Graduate School ETD Form 9
(Revised 12/07)

PURDUE UNIVERSITY
GRADUATE SCHOOL
Thesis/Dissertation Acceptance

This is to certify that the thesis/dissertation prepared

By Ukwatte Lokuliyanage Indika Upendra Perera

Entitled
Experimental Investigation into Combustion Torch Jet Ignition of Methane-air, Ethylene-air, and Propane-air Mixtures

For the degree of Master of Science in Mechanical Engineering

Is approved by the final examining committee:

M. Razi Nalim
Chair

Jian Xie

Likun Zhu

To the best of my knowledge and as understood by the student in the *Research Integrity and Copyright Disclaimer (Graduate School Form 20)*, this thesis/dissertation adheres to the provisions of Purdue University's "Policy on Integrity in Research" and the use of copyrighted material.

Approved by Major Professor(s): M. Razi Nalim

Approved by: Sohel Anwar 12/07/2010
Head of the Graduate Program Date

Graduate School Form 20
(Revised 9/10)

PURDUE UNIVERSITY
GRADUATE SCHOOL

Research Integrity and Copyright Disclaimer

Title of Thesis/Dissertation:

Experimental Investigation into Combustion Torch Jet Ignition of Methane-air, Ethylene-air, and Propane-air Mixtures

For the degree of Master of Science in Mechanical Engineering

I certify that in the preparation of this thesis, I have observed the provisions of *Purdue University Executive Memorandum No. C-22,* September 6, 1991, *Policy on Integrity in Research.**

Further, I certify that this work is free of plagiarism and all materials appearing in this thesis/dissertation have been properly quoted and attributed.

I certify that all copyrighted material incorporated into this thesis/dissertation is in compliance with the United States' copyright law and that I have received written permission from the copyright owners for my use of their work, which is beyond the scope of the law. I agree to indemnify and save harmless Purdue University from any and all claims that may be asserted or that may arise from any copyright violation.

Ukwatte Lokuliyanage Indika Upendra Perera

Printed Name and Signature of Candidate

11/23/2010

Date (month/day/year)

*Located at http://www.purdue.edu/policies/pages/teach_res_outreach/c_22.html

EXPERIMENTAL INVESTIGATION INTO COMBUSTION TORCH JET IGNITION OF METHANE-AIR, ETHYLENE-AIR, AND PROPANE-AIR MIXTURES

A Thesis
Submitted to the Faculty
of
Purdue University
by
Ukwatte Lokuliyanage Indika Upendra Perera

In Partial Fulfillment of the
Requirements for the Degree
of
Master of Science in Mechanical Engineering

December 2010
Purdue University
Indianapolis, Indiana

ACKNOWLEDGMENTS

I would like to acknowledge the guidance and support of my major professor and academic advisor Dr. M. Razi Nalim in research related activities as well as my academic studies. Furthermore I would like to thank Dr. Nalim for the opportunity he offered me to work as a research assistant with him while reading for my master's degree in mechanical engineering.

My gratitude goes out to my committee members Dr. Jian Xie and Dr. Likun Zhu, for the help and support they gave me in completing my studies. I would like to thank Dr. Sivakumar Santhanakirhnan who was one of my course instructors as well as a former committee member for the valuable advice and support I received from him.

I would like to acknowledge the support and assistance of Dr. Jie Chen and the Dept. of Mechanical Engineering for providing the required facilities for my study. I appreciate the help of Rudolph Earlson, Joseph Huerkamp, and Daniel Aw in machining necessary components, purchasing materials, and designing of components that were required for the experimental rig. I appreciate the effort of Sudha Takur, who volunteered to work with me in creating the model components and the drawings necessary for the redesigned main chamber.

I would like to thank my colleagues at the Combustion and Propulsion Research Laboratory, Sameera Wijeyakulasuriya, Tarek Elharis, Ruturaj Kulkarni, Kevin Murphy, and Abdullah Karimi, for their valuable input and help they have given me. I would like to thank Brian Froelich the research assistant who worked on the single-channel wave-rotor combustion rig before me, for helping me in the initial stages of the study. I would

further like to thank the assistance of Dr. Viktor Kilchyk, Dr. Hongwei Li, and Zachary Lightner who worked at the CPRL during my study at IUPUI.

I acknowledge the effort of the Summer 2010 MURI project team comprising of Matthew Bixler, Ahamed Farook, and Arash Pourtaherian, who helped in conducting experiments from July to August 2010.

I am grateful for the help of Valerie Lim Diemer, Ginger Lauderback, and Amanda Herrera, related to the administrative issues as well as in preparation and formatting of this thesis.

I appreciate the support of the Computer Networking Center at IUPUI with special thanks to Donald Krajewski and Robert Meagher.

Finally, I would like to thank my wife, my daughter, and our families back in Sri Lanka, who have sacrificed a lot in the attempt to grant me the peace of mind and support in completing my graduate studies.

TABLE OF CONTENTS

Page

Page

LIST OF TABLES

LIST OF FIGURES

Figure Page

Figure Page

Figure Page

Appendix Figures

Appendix Figure Page

ABSTRACT

Perera, Ukwatte Lokuliyanage Indika Upendra. M.S.M.E., Purdue University, December 2010. Experimental Investigation into Combustion Torch Jet Ignition of Methane-Air, Ethylene-Air, and Propane-Air Mixtures. Major Professor: M. Razi Nalim.

Ignitability and the ignition delay time of a combustible mixture in a long combustion chamber, ignited by a hot combustion torch jet generated in a pre-chamber was investigated experimentally in relation to application as a viable igniter method for wave rotor combustors. Methane-air, ethylene-air, and propane-air in varying equivalence ratios were investigated as the combustible mixture in the combustion chamber. The effects of variation in the torch jet fuel, initial equivalence ratio in the pre-chamber, and nozzle geometry on the ignitability and the ignition delay time of combustible mixtures were observed and analyzed.

The single-channel wave-rotor combustion rig at Combustion and Propulsion Research Laboratory at the Purdue School of Engineering and Technology at Indiana University-Purdue University, Indianapolis was used for this study. High-speed video imaging techniques to observe the ignition and flame propagation in the combustion chamber and fast-response pressure transducers to measure the dynamic pressure fluctuations in the combustion chambers were used in the current study.

The present work explains how the experimental procedure and preliminary testing was carried out in order to conduct the necessary testing to find the ignitability and ignition delay time of a combustible mixture.

Ignitability of methane, ethylene, and propane were much broader in range compared to conventional spark ignitable lean and rich limit equivalence ratios. The methane and propane ignition lean limits were similar to radical activated ignition lean limits found in previous studies of the same fuels. Ethylene exhibited the widest range in equivalence ratios from 0.4 to 2.4, while methane had the narrowest ranging from equivalence ratio 0.4 to 1.4.

The ignition delay studies indicated both chemical kinetics and mixing between the combustion torch jet and the combustible mixture were critical. The mixing phenomena dominated chemical kinetics; unlike in ignition delay studies conducted using shock heated ignition techniques. Ethylene-air mixtures had the shortest ignition delay times ~1 ms for lean but near-stoichiometric mixtures. Methane and propane indicated similar ignition delay time characteristics with lean near-stoichiometric mixtures.

The fuel-air equivalence ratio which was used to generate the combustion torch jet and the torch jet nozzle geometry had a direct influence over the ignition delay time in the main chamber combustible mixture. The slightly rich fuel-air ratios used to generate the combustion torch jet had the lowest delay times in igniting the main chamber fuel-air mixtures.

CHAPTER 1. INTRODUCTION

1.1. Background

Internal combustion engines, both positive-displacement piston engines and steady-combustion gas turbine engines, have been the cornerstone of power generation and propulsion for the last century. While the positive-displacement piston engines are preferred for automobile applications, the steady-combustion gas turbine engines are predominantly used in the aviation and power generation applications. Alternative intermittent or pulsed-combustion (unsteady) systems have received renewed interest with the highly publicized pulsed detonation engines (PDEs). These intermittent combustion devices provide a pressure rise compared to its steady combustion counterpart where there is a reduction in the stagnation pressure in the steady combustion devices. These pressure-gain unsteady combustion devices could be used to replace the steady-combustion devices such as the gas turbines.

Numerous conceptual devices have been used to achieve this pressure-gain combustion, which would lead to increased power, or thrust, improved fuel efficiency, reduced nitrogen oxides (NOx) formation, and other benefits expected from any conventional internal combustion engines. The Humphrey thermodynamic cycle is the theoretical operating cycle for a device that uses the upstream compressed gas which is combusted in a constant-volume combustor, and in turn expanded in another device or flow downstream of the combustor. Figure 1.1 illustrates the concept of the pressure-gain combustor engine. Figure 1.2 illustrates the significant difference in the thermodynamic operating cycles between the Humphrey cycle and the Brayton cycle (the gas turbine operating cycle) using a temperature-entropy (T-s) diagram. The turbine inlet temperature and the compressor discharge pressure are fixed in the T-s diagram for the two cycles for

comparison purposes. The pressure rise in the constant-volume combustion from state 2-3 instead of the constant-pressure combustion from state 2-3_b brings about the higher power output and higher efficiency for a fixed energy input. This increase in efficiency is evident by the reduction in the entropy from state 2-3 in the Humphrey cycle compared with the process from state 2-3_b in the Brayton cycle. Akbari and Nalim [1] compare the entropy generation of these two cycles using an air-standard cycle and specific heat ratio of $\gamma = 1.33$ show that there is a reduction of about 25% of the entropy production. This reduction in entropy production is an advantage of the constant-volume combustion over the constant-pressure combustion.

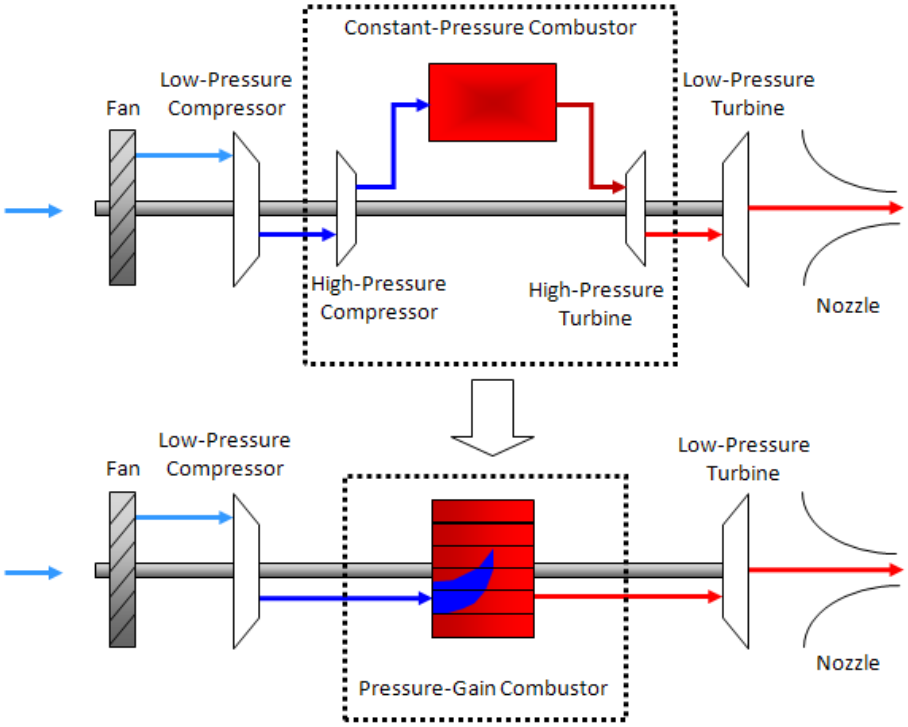

Figure 1.1 Schematic representation of the pressure-gain combustor (recreated by thesis author from reference [1])

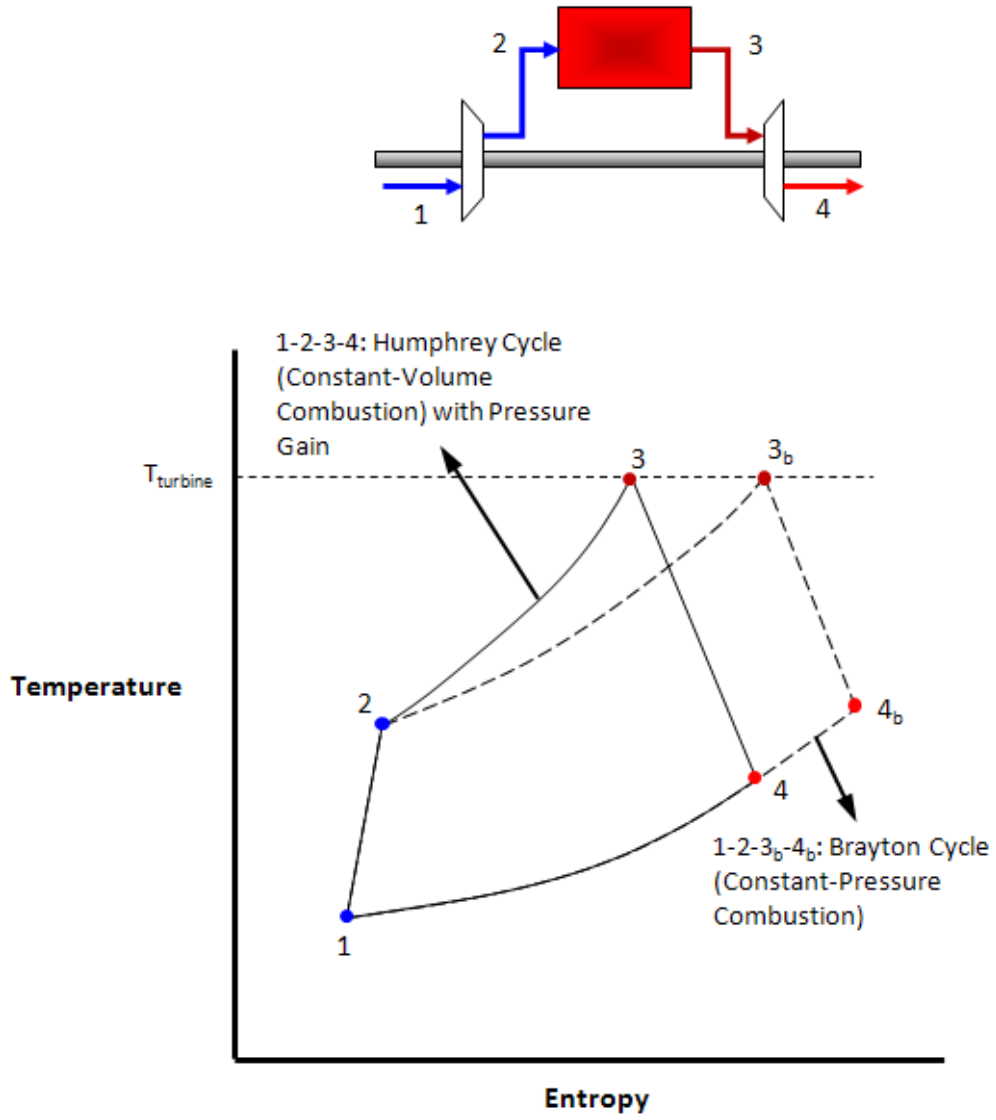

Figure 1.2 Comparison of Humphrey cycle (1-2-3-4) with Brayton cycle (1-2-3_b-4_b) (recreated by thesis author from reference [1])

The constant-volume wave-rotor combustor is a device that utilizes this advantage presented by the Humphrey cycle. A schematic configuration of a wave-rotor combustor is illustrated in Figure 1.3. The rotor consists of a number of sequentially arranged channels around the periphery of a drum. These channels are usually, but not necessarily, arranged in the axial direction of the drum. The drum rotates between two endplates

which are stationary. Each endplate has a number of ports or manifolds at different pressures and contain different fluids connected to them. The schematic only illustrates the inlet and outlet ducting on the endplate. These ports or manifolds in the endplates control the flow of fluids through the channels in the rotor. The endplates isolate the channels in the rotor from the environment creating the constant-volume combustion chambers. The channel openings are periodically exposed to and isolated from the ports or manifolds in the endplates when the channels rotate past the openings in the endplate.

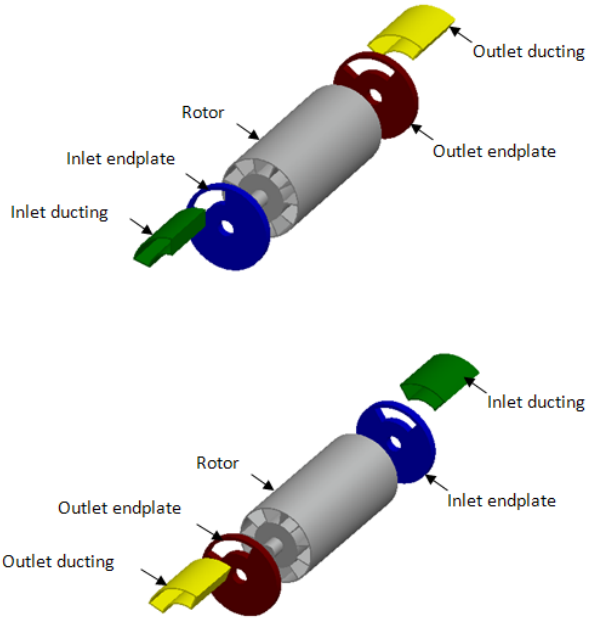

Figure 1.3 Schematic configuration of a wave-rotor combustor from the inlet (top) and outlet (bottom) orientations

The sudden opening and closing of the channels to the stationary ports when the rotor rotates, initiates gas dynamic compression and expansion waves with in the channel which propagate the length of the channel interacting with the fluid flow. These waves affect dynamic pressure and energy exchange within the fluid in the channels without pressure equilibration. The orientations of the inlet and exit port locations are critical to this effect.

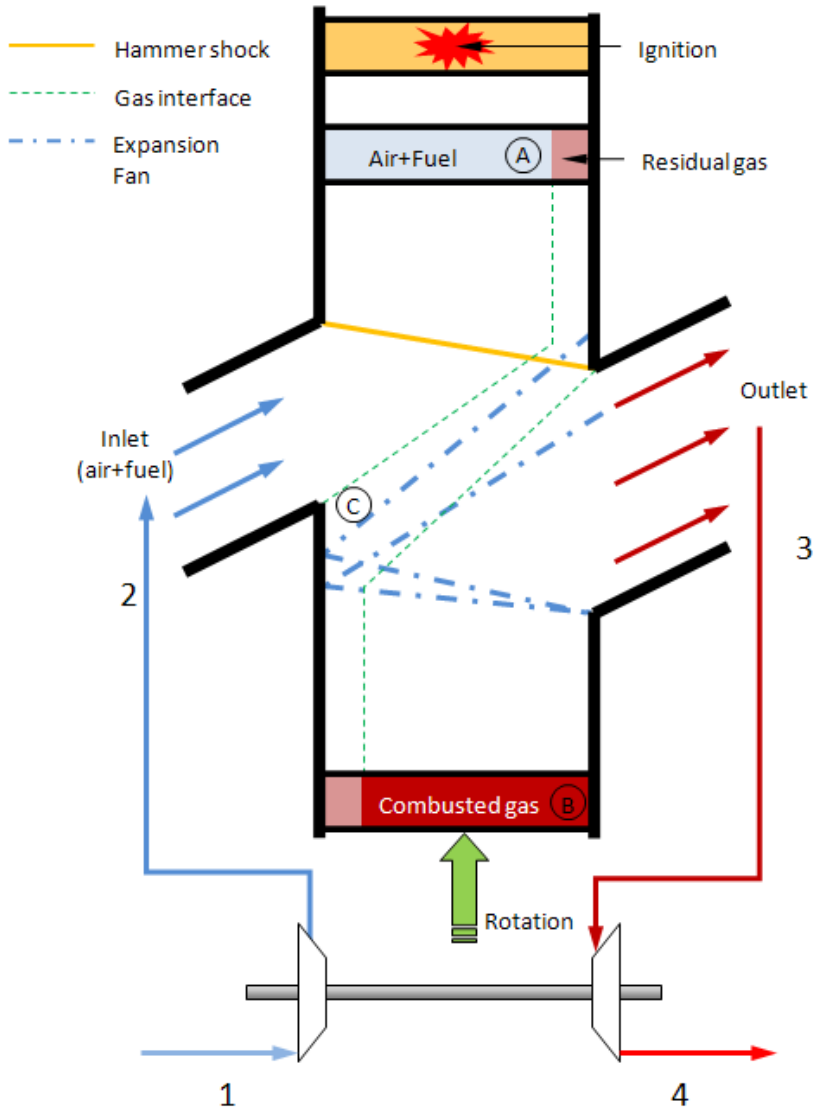

Figure 1.4 Schematic developed view of a wave-rotor combustor (recreated by thesis author from reference [1])

These gas-dynamic processes that take place inside the channels of a wave-rotor combustor are illustrated in Figure 1.4. The diagram is an unwrapped (developed) view of the wave rotor combustor, which demonstrates the sequential purging, filling, and igniting phases that take place inside a single channel as it rotates around the rotor axis. The rotary motion of the channels is represented by the vertical motion in the upward direction. This can be interpreted as the representation of changes that occur inside a

single channel of the rotor as time varies along the vertical time axis, but the former interpretation is going to be utilized to explain the gas-dynamic processes. At any given time during the rotation of the wave rotor, a number of channels are open at the same time to the inlet port and to outlet port. The other channels are closed at both ends by the endplates and therefore are under constant-volume conditions. The gas composition inside a few channels and the gas-dynamics inside other channels are illustrated by simple wave trajectories in Figure 1.4. The complex flow patterns, mixing phenomena, combustion, and trifling reflected waves are not illustrated in order to maintain the simplicity of the figure.

The operating cycle of a simple wave-rotor combustor includes the intake process of fresh air and fuel mixture into the channel, igniting this combustible mixture admitted in the intake process and completing the combustion under constant-volume conditions, and exhaust process out through the outlet port. At state B the channel is closed at both ends and the combustible mixture is completely combusted, achieving higher temperature and pressure compared to temperature and pressure attained inside a constant-pressure combustor. The opening of the outlet port exhausts the high pressure and high temperature combustion products to a lower pressure exhaust manifold creating an expansion wave that propagates into the channel towards the inlet port. This expansion wave accelerates the combustion products out through the outlet port. The channel opens up to the inlet port as the expansion wave arrives at the inlet port end which draws the fresh air-fuel mixture into the channel. This helps in purging the channel of the exhaust gases. As the filling process continues on the inlet side of the channel the outlet port closes, disabling the fresh air-fuel mixture and remaining fraction of the exhaust gas from going through to the outlet manifold. This sudden closure of the exit port generates a compressive wave termed “hammer shock” which propagates towards the inlet side. The inlet port is designed in such a way that this hammer shock does not propagate through the open inlet port. The combustible gas mixture at state A, which is made up of fresh air-fuel and the residual gas from combustion in the earlier cycle, is ignited using an igniter

(not indicated in the figure). The combustion returns the contents inside the channel to state B completing the cycle.

The wave rotor combustor has to ensure that it is able to ignite the combustible mixture as well as completely combust the channel contents to ensure the combustion process is completed while the channels are closed at both ends. This only leaves the combustor a fraction of the total cycle time to complete the combustion process. In addition, rapid combustion also minimizes losses due to heat transfer and channel leakage. The leakage is the outflow of gas through the gap created in between channel ends and the endplates due to the high-pressure created inside the channels compared to the ambient pressure around the wave-rotor. The minimization of NOx and other harmful emissions and minimized weight and volume to the power developed are other important features required from a wave rotor combustor engine.

All these requirements and/or features stipulate a dependable ignition source and fast combustion. Both deflagration and detonation combustion methods are plausible for application in wave rotor combustor engines [2-7]. The ignition of the combustible mixture can be initiated with igniters on either endplate or even in both endplates depending on the desired combustion propagation direction of the wave rotor combustor. The ignition sources or methods of ignition in a wave rotor combustor may vary from conventional ignition devices used in internal combustion engines, such as spark plug devices and glow plugs, to unconventional methods such as laser ignition devices, a separate pre-combustion chamber, combustion products routed from a previously burned channel in the same wave rotor, and any combination of these methods [6]. The use of a sparkplug for start up operations and then, using combustion products from a previously combusted channel to ignite the combustible mixture inside a succeeding channel of the wave rotor for self-sustained operation is an example of a combined ignition method [3]. This thesis is focused on ignition of pre-mixed combustible mixtures with combustion product jets or torch-jet which can give an insight into either of the methods that use hot combustion products to ignite the combustible mixture in a wave rotor combustor channel as explained earlier.

1.2. Literature Research

Ignition of a combustible mixture by hot combustion-product jets is one of the ignition methods proposed to be used in wave rotor combustors. The literature in this regard and other ignition methods proposed for wave rotor combustor applications is limited at best. The ignition of combustible mixtures using combustion products is plagued with complex flow phenomena and fluid mixing in addition to the chemical kinetics associated with combustion of fuels. The chemical kinetics of different fuels involved with ignition delay studies are commonly conducted using shock tube facilities where the combustible fuel-air mixtures are ignited behind the reflected-shock wave. The preference of shock tube facilities for these ignition delay experiments is the uniform instantaneous heating of the combustible mixture and the ability to vary the ignition temperature by changing the pressure ratio between the driver and the driven sections. These reflected-shock waves are generated using a sealed pipe (generally of constant cross-sectional area) divided into a high-pressure driver side and a low-pressure driven side filled with a combustible mixture by a physical diaphragm. The diaphragm is ruptured or removed allowing the high-pressure driver gas to compress the driven gas. Due to the sudden removal of the diaphragm, pressure waves start propagating into the low driven gas side with each passing pressure wave increasing the temperature and velocity of the of the wave above the one that propagates in-front of it. These pressure waves culminate into a shock wave which raises the temperature and pressure of the driven gas. An expansion fan (Prandtl-Meyer) propagates into the driver gas at the same time. The propagating shock wave, once arriving at the closed end on the driven side, reflects as a shock wave propagating in the opposite direction from which it came further increasing the temperature of the once compressed combustible mixture, igniting the combustible mixture. The initial driver and the driven gas pressures are predetermined to ignite the mixture for conditions behind the reflected shock wave.

Ignition delay time for shock tube experiments varies from torch jet ignition experiments due to the physical difference of the experiment. This changes both the physics that govern the experiment and ultimately the ignition chemistry in determining

the chemical kinetics [8]. Although the torch jet ignition experiment physics and chemistry are different from the shock ignition experiment, the chemical kinetics are the same for both as long as the temperatures and pressure conditions governing these chemical kinetics are similar. The reasons for using shock heated ignition in chemical kinetic studies are the ability to instantaneously (approximately in nanoseconds) and uniformly heat the combustible mixture. In addition to this, the experimental observation timescales to determine chemical kinetics is short compared to diffusion timescales when compared to other methods of ignition [8].

Experiments and study of ignition of combustible mixtures by hot gases were studied in relation to safety in mines, where the majority of the research publications were from the Bureau of Mines, U. S. Department of Interior [9-14]. These experiments were all conducted with a steady non-reactive hot gas jet injecting into a well-mixed stationary or quiescent combustible mixture. Wolfhard's [9] work indicated that there is a slight increase in "ignition temperature" when the gas of the heated jet was changed from atmospheric air to nitrogen for all test fuels. The "ignition temperature" is defined as the steady jet-base temperature at which the luminous region in the combustible mixture transforms into ignition. Wolfhard [9] also states for ethane, ethylene, and carbon monoxide the ignition temperature changes depending upon the type of hot gas used. Nitrogen and carbon dioxide having similar ignition temperatures, while argon and helium have higher ignition temperatures respectively. Vanpée and Wolfhard [11] conclude that except for some fuels or combustible mixtures a correlation can be found between the "ignition temperature" and the "limit flame temperature" for a particular fuel. This "limit flame temperature" was measured using a diffusion flame around a stainless steel hemisphere [15]. Fink and Vanpée [13] developed an overall rate expression for describing the ignition of fuel-air mixtures at relatively low-velocities by a hot inert gas jet for methane, ethane, and ethylene similar to laminar flame simplified reaction rate expressions [16]. Cato and Kuchta [14] state the "ignition temperature" depend on the jet dimensions, composition of the combustible mixture, and jet velocity.

They also claim that the ignition depends on jet base temperature rather than on rate of heat injected from the jet to the combustible mixture.

Ignition of a combustible mixture by a turbulent jet of radicals generated in a pre-chamber was studied by Gussak [17], Oppenheim [18], Murase [19-20], Wallesten [21], Valle [22], Toulson [23, 24], Attard [25], and Yamaguchi [26]. This method of ignition generally termed as Avalanche Activated Combustion or LAG (Lavinnaia Aktyvatsia Gorenia-acronym in Russian) in which the basic concept is to initiate combustion in the main chamber using highly active radicals generated in a fuel-rich pre-chamber was extensively studied by Gussak [17]. The 5-7 fold reduction in ignition delay and 3-4 fold reduction in combustion duration were important findings related to this LAG method compared with conventional sparkplug ignition systems. The pulsed combustion jet (PCJ) or pulsed flame combustion (PFJ) as it was later named is an evolution of the LAG concept [18] where the flame is quenched by letting the jet expand into the main chamber via an orifice or a nozzle of appropriate sizing. Another off-shoot of this same concept was to use electrical discharge to produce a plasma jet to ignite the main chamber fuel-air mixture and was called pulsed plasma jet (PPJ) [21]. The distinction of these studies is that the pre-chamber volume is much smaller than the main-chamber volume where the combustible mixture resides. These radical jets being generated either with combustion or by electrical discharge, have the ability to ignite fuel-lean mixtures unable to be ignited by conventional spark ignition methods. In addition to this, high fuel economy and low nitrogen oxides and carbon monoxide emission are also achieved in these radical jet ignition systems [22-26].

Tarzhanov et al. [27], using hot detonation products to detonate stagnant propane-air mixtures, have found that detonation of the propane mixture is dependent on the initial volume concentrations, mass fraction of hot detonation products to propane-air mixture, and energy deposited from the detonation products. Using experimental observations and numerical modeling of the complex phenomena that are interrelated in the torch jet ignition processes Mayinger et al. [28] found a correlation between the induction time

(ignition delay time) and mixing time of the jet and adiabatic ignition delay for the fuel-air mixtures that were investigated.

Bilgin et al. [29, 30], using the same single channel wave-rotor constant volume combustor rig used in this current study, conducted a series of experiments to find a correlation between Damköhler number and ignition of a fuel-air mixture in the main chamber by a torch jet generated in a pre-chamber. An important feature of this experimental rig is that it has the ability to simulate the effects of the stationary igniter port interaction with the rotating channels of the wave-rotor combustor, in an inverse design, where the igniter port represented by the pre-chamber is traversing the opening of the stationary channel. The effects of initial pressure, equivalence ratio, pre-chamber geometry, nozzle geometry, and the traversing speed of the pre-chamber were studied using high-speed video imaging and pressure history data captured using pressure transducers placed in locations along the length of the channel. Using the experimental data from this single channel wave-rotor constant volume combustor rig and Star-CD computational fluid dynamics (CFD) code, Baronia et al. [31, 32] numerically simulated the stationary (the pre-chamber torch jet axially aligned with the channel axis) experiments conducted by Bilgin et al. A four-step kinetic reaction model was used to simulate combustion in the numerical study where the ignition in the main chamber appeared to be more sensitive towards a threshold temperature (not the ignition temperature) compared to local equivalence ratio and turbulence kinetic energy. This temperature was the critical temperature limit used in the kinetic modeling of combustion used in the numerical simulation.

1.3. Objectives of Current Research

The main objective of this study was to gain an insight into the types of fuels suitable for wave-rotor combustor applications. Three fuels, namely methane, ethylene, and propane were tested under varying equivalence ratios in both the pre-chamber and the main chamber. These chambers were initially maintained at atmospheric pressure and room temperature respectively.

The ignition delay time variation for each fuel under constant experimental conditions and the ignitable limits, both lean and rich, for all three fuels in the main chamber were investigated. The variation of ignition delay time for fuels with different pre-chamber equivalence ratios and nozzle geometry were also observed.

CHAPTER 2. EXPERIMENTAL FACILITY AND METHODOLOGY

The single-channel wave-rotor combustion rig was originally built by Bilgin et al. [29, 30] at the University of Washington in the late 1990s with the financial support of National Aeronautics and Space Administration (NASA) Lewis Research Center. All experiments pertaining to this study were carried out at the Combustion and Propulsion Research Laboratory (CPRL) at the Purdue School of Engineering and Technology at Indiana University-Purdue University, Indianapolis (IUPUI). This chapter gives a description on the individual components comprising the experimental facility, the equipment used in measuring the experimental variables, equipment and tools used for data acquisition and high-speed video imaging.

2.1. Experimental Setup

The single channel wave-rotor combustion rig consists of two sub-assemblies, the pre-chamber and the main chamber. The pre-chamber is mounted on a shaft that can be rotated with the use of an electric-motor via a belt-drive. Bilgin [29, 30] used a similar mechanism for the rotary experiments. However, the experiments for the current study were all conducted with a stationary pre-chamber. Figure 2.1 shows the experimental facility at CPRL and the main equipment and systems used in the experiment including the single channel wave rotor rig, the Vision Research Phantom v9.0 high-speed video camera, and the fueling system. For ease of moving the fueling system, the entire fueling system including the vacuum pump, flow control valves, and flow regulators were mounted on a steel cart.

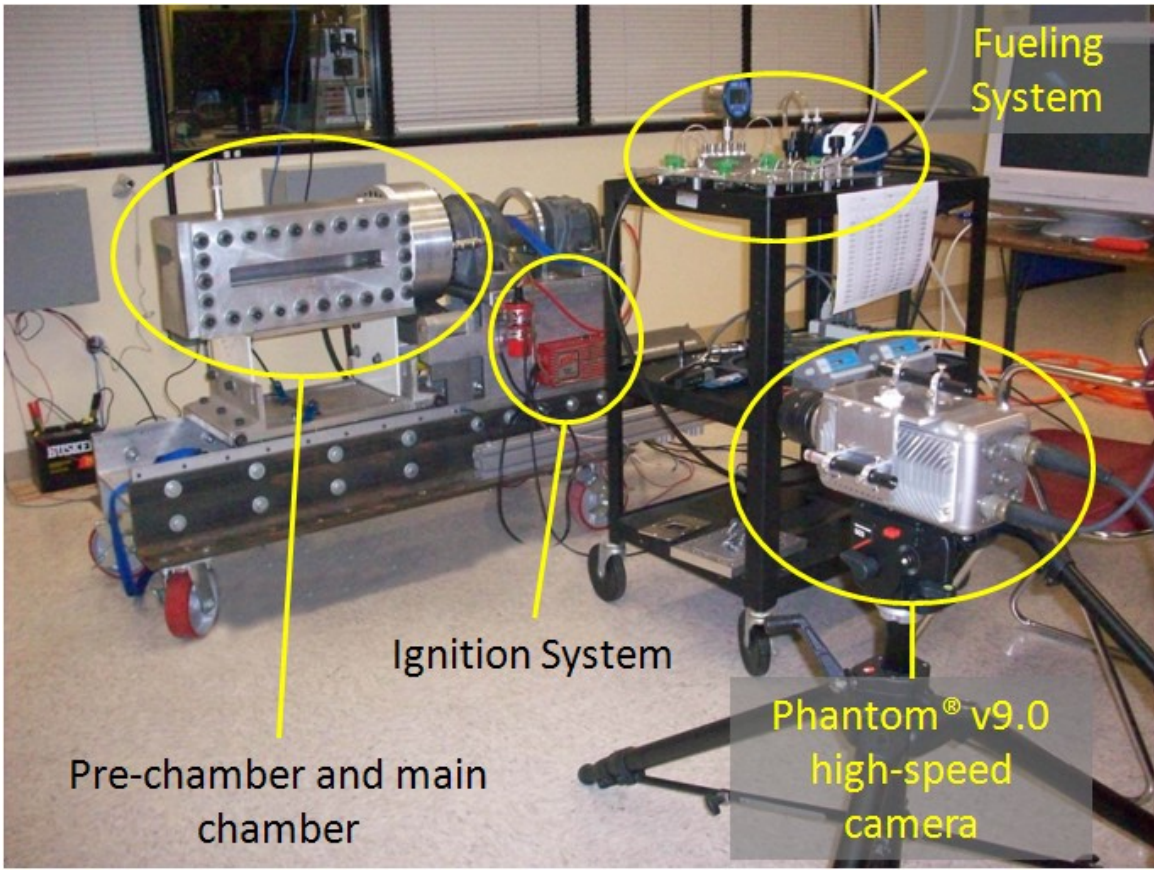

Figure 2.1 Experimental facility in CPRL

Figure 2.2 is the computer aided design (CAD) model of the single channel wave rotor combustor rig modeled using Pro/ENGINEER® education edition by Parametric Technology Company (PTC®). The main chamber is placed flush against the pre-chamber before the start of each experiment by moving the main chamber towards the pre-chamber along the H-beam and clamping the main chamber. The pre-chamber and main chamber design drawings are provided in Appendix A.

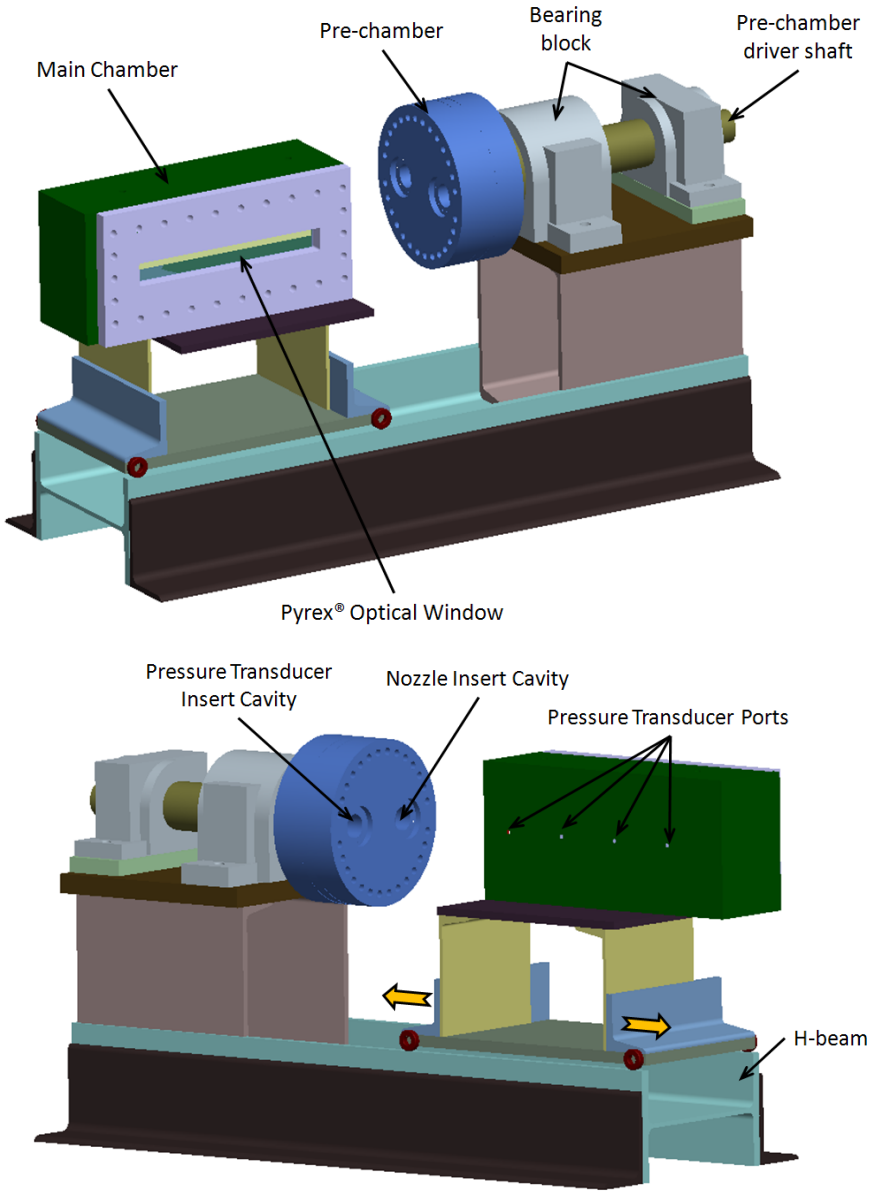

Figure 2.2 CAD model of the single channel wave-rotor combustor rig: (top) 3d view from the front side, (bottom) 3d view from the rear side

2.1.1. Pre-Chamber

The pre-chamber uses a spark plug to generate hot combustion products in a combustion torch-jet similar to the torch-jet igniters described in other research conducted [3, 17, 18] which ensure a stable and reliable combustion source. The pre-

chamber consisted of three main components representing a front plate, rear plate, and a middle ring (Appendix A). The pre-chamber internal cavity is of cylindrical design of diameter 6.519 in and a length of 1.536 in encompassing an internal volume of 51.268 cubic in.

The front plate has two identical cylindrical cavities placed symmetrically, to ensure static and dynamic balance of the pre-chamber under rotary test conditions (Figure 2.3 (e)). The importance of this symmetry of the cylindrical cavities to the stationary experiments was in determining the pressure inside the pre-chamber at the nozzle inlet. This pressure history data was used for evaluation of the diaphragm rupture time explained in detail in the next chapter. One of the pre-chamber front plate cavities was used to insert a pressure transducer to measure the pressure history inside the pre-chamber, while the other cavity was used for one of several nozzles. The symmetry of the pre-chamber internal volume and the location of the nozzle and pressure transducer insert were used to assume the pressure measured at the pressure transducer location was the same as the pressure at the inlet of the nozzle. This assumption can only be justified for symmetric flame propagation leading to predictable rate of fuel consumption and pressure rise inside the pre-chamber. This is a justifiable in relation to the experimental conditions and the geometry inside the pre-chamber.

The rear plate was used to mount the pre-chamber sub-assembly onto the pre-chamber driver shaft. In addition to this, the rear-plate also had the fueling ports for the pre-chamber and the sparkplug attached at the center of the plate. The middle ring is a simple annular ring to provide the required volume between the front plate and the rear plate.

In order to fuel the pre-chamber the nozzle was separated from the pre-chamber by an aluminum diaphragm of thickness 0.003 in. The aluminum diaphragm was scored using a scoring mechanism for controlled tearing of the aluminum diaphragm into four petals along two perpendicular lines of symmetry on the diaphragm as illustrated in Figure 2.3 (a) and (b).

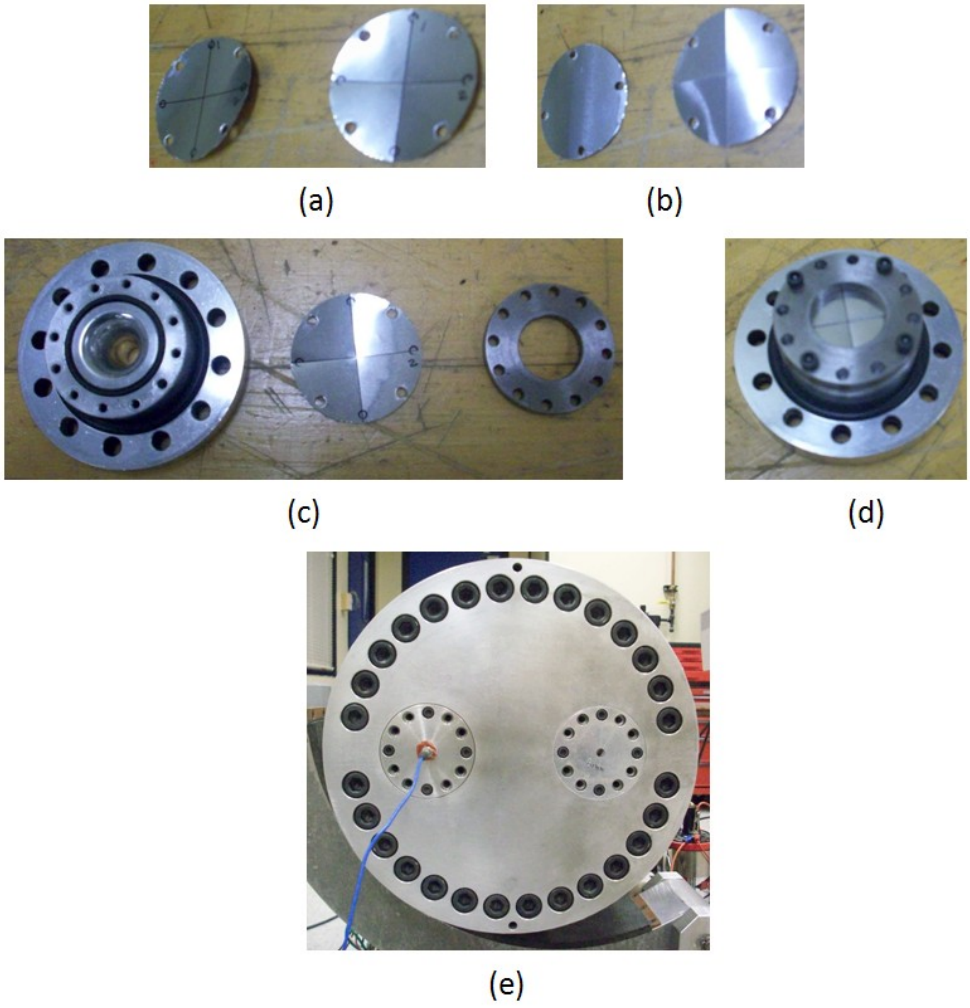

Figure 2.3 Aluminum diaphragm integrated into the nozzle insert: (a) aluminum diaphragm on the left and scored diaphragm on the right from the front, (b) aluminum diaphragm on the left and scored diaphragm on the right from the back, (c) nozzle insert, scored diaphragm, and nozzle plate, (d) nozzle assembly, and (e) pre-chamber with nozzle insert on the right and pressure transducer insert on the left

2.1.2. Main Chamber

The main chamber was machined of a single solid aluminum block of 9.0 in × 6.0 in × 19.5 in external dimensions. The combustion chamber has a square cross-section of 1.57 in × 1.57 in and is 16.0 in long. One wall of the combustion chamber consists almost entirely of an optical window allowing visual access into the main chamber (Figure 2.2

(top) and Figure 2.4 (a)). Ignition occurs from the right end of the main chamber, when viewed from the optical window side.

The main chamber has four pressure transducers mounted flush on the wall opposite to the optical window at four locations down the length of the combustion chamber (Figure 2.4 (b)). The dimensions of the main chamber and locations of the pressure transducers are shown in Appendix A. The distance from the channel entrance to each pressure transducer location is listed in Table 2.1.

Table 2.1 Pressure transducer locations

Pressure Transducer	Distance from the entrance (in)
PT-1	2.00
PT-X	6.34
PT-2	10.67
PT-3	15.00

The main chamber optical window was a 2.0 in thick Pyrex® rectangular cube of cross-section 16.0 in × 5.0 in. The Pyrex® optical window was clamped down by the window plate with a rectangular cut of dimensions 13.638 in × 1.570 in. The rectangular cut started from 2.362 in from the entrance of the channel due to structural constraints [30]. The main chamber also housed two fueling port locations on the top surface of the chamber. For the current study, the port farthest away from the entrance was used for fueling.

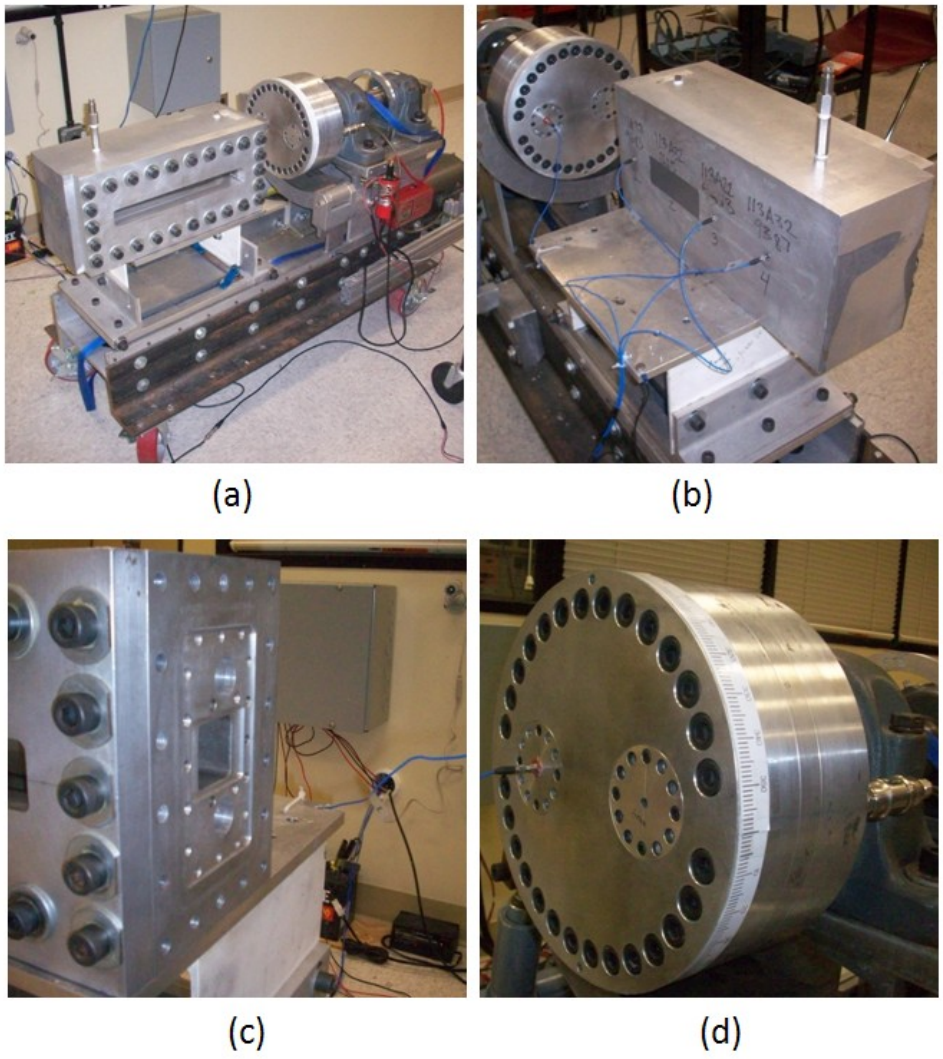

Figure 2.4 Single channel wave rotor combustor rig: (a) from the optical window side, (b) from the pressure transducer side, (c) main chamber channel entrance, and (d) pre-chamber nozzle exit face

For fueling the main chamber, a latex diaphragm of 0.006 in. initial thickness was stretched over the diaphragm plate as indicated in Figure 2.5. The amount of stretch the latex diaphragm was subjected to was determined by the procedure explained below. The latex diaphragm with no stretch was opaque and therefore the text behind the latex diaphragm is illegible (Compare Figure 2.5 (b) and (c)). The diaphragm was stretched until the text behind the latex diaphragm was legible as observed in Figure 2.5 (d). The text was approximately 2 in below the latex diaphragm and a simple test bench was used

as a testing bed with a step to house the diaphragm plate and a square hole in the middle similar to the diaphragm plate. Then this diaphragm plate covered on one side by the latex diaphragm was placed in the step machined in the entrance face of the main chamber as can be observed in Figure 2.6. The diaphragm backing plate was placed on top of the diaphragm plate and fixed to the main chamber using screws. Before the fueling commenced a solid aluminum plate (fueling plate) was bolted on to the main chamber entrance face over the diaphragm backing plate to ensure the latex diaphragm did not rupture due to the vacuuming of the main chamber prior to the fueling. The vacuuming and fueling processes are explained later in the chapter. This fueling plate was removed after the fueling was completed before the main chamber was moved flush against the pre-chamber for the commencement of the experiment.

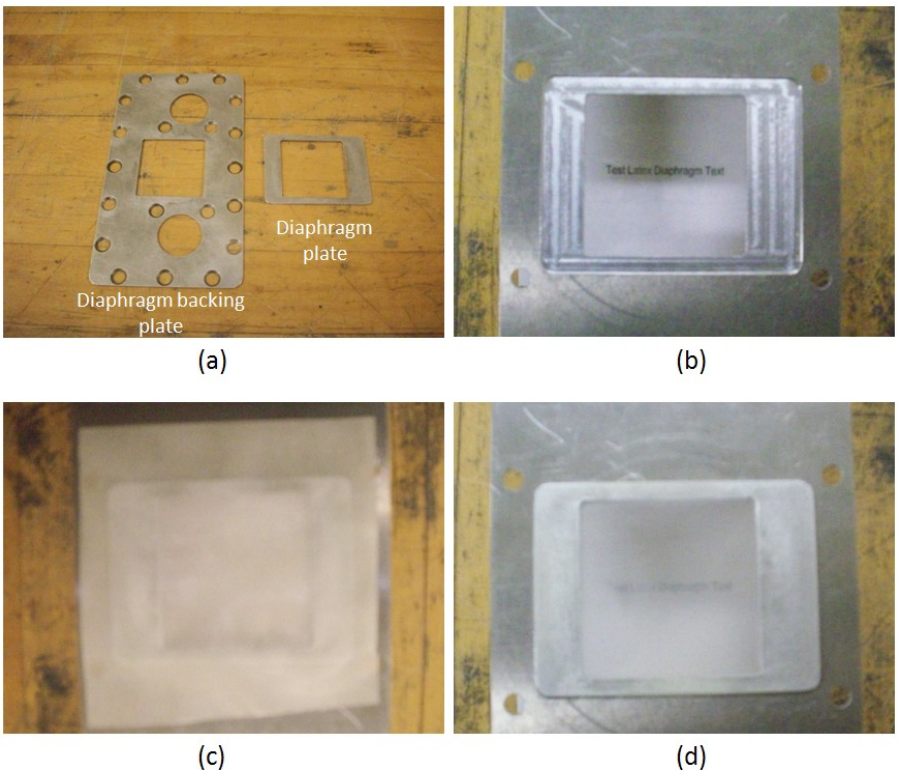

Figure 2.5 Preparation of the latex diaphragm: (a) diaphragm plate and diaphragm backing plate, (b) the setup used to assess the strech of the latex, (c) with un-streched latex diaphragm, and (d) with streched latex diaphragm

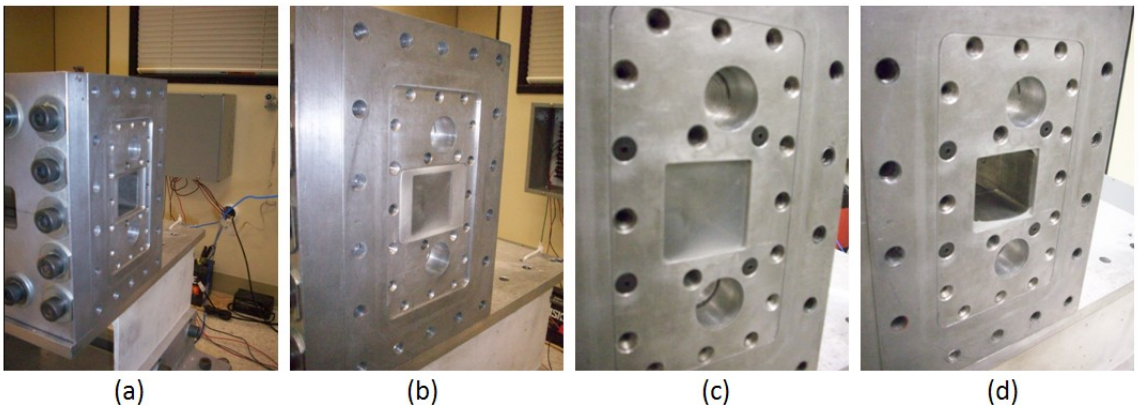

Figure 2.6 Main chamber latex diaphragm and plate assembly: (a) main chamber channel entrance face, (b) diaphragm plate inserted in the main chamber with latex diaphragm stretched over it, (c) after clamping the diaphragm backing plate over the diaphragm plate, and (d) diaphragm assembly after an experiment

Figure 2.7, shows the pre-chamber and main chamber diaphragm locations in the single channel wave rotor combustion rig. The Figure 2.7 (a) indicate the orientation and location from where the cross-sectional view is obtained. The Figure 2.7 (b) illustrate the pre-chamber cavities the nozzle insert assembly (shown in red) and the pressure transducer insert (shown in orange) are mounted. The latex diaphragm assembly is shown in green. The lower half of Figure 2.7, indicate a detailed view (Figure 2.7 (d)) of the aluminum diaphragm assembly and the latex diaphragm assembly. Figure 2.7 (c) show the diaphragm plate and the diaphragm backing plate which make up the diaphragm assembly with the latex diaphragm wrapped over the diaphragm plate as indicated in Figure 2.5 (d). Figure 2.7 (e) shows the breakdown of the nozzle assembly to the nozzle insert, scored aluminum diaphragm, and the nozzle plate.

The combustion in the pre-chamber increases the pressure in the chamber until the aluminum diaphragm rupture and allow the hot combustion torch jet to flow through the nozzle. The torch jet impinges on the stretched latex diaphragm rupturing it and entering into the main chamber.

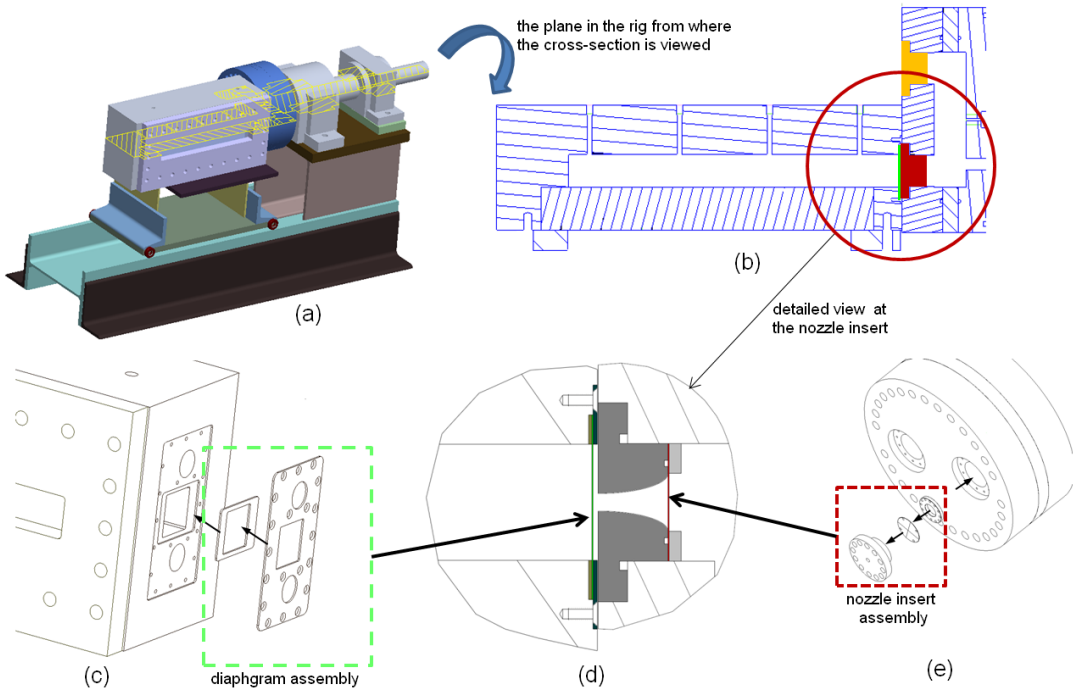

Figure 2.7 Single channel wave rotor combustion rig cross-section with pre-chamber and main chamber diaphragms

2.1.3. Nozzle Inserts

All nozzles used for the current study are categorized in Table 2.2 below with the major dimensions of each nozzle provided in Appendix B. Nozzles A-E were for the current study and flame propagation studies conducted at IUPUI while nozzles F and G were two of the nozzles used by Bilgin [30] in his study, classified as nozzle 2 and nozzle 3, respectively. Each of these nozzles have the same inlet diameter of 0.787 in. but the exit and throat diameter varied along with the internal geometry of the nozzle. Nozzles A-D were convergent nozzles, while the others were convergent-divergent nozzles with E and G having straight cone geometry and nozzle F having a hemispherical convergent section and a straight-cone divergent section.

Table 2.2 Nozzle dimensions

Nozzle	$\frac{A_{exit}}{A_{throat}}$	Exit Diameter d_e (in)	Throat Diameter d_c (in)
A	1.00	0.236	0.236
B	1.00	0.197	0.197
C	1.00	0.157	0.157
D	1.00	0.118	0.118
E	1.78	0.157	0.118
F	2.04	0.159	0.111
G	2.03	0.318	0.223

2.1.4. The Leakage Gap

The gap between the main chamber (jet entrance face) and the pre-chamber (nozzle exit face) can be varied. This gap, which simulates the gap between the channel ends in the rotor and the endplate, is defined as the leakage gap in wave rotor literature. To facilitate the objectives of constant-volume combustion, this gap should be as small as possible. It may not be possible to maintain a hermetic contact between the two surfaces moving at relative velocities to each other. This seal should also maintain a physical gap to compensate for thermal expansion of the rotor in a wave-rotor combustor. Wilson et al. [33, 34] recommended maintaining a leakage gap lesser than one hundredth of the channel height. Due to the machining inaccuracies, bearing play, and the mechanism used to clamp the main chamber onto the rig base, the gap between the pre-chamber and the main chamber could not be entirely eliminated for the experiments in the current study. The leakage gap was maintained below the limit specified by Wilson for each experiment conducted and this will be discussed in later chapters.

2.2. Ignition System

The ignition system was used to initiate combustion inside the pre-chamber. The main components of the ignition system were the battery, the spark plug, the capacitive

discharge ignition (CDI) system, the ignition coil, and the trigger button as illustrated in Figure 2.8. A DC battery of 12 V was used as the power supply to the ignition system. The ignition arm toggle switch was used as a safety precaution to disable the system from sparking when the toggle switch was in the "off" position. All the negative connections were routed to a common ground (GND) including the digital ground (DGND) of the data acquisition system.

A Champion brand RC11ZYC4 model spark plug was used with the maximum spark gap recommended by the manufacturer 0.045 in for stable and reliable ignition in the pre-chamber. The spark plug high-tension cable routed from the ignition coil was connected to the copper rod using a sliding contact to allow rotary motion of the pre-chamber for rotary experiments. The copper rod was installed in the axial hole pre-drilled in the pre-chamber drive shaft. To avoid sparking between the copper rod and the steel drive shaft, a plexiglass tube was used to insulate the copper rod in the drive shaft.

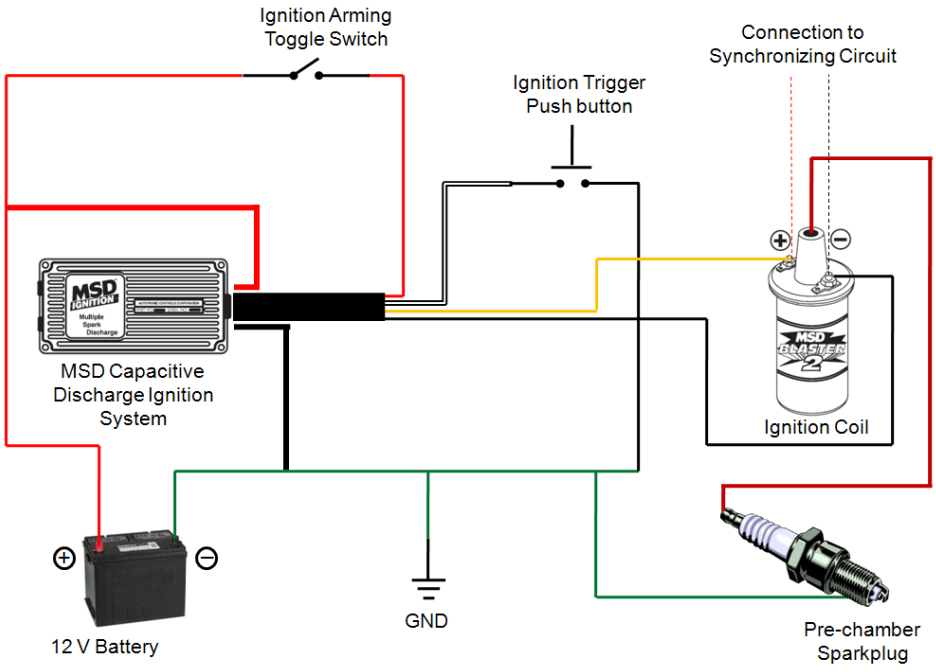

Figure 2.8 Schematic diagram of the ignition system

An MSD CDI system was used in conjunction with the MSD blaster 2 ignition coil to produce the high voltage current required for the spark plug. Although the CDI system was not essential for the stationary experiments conducted in the current study, the high-voltage induced in the secondary coil due to the higher voltage supplied by the CDI system on the repetitive triggering using the push button.

The induced secondary high-voltage current in the ignition system was routed to the synchronization circuit to initiate both the data acquisition and the high-speed video camera. Therefore the delay in the ignition circuit from the time when the push button was triggered to when the secondary high-voltage current was induced in the system was of no consequence for experiment and the acquired data. The signal generated in the ignition system to the push button trigger is illustrated in Appendix C. This indicates that the ignition system is triggered with the pressing of the push button without a delay.

2.3. Data Acquisition System

The data acquisition system was made up of the fast-response pressure transducer data acquisition system and the high-speed video camera control and image capture system.

2.3.1. Pressure Transducers

Five PCB Piezotronics$^{INC.}$ ICP® high frequency-general purpose 113A32 dynamic pressure transducers were used for the current study. One of the pressure transducers was used to measure the pressure in the pre-chamber and the other four for were used to measure the spatial pressure variation along the main chamber. The pressure transducer specifications are attached in Appendix H.

2.3.2. National Instruments Data Acquisition System

The data acquisition system comprised of National Instruments NI SCXI-1000 4-slot chassis with a NI SCXI-1530 4-channel ICP® (Intergrated Circuit-Piezo Electric) accelerometer module, to acquire the data from the 113A32 dynamic pressure transducers and a NI SCXI-1302 50-pin feedthrough terminal block, used to initiate the data acquisition process based on the input signal from the synchronizer circuit. The signals were routed through a NI SCXI-1180 feedthough panel and a NI SCXI-1349 adapter to a NI PCI-6251 M-series data acquisition device connected to a computer. A schematic of the data acquisition system is given in Figure 2.9. National Instruments LabVIEW Developer Suite™ 2009 was used to develop a virtual instrument (vi) that controls the hardware in the data acquisition system.

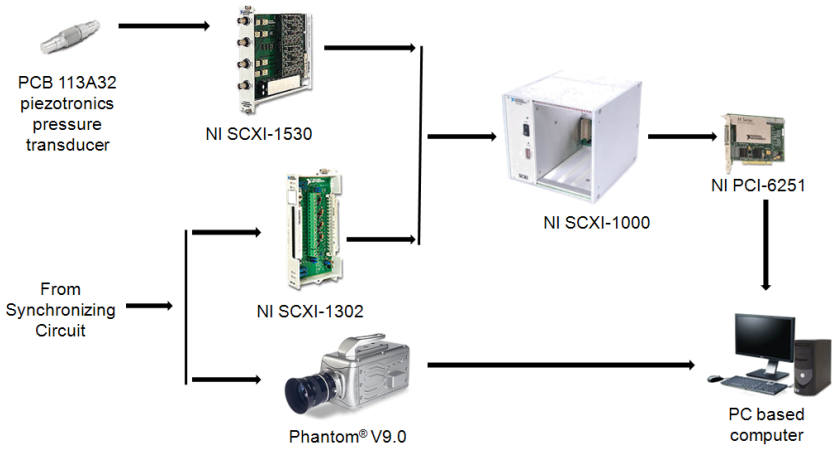

Figure 2.9 Schematic data acquisition

2.4. Phantom v9.0 High-Speed Video Camera

The Vision Research^INC. Phantom® v9.0 monochrome camera was used to acquire high-speed video of the experiment through the optical window in the main chamber. The camera sensor specifications and spectral response curve are given in Appendix D. The camera is capable of capturing 144,175 frames per second (fps) and a maximum resolution of 1632 × 1200 pixels. All experiments were conducted at 10,000 fps to be synchronized with the fast response pressure data acquisition system. The camera was

accessed and controlled using Phantom® camera control software, software revision 675. The Nikon F-AF Nikkor 50 mm f/1.8 D lens was mounted on the high-speed video camera with the f-number 1:1.8. The exposure time set to 96.75 μs and EDR (Extreme Dynamic Range) exposure at 0 μs. Setting EDR exposure time to 0 μs, the exposure levels at time of triggering of the camera was used as the reference for exposure levels for the entire series of captured video. The exposure time was the duration the object in the field of view of the camera is exposed to the camera sensor between each time increment. This can be explained using the example below. At 10,000 fps the camera sensor is exposed to the object for a duration of 96.75 μs every 100 μs. The reasons for using a high exposure time and an f-number were due to the importance of exposing the sensor to the slightest illumination in the main chamber gas mixture to determine ignition. These exposure rates and the f-number would have to be different for rapid flame propagation in order to eliminate the motion blurring that occurs where in the same image frame multiple flame positions of the propagating flame are recorded.

2.4.1. Laser Alignment System

The camera resolution is in inverse proportion to the frame rate. As an example the camera is capable of capturing video at 1,000 fps at resolution of 1632 × 1200 pixels. When the frame rate was increased to 10,000 fps the resolution reduced to 1152 × 152 pixels. This resolution covers a rectangular area encompassing the optical window if the camera lens is placed approximately 5 ft from the optical window in the main chamber. In order to align the camera lens vertical and horizontal symmetric lines with the vertical and horizontal lines of the optical window, two laser line generators were used on a machined setup which can be mounted on the Phantom v9.0 camera. The design drawings of the laser alignment system are in Appendix E. The procedure followed for aligning the camera using the laser system begins with the Phantom® camera control software. The camera was used with its maximum square resolution at 1200 × 1200 pixels at 1,236 fps and 805.75 μs exposure time.

With the laser line generators switch “On” and observing the deviation from the horizontal and vertical cross-hair on the screen, the alignment laser generator orientation was adjusted until each align with the corresponding cross-hair line (Figure 2.10 (a) and (b)). After the laser line generators were aligned the level of the rig was measured using a bubble level and required adjusts are made to the main chamber level by inserting shim stock between the racers and H-beam guide.

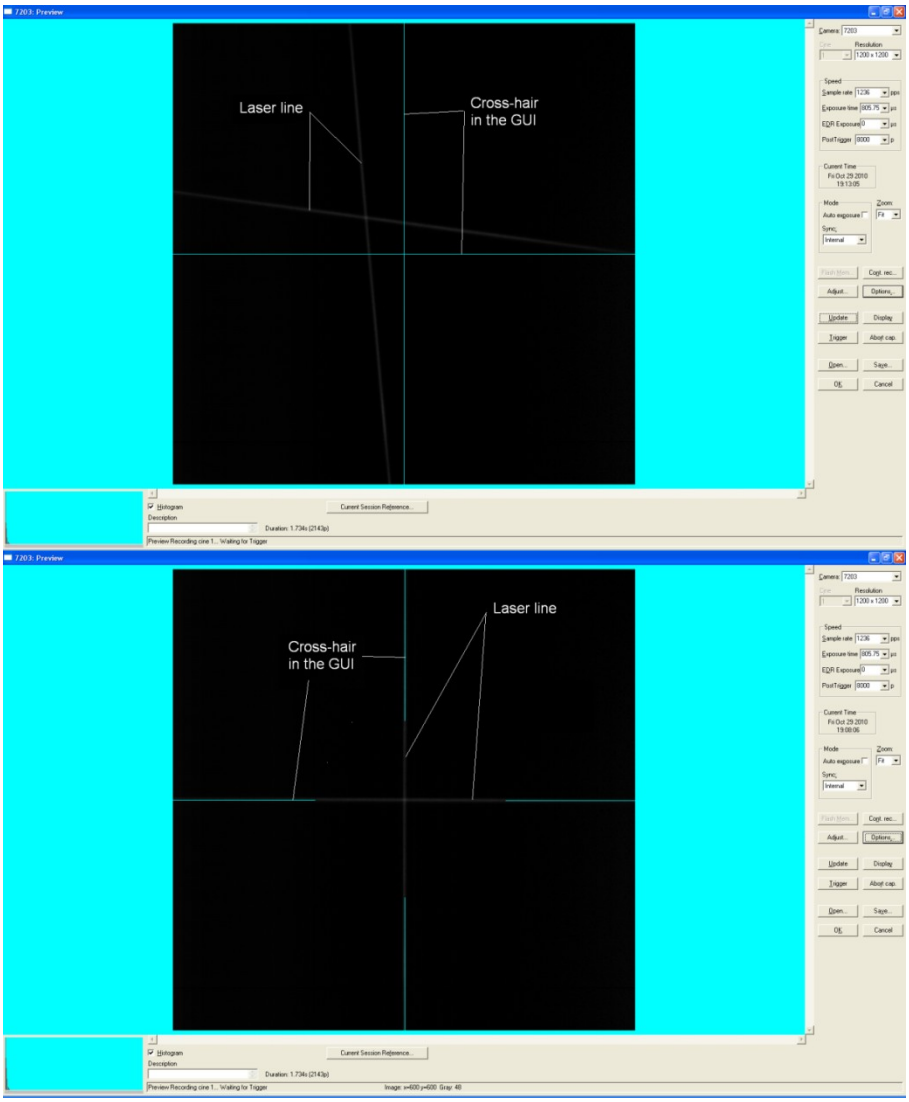

Figure 2.10 Laser alignment: (top) before alignment of the laser line generators (bottom) after alignment

Then the camera tripod was leveled observing the bubble levels available at each stage of the tripod and the laser alignment setup using the adjusting screws on the tripod as necessary to ensure proper level (Figure 2.11). Finally, the camera height and any required fine adjustments to the tripod adjusters were carried out using the laser lines projected onto the main chamber as illustrated in Figure 2.11 (a) and (b).

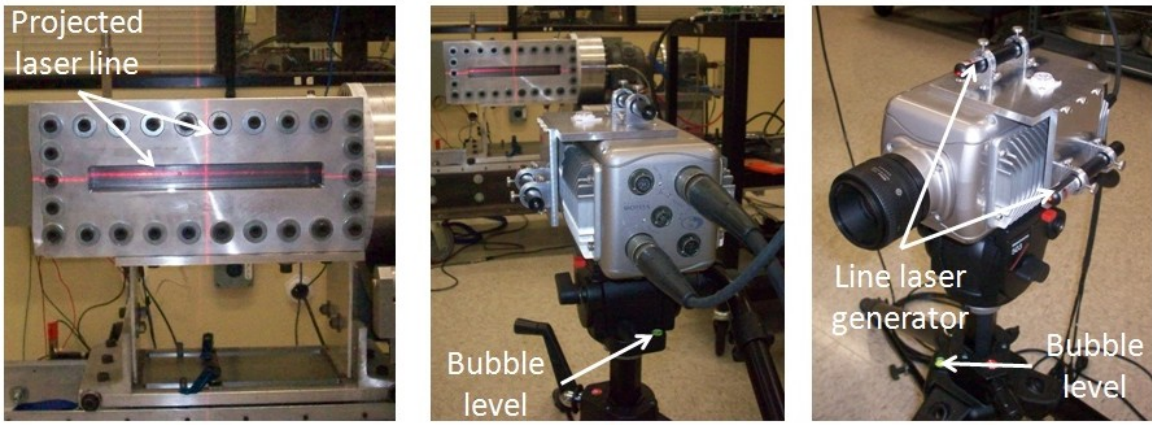

Figure 2.11 High-speed video camera with laser alignment system: (a) the projected laser lines on the main chamber optical window, (b) the view of the camera and the with the main chamber, and (c) the camera with the laser alignment system mounted on

2.5. Fueling System

The fueling system used in the experiments is shown in Figure 2.12. This fueling system was used to fuel both pre-chamber and main chamber for all experiments. Capable of preparing mixtures of fuel-air ratios between multiple fuels and air, the current system is even capable of preparing higher pressure and vacuum pressure initial mixtures. Before each experiment both the pre-chamber and the main chamber were purged using compressed air for over 30 minutes. Then the pre-chamber was hermetically sealed using the nozzle insert sub-assembly and the main chamber was sealed using the latex diaphragm and the plate assembly, as explained earlier in the chapter. The pre-chamber was fueled first, using a vacuum pump to pull vacuum pressure of more than 10.00 psig (gauge pressure) and filling the pre-chamber with the required fuel type and

the predetermined equivalence ratio based on partial pressure method. The partial pressure method will be explained in the next chapter.

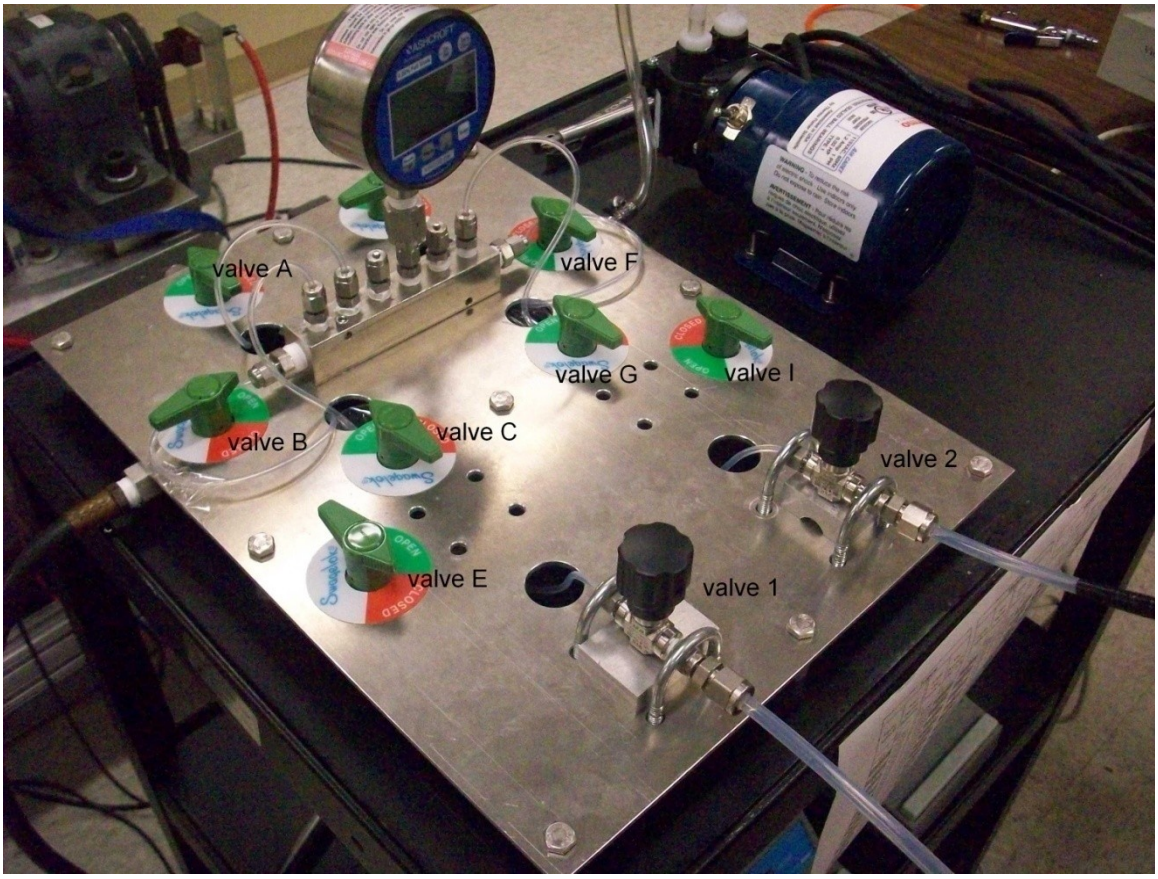

Figure 2.12 Fueling system

Assuming the fuel was connected to the flow-control valve 1 in the Figure 2.13, and all other valves are closed, the fuel flow would be passed through the open quarter-turn plug valves C and A and into the pre-chamber. After filling the pre-chamber with the required amount of fuel, flow-control valve 1 will be closed and valve E would be opened to bring the pressure in the pre-chamber up to atmospheric pressure. The quick-connect valve would be disengaged and the entire system would be vacuumed and then purged for at least 5 minutes before all the valves are closed once again and the quick-connect valve was connected to the main chamber fueling port. The process of fueling was identical to the procedure followed in fueling the pre-chamber.

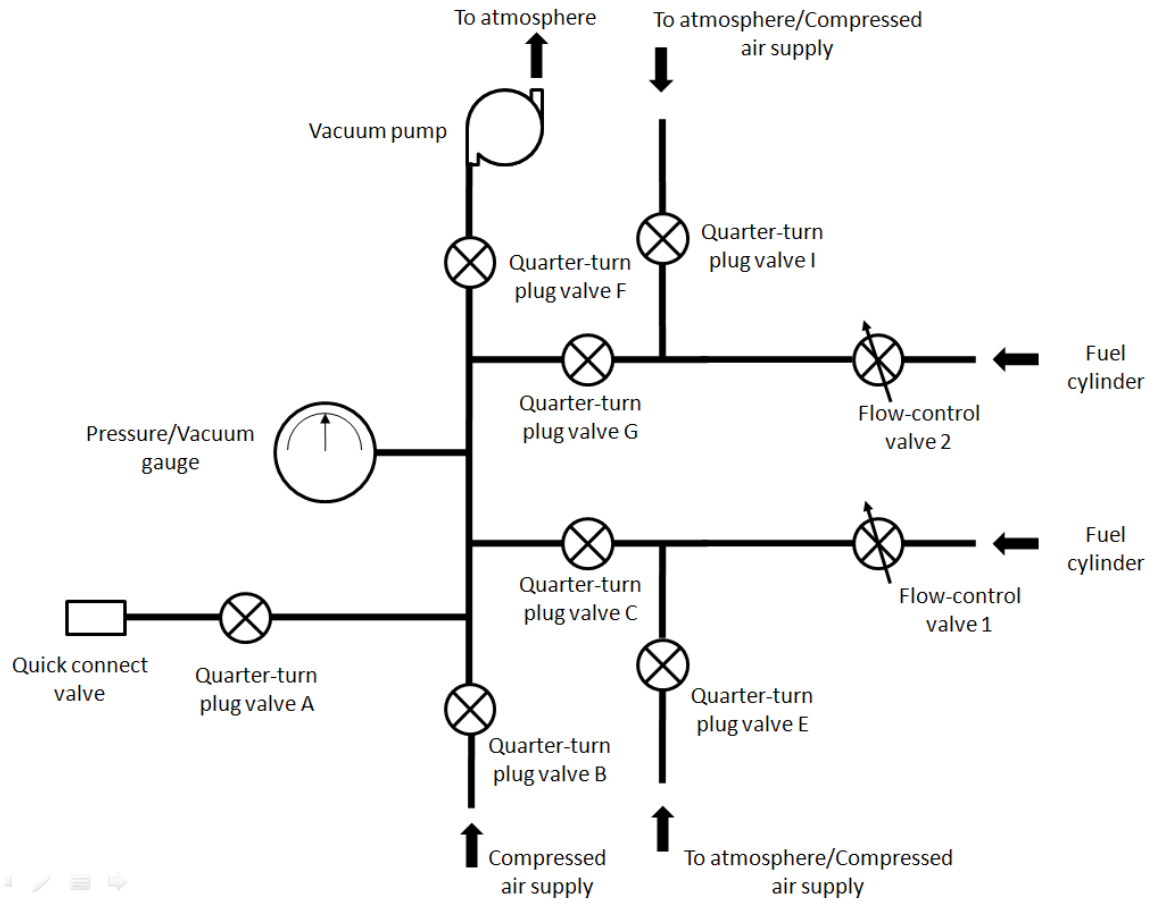

Figure 2.13 Schematic diagram of the fueling system

2.6. Aluminum Diaphragm Scoring Setup

The scoring of the aluminum diaphragms were carried out by a 50050 Score One™ glass cutter illustrated in Figure 2.14. A sliding bed was designed and fabricated to minimize the scoring depth variation of the aluminum diaphragms. This scoring depth variation was a critical experimental variable which needed to minimized. The design drawings of the sliding bed are attached as Appendix F.

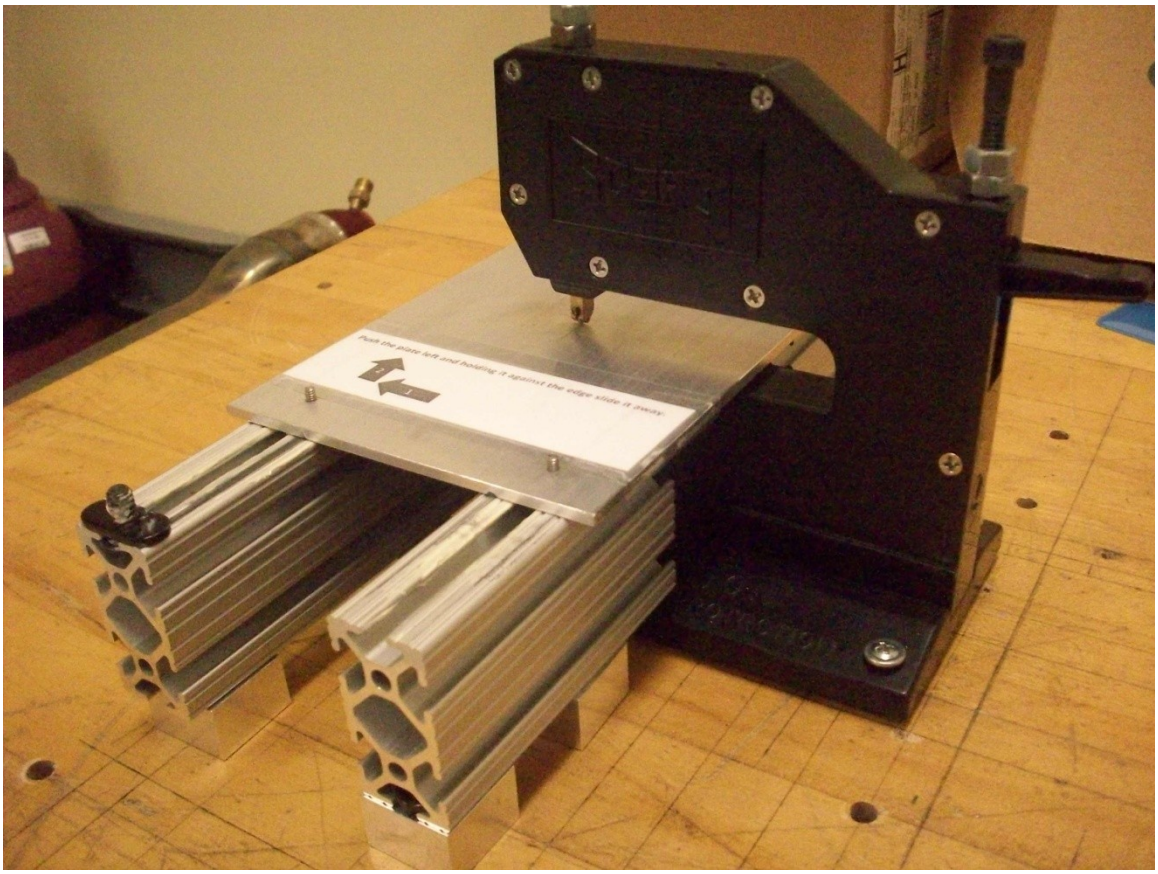

Figure 2.14 Diaphragm scoring mechanism

CHAPTER 3. PRELIMINARY EXPERIMENTS

This chapter explains the preliminary experiments conducted that were required to identify the relevant experimental variables and their ranges before the main experimental study was carried out.

3.1. Fueling System Leakage Test and Partial Pressure Calculation

A new fueling system was built for this study to ensure no leakage. The description of the fueling system and the fueling process was explained in Section 2.5. Any leak in the fueling system can contribute towards variations in fuel-air mixtures prepared in the pre-chamber and the main chamber. In the fueling process a specific predetermined amount of fuel has to be supplied in order to prepare a mixture of required equivalence ratio; in leakage of air would make a leaner mixture than that was intended.

If this leakage in the fueling system cannot be eliminated, the leakage may be measured to allow the fuel-air mixture values to be corrected. Therefore the leakage in both the pre-chamber and the main chamber were individually measured under the same vacuum conditions the chambers are subjected to in the fueling process. With each chamber connected to the fueling system independently, the pre-chamber and the main chamber pressure variation and the total error at each measurement are indicated in Figures 3.1 and 3.2 respectively.

An ASHCROFT® 2074 digital industrial gauge was used to measure the pressure in the fueling system. The full-scale terminal point accuracy of the gauge was 0.25% that included hysteresis, linearity, and repeatability. The accuracy also allowed zeroing of the

gauge at start-up to eliminate any sensor offset. The accuracy of the gauge leading to a 0.0375 psi variation of the measured pressure.

The pre-chamber vacuum pressure dropped 0.004 psi in 10 minutes and the main chamber vacuum pressure dropped 0.006 psi in 10 minutes. The average time to fuel each chamber was 35±10 s and 32±9 s for pre-chamber and main chamber respectively. There were only two occasions the fueling time exceeded 60 s with the maximum time being 67 s. Therefore, the effect of leakage of vacuum pressure on the equivalence ratio was neglected and no corrections on the equivalence ratios were performed. For the maximum drop in vacuum pressure of 0.006 psi in either chamber during the fueling time, would only lead to a 0.7% error in the equivalence ratio, if near stoichiometric.

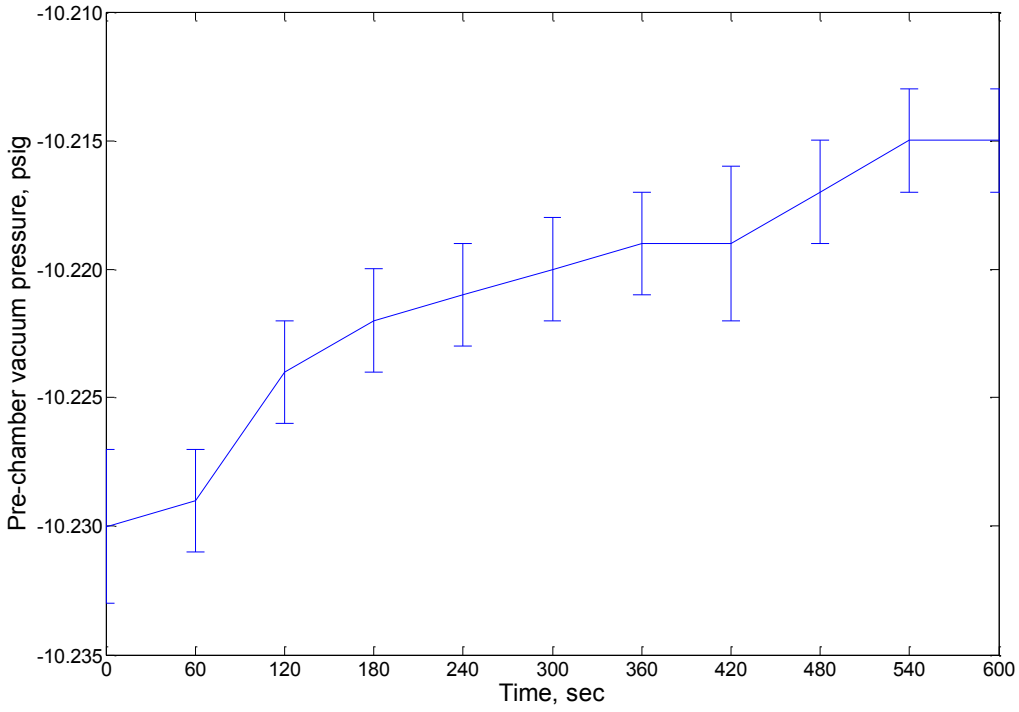

Figure 3.1 Pre-chamber vacuum pressure variation with total error

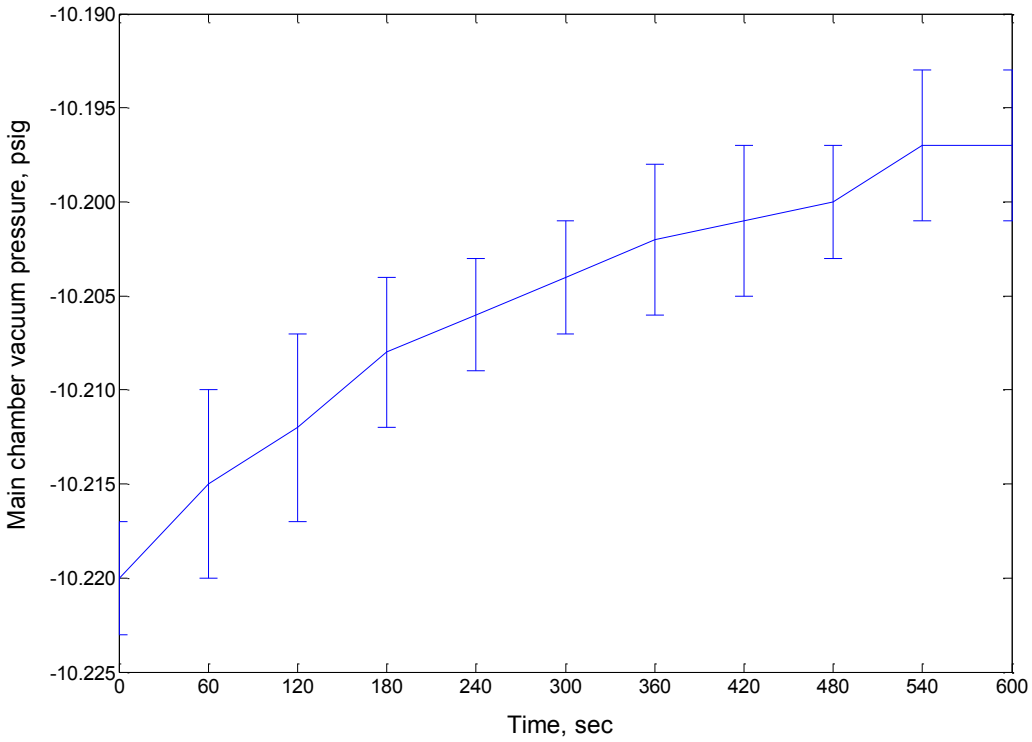

Figure 3.2 Main chamber vacuum pressure variation with total error

Dalton's partial pressure law was utilized in preparing the fuel-air mixtures. The law states that the total pressure of a mixture of gases is equal to the sum of the individual gas partial pressures, which are the pressures of individual gases if it was occupying the same volume now occupied by the gas mixture.

$$P = \sum P_i = \sum \chi_i P \qquad \text{Eq. 3.1}$$

P is total pressure of the mixture, P_i is the partial pressure of the i^{th} component in the mixture assuming the i^{th} component occupied the same volume occupied by the total gas mixture, and χ_i is the mixture concentration in mole fractions.

It is desired to calculate the required amount of fuel for a predetermined equivalence ratio, say ϕ defined as in Equation 3.2 below,

$$\phi = \frac{(A/F)_{stoichiometric}}{(A/F)} = \frac{(F/A)}{(F/A)_{stoichiometric}} \qquad \text{Eq. 3.2}$$

where (A/F) is defined as air/fuel mass ratio and (F/A) is defined as fuel/air mass ratio. Air is assumed to be a mixture of one mole of O_2 to 3.76 moles of N_2. Therefore if the intended fuel is a hydrocarbon fuel, C_xH_y the balanced chemical reaction for complete combustion of the fuel in atmospheric air would be,

$$C_xH_y + \left(x + \frac{y}{4}\right)(O_2 + 3.76N_2) \rightarrow xCO_2 + \frac{y}{2}H_2O + \left(x + \frac{y}{4}\right)3.76N_2 \qquad \text{Eq. 3.3}$$

Therefore the stoichiometric air-fuel ratio is,

$$(A/F)_{stoichiometric} = \frac{4.76\left(x + \frac{y}{4}\right)}{1}\frac{MW_{air}}{MW_{C_xH_y}} \qquad \text{Eq. 3.4}$$

Since the equivalence ratio, ϕ is known, using Equation 3.2 the air-fuel ratio for the desired equivalence ratio can be calculated as,

$$(A/F) = \left(\frac{4.76\left(x + \frac{y}{4}\right)}{1}\frac{MW_{air}}{MW_{C_xH_y}}\right)\Big/\phi \qquad \text{Eq. 3.5}$$

Representing any combustion reaction between the fuel in question and air represented by the reaction below,

$$C_xH_y + z(O_2 + 3.76N_2) \rightarrow \text{combustion products} \qquad \text{Eq. 3.6}$$

The unknown mole ratio, z of the air-fuel can be evaluated by,

$$z = (A/F)\frac{1}{4.76}\frac{MW_{C_xH_y}}{MW_{air}} \quad \text{Eq. 3.7}$$

Since the mole fraction in the required mixture is known, the mixture composition by mole fraction can be found as,

$$\frac{N_{air}}{N_{C_xH_y}} = z \rightarrow \frac{N_{C_xH_y}}{N_{C_xH_y} + N_{air}} = \frac{1}{1+z} = \frac{N_{C_xH_y}}{N_{total}} = \chi_{C_xH_y} \quad \text{Eq. 3.8}$$

and partial pressure can be related to the mixture composition and total pressure by the equation,

$$P_i = \chi_i P \quad \text{Eq. 3.9}$$

The required partial pressure for the fuel can be evaluated by substituting the partial pressure and the mixture concentration of fuel in Equation 3.9,

$$P_{C_xH_y} = \chi_{C_xH_y} P \quad \text{Eq. 3.10}$$

3.2. Diaphragm Material and Diaphragm Thickness

The aluminum diaphragm used in all the experiments was aluminum alloy 1100, which was 0.003±0.0003 in thick. All diaphragms were scored using the scoring mechanism described in Section 2.6 and assembled between the nozzle and the nozzle plate. This nozzle assembly was then fixed into the pre-chamber nozzle cavity (Figure 2.3 (e)). The pre-chamber pressure rise due to combustion ruptured the aluminum diaphragm. The 0.003 in diaphragm did not rupture unless it was scored at maximum pressure in the pre-chamber. Diaphragms made of the same aluminum alloy with thicknesses

0.004±0.0004 in and 0.005±0.0004 in were tested in preliminary experiments. These thicker diaphragms were scored using the same scoring mechanism used in scoring the 0.003 in aluminum diaphragm, but did not rupture. It was decided to use the 0.003 in thick aluminum diaphragm as the diaphragm material.

Mylar® polyester (PET) films of 0.002±0.0002 in, 0.003±0.0003 in, and 0.005±0.0005 in thickness were tested with prolonged diaphragm rupture time. This was due to the diaphragms melting from the combustion heat release compared to being ruptured from the pressure rise. This prolonged duration time was deemed not suitable for the torch jet studies with the current experimental setup. In addition to this the melting/burning of the polyester film produces chemical species which might lead to experimental variations that cannot be accounted for with the current experimental setup.

The latex diaphragm used in the main chamber was ruptured rather than being burned through by the impinging torch jet. Therefore the latex diaphragm was assumed not to contribute towards producing chemical products which might have affected the re-ignition of the combustible fuel-air mixture in the main chamber. This was based on the visual inspection of the remains of the latex diaphragm where the torn edges facing the pre-chamber side were not burnt nor melted. However, some broken off and melted latex diaphragm particles were found at the end of experiments inside the main chamber. These latex particles were assumed to melt due to the combustion in the main chamber. All experiments were conducted with 0.006±0.002 in thick with a durometer rating of 40A±5 natural latex rubber films were used to produce all the main chamber diaphragms.

3.3. Pre-Chamber Diaphragm Assessment

The pre-chamber rupture time is of great significance to the experiment because the constituents of the torch jet include both combustion products and radicals to varying degrees depending on the time of rupture. The diaphragm rupture is directly dependent on the pressure rise in the pre-chamber which depends on the amount of fuel-air mixture burnt as time passes after the ignition of the mixture with the sparkplug. At the time of

rupture if the combustion products with radicals are injected into the main chamber through the nozzle, the combustible mixture in the main chamber will ignite after a shorter ignition delay as compared to if the jet was made up of completely combusted, inert combustion products. The amount of radicals generated varies with the fuel type used in the pre-chamber which in turns governs the main chamber ignition process.

To evaluate the diaphragm rupture time, a numerical analysis of the high-frequency pressure measurements were conducted and validated with the high-speed video images. A series of tests were conducted with the camera field of vision aligned axially looking directly into the pre-chamber through the nozzle cavity as indicated in the top right of Figure 3.3. This image was taken under room lighting conditions at 256 × 256 resolution, frame rate of 30 fps, exposure time of 10,000 μs, and EDR exposure of 0 μs. The experimental video was captured at the same resolution at frame rate of 10,000 fps (time interval between frames 100 μs) with the lens aperture set to an f-number of 1:1.8 and the exposure time of 96.75 μs and EDR exposure of 0 μs. The images obtained for 7 experiments off the series of experiments are shown in Figure 3.3. The number at the left bottom corner of each frame indicates the relative frame number from trigger signal of the ignition system in the pre-chamber. The high-speed video were captured with lights turned off in the laboratory, and the luminous region detected in the frames are the self illumination of the combustion gases in the pre-chamber. The red circles indicate the first frame illumination from inside the pre-chamber was detected in each preliminary experiment. The diaphragms were scored with the use of the diaphragm scoring mechanism described in Section 2.6. The diaphragms were scored to different depths in order to check the reliability of the numerical method used to compute the diaphragm rupture time in the pre-chamber.

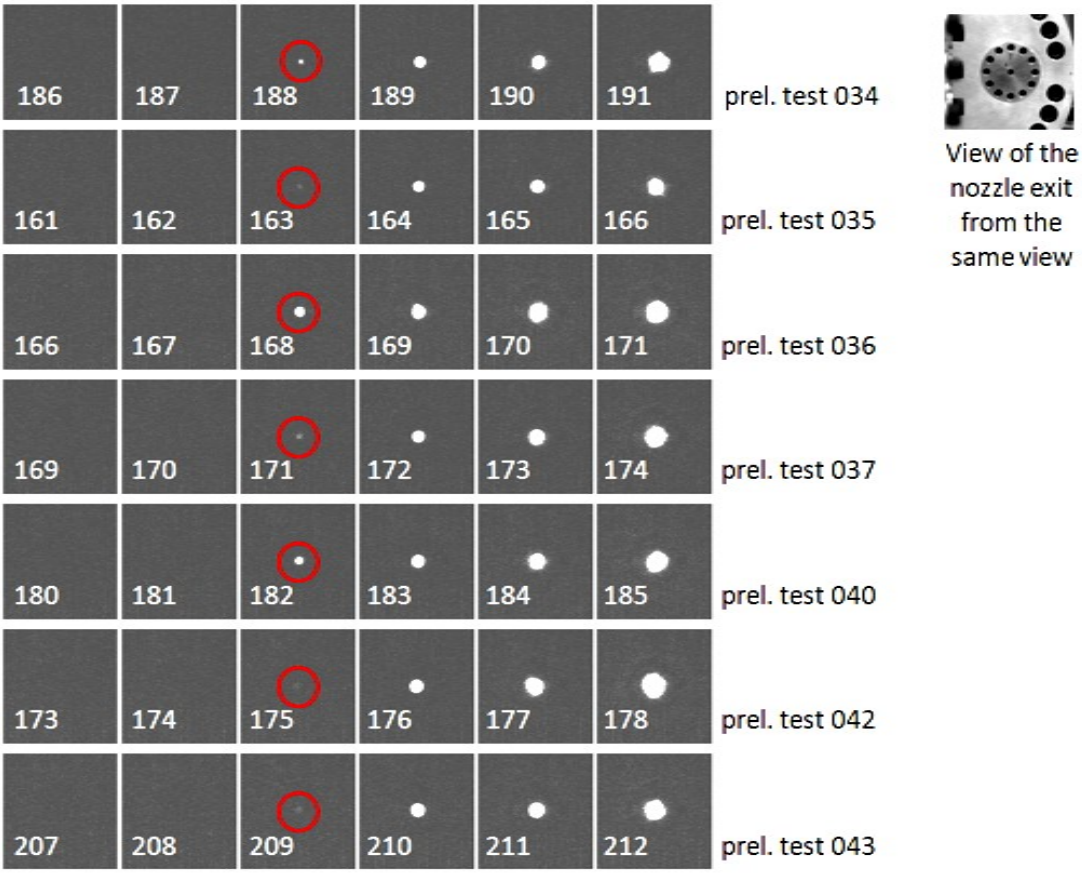

Figure 3.3 High-speed images of the pre-chamber torch jet exit

In order to numerically analyze the diaphragm rupture time a simple MATLAB® numerical code was used. The pressure transducer (PT-0 pressure transducer) history inside the pre-chamber was used to develop a polynomial curve fit for the measured pressure history. The order of the polynomial is decided upon the lowest possible value for the summation of difference squared terms between the polynomial curve fit values and the measured pressure data at each time instance the measurements were recorded. These polynomial values are used to calculate the pressure gradient with time at every time instance. A typical plot obtained from the numerical analysis used to evaluate the diaphragm rupture time using the pressure history is shown in Figure 3.4. The time

instant corresponding to the maximum value for the pressure-time gradient correlated with the visual detection of luminosity from the pre-chamber.

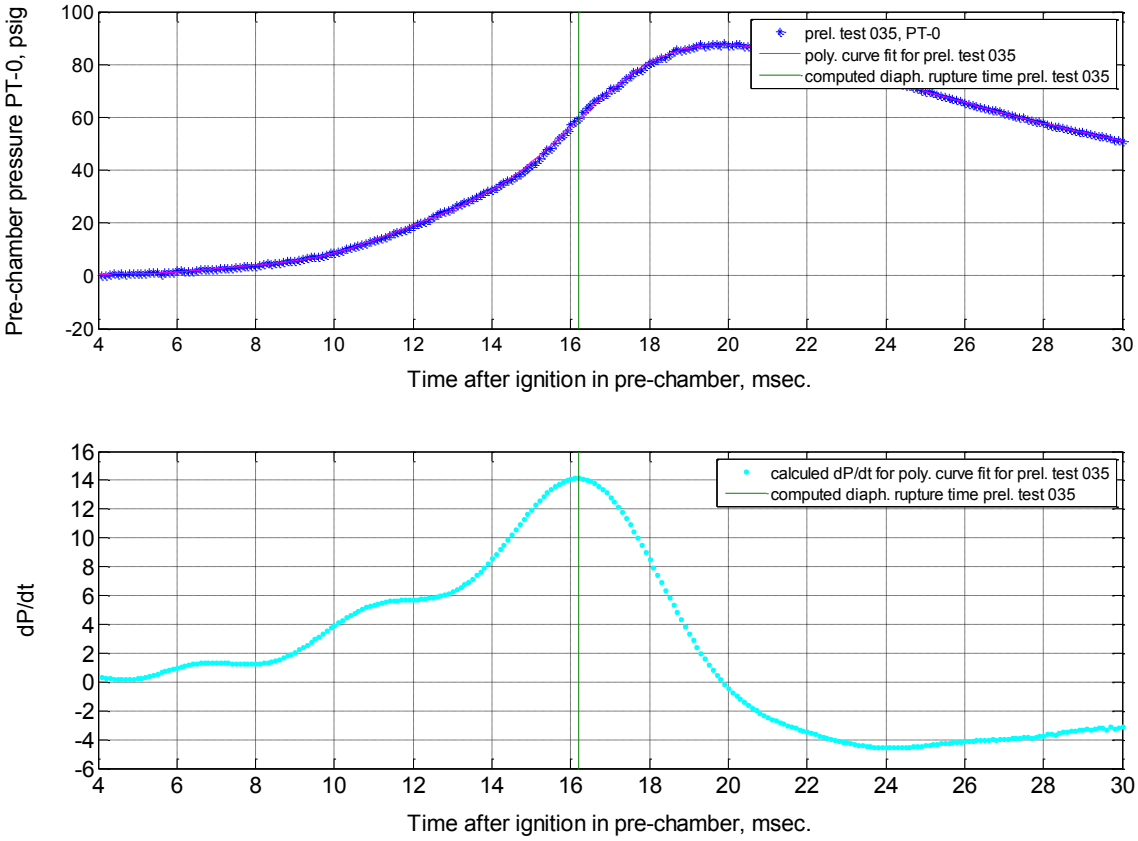

Figure 3.4 Output plot of the numerical analysis for evaluating diaphragm rupture time using pressure history in the pre-chamber

Comparison of the visual inspection and the computed diaphragm rupture time for this series of tests are illustrated in Figure 3.5. The pressure in the pre-chamber is controlled by the amount of combustible mixture in the pre-chamber, the heat loss to the pre-chamber, mass outflow through the open nozzle, and the expansion fan propagating into the pre-chamber when the diaphragm ruptures. The heat loss can be neglected as the heat transfer time scales are high compared to the experimental observation times. This was verified by tests carried out using polyester diaphragms, which took approximately 5 times the time needed to rupture the aluminum diaphragm under the same pre-chamber

conditions. The polyester diaphragms burned due to the heat of the reactions in the pre-chamber but still held the pre-chamber mixture without failing for a longer time than the typical diaphragms used in these experiments. This leads to the conclusion about the heat transfer from the combustion in the pre-chamber to the surrounding material is slow compared to the experiment observation time. The amount of mass outflow through the nozzle is negligible immediately after diaphragm rupture. This is due to there being no mass outflow until the diaphragm rupture event. This mass outflow subsequently leads to the pressure drop inside the pre-chamber as time progresses. Therefore the mass outflow, the expansion fan propagation into the pre-chamber and the reduction in the pressure rise due to the depletion of the combustible mixture in the pre-chamber are the only plausible explanations.

The diaphragm rupture time, diaphragm rupture pressure, and pre-chamber maximum pressure are given in tabular form for some preliminary experiments conducted in Table 3.1. The diaphragm rupture time variation is due to the different reaction rates of the fuel types used, where methane is slow to combust compared to ethylene which is the easiest to combust. This is indicated by ethylene mixtures having the lowest rupture time with a mean of 14.7±0.2 ms, while propane has a mean rupture time of 28.7±0.4 ms, and methane having a 39.6±1.6 ms average rupture time. The diaphragm rupture pressure for these fuels varied around an average of 53.3±1.3 psig which is independent of the fuel type as well as equivalence ratio. The maximum pressure was recorded for ethylene mixtures with an average pressure of 92.3±1.0 psig. The propane mixtures had an average maximum pressure of 77.9±0.3 psig while methane had the lowest average maximum pressure of 68.7±1.3 psig.

It was expected that combustible mixture is still present after diaphragm rupture, since the pressure keeps increasing inside the pre-chamber. After the diaphragm rupture event, ethylene showed a 73% increase in pressure from diaphragm rupture pressure after the diaphragm rupture. Methane maximum pressure increased 29% from the diaphragm rupture pressure and propane maximum pressure increased by a 46%. This led to the

conclusion that the propagating expansion fan leads to the reduction in the pressure gradient after the diaphragm rupture in the pre-chamber.

Table 3.1 Diaphragm rupture time, pressure, and maximum pre-chamber pressure

Fuel type	Equivalence ratio, ϕ	Diaphragm rupture time (ms)	Diaphragm rupture pressure (psig)	Pre-chamber max. pressure (psig)
Methane	1.1	39.9	51.7	67.9
Methane	1.1	39.9	52.9	69.6
Methane	1.1	37.4	52.9	69.9
Methane	1.1	41.1	51.3	67.3
Ethylene	1.1	15.1	56.3	93.7
Ethylene	1.1	14.9	53.5	91.0
Ethylene	1.1	14.9	54.7	93.5
Ethylene	1.1	14.6	54.3	93.3
Ethylene	1.1	14.7	53.6	91.6
Ethylene	1.1	14.7	54.3	92.5
Ethylene	1.1	14.6	54.8	92.6
Ethylene	1.1	14.6	53.8	92.5
Ethylene	1.1	14.4	52.9	91.0
Ethylene	1.1	14.5	53.1	91. 8
Propane	1.1	29.0	52.2	77.8
Propane	1.1	28.8	53.1	78.3
Propane	1.1	28.2	51.2	77.6

The predicted diaphragm rupture times from the numerical analysis is compared with the high-speed video images of the same experiment and presented in Figure 3.5. The numerical method was able to predict the rupture time of the diaphragm where the largest deviation was 300 μs in preliminary test number 037 and 040. The average deviation was 130±116 μs. This can be attributed to the time resolution of the high-speed image capture rate and the data acquisition rate as well as the numerical errors of curve-

fitting the experimental pressure data along with subsequent calculations on these curve fit data. The variations of the ignition delay times for the different preliminary tests were due to the variation in the diaphragm scoring depth that was done deliberately to check the reliability of the numerical analysis method to predict the diaphragm rupture time. For these preliminary tests the initial pressure, initial temperature, and the initial equivalence ratio were maintained at atmospheric pressure, room temperature, and 1.1 respectively.

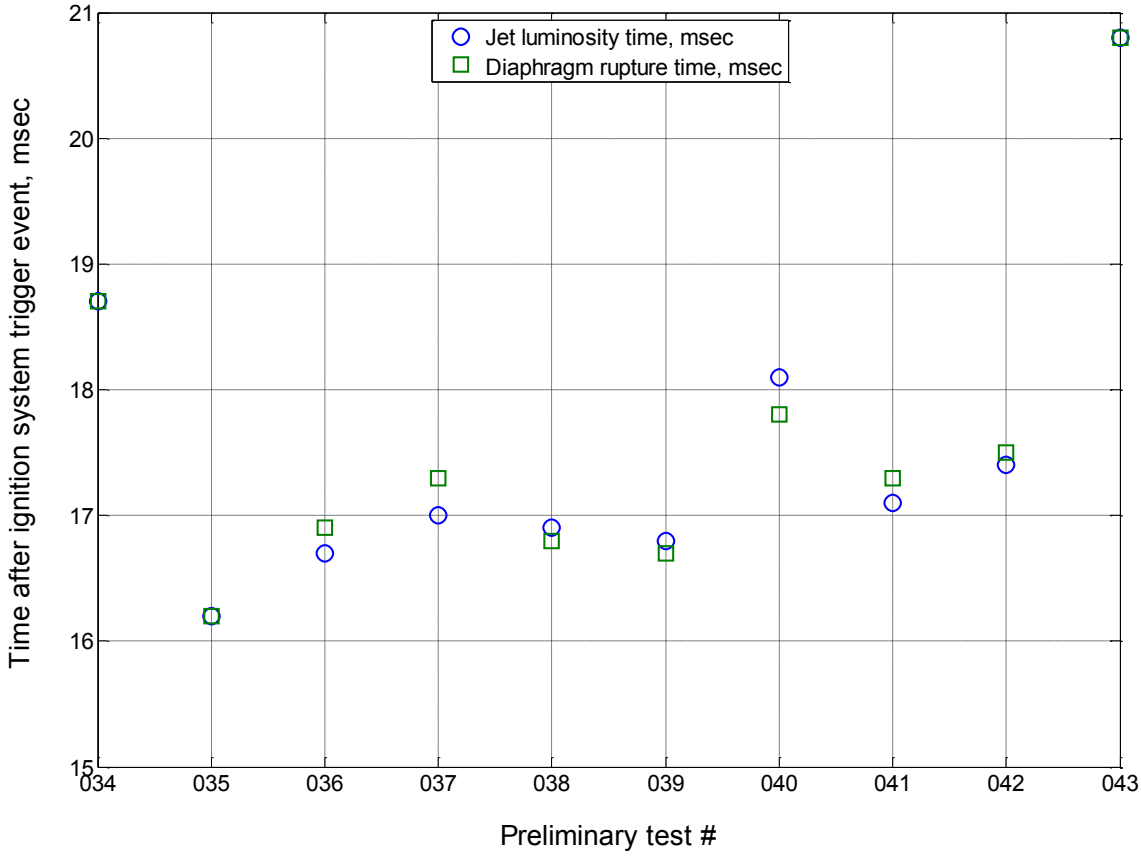

Figure 3.5 Diaphragm rupture time assessment

3.4. Repeatability of Experiments

Experimental repeatability was tested with ethylene-air mixtures in the pre-chamber to check the reliability and consistency of the torch jet produced. A series of preliminary tests numbers from 11 to 20 were conducted to evaluate the pressure history, diaphragm rupture time, diaphragm rupture pressure, and max-pressure of the pre-

chamber. The initial pressure and initial temperature were maintained at atmospheric pressure and room temperature. The equivalence ratio was held constant at 1.1. The pressure histories of these 10 preliminary tests are similar to one another as illustrated by Figure 3.6.

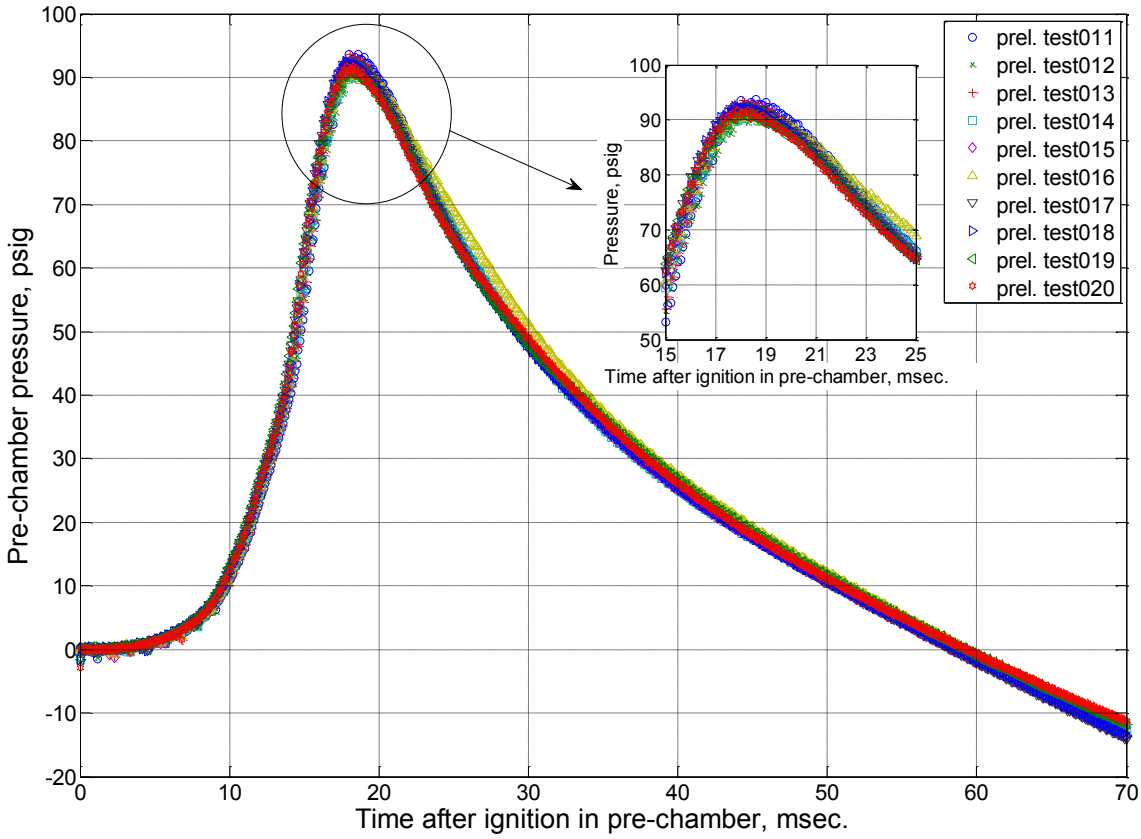

Figure 3.6 Pressure time history after ignition in the pre-chamber

Another series of preliminary experiments were conducted to observe the reliability and repeatability of the experiment by varying the equivalence ratio inside the pre-chamber. The initial pressure and temperature were maintained at atmospheric pressure and room temperature respectively. The results of these preliminary tests are illustrated in Figure 3.7. Preliminary test 015, 016, and 017 at equivalence ratio 1.1 had the highest pressure gain followed by the tests with equivalence ratio 0.9. The fuel-rich

preliminary tests 050 and 051 took a slightly longer time to reach the maximum pressure compared to mixtures with equivalence ratio 1.1.

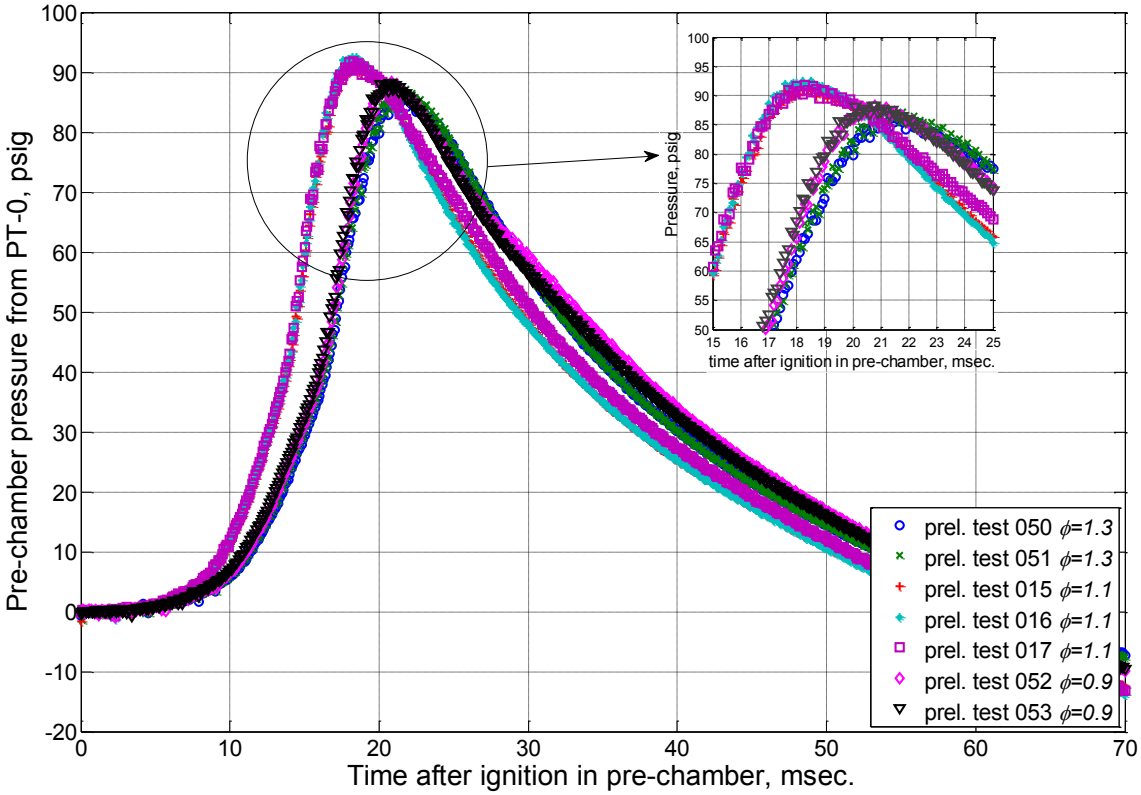

Figure 3.7 Pressure histories inside the pre-chamber for test with different equivalance ratios

The aluminum diaphragm rupture times, diaphragm rupture pressures, and maximum pressure reached in the pre-chamber for the ethylene preliminary tests from Table 3.1 are illustrated in Figure 3.8 to Figure 3.11. The diaphragms were scored with the same settings to maintain similar diaphragm conditions to maintain similar diaphragm rupture times. The range of diaphragm rupture time varies from 14.4 to 15.1 ms, with a mean 14.7 ms with a 0.2 ms standard deviation. The similar rupture times ensure the constituents of the torch jet are similar and therefore the variations in the re-ignition in the main chamber are relatively independent of the torch jet variations.

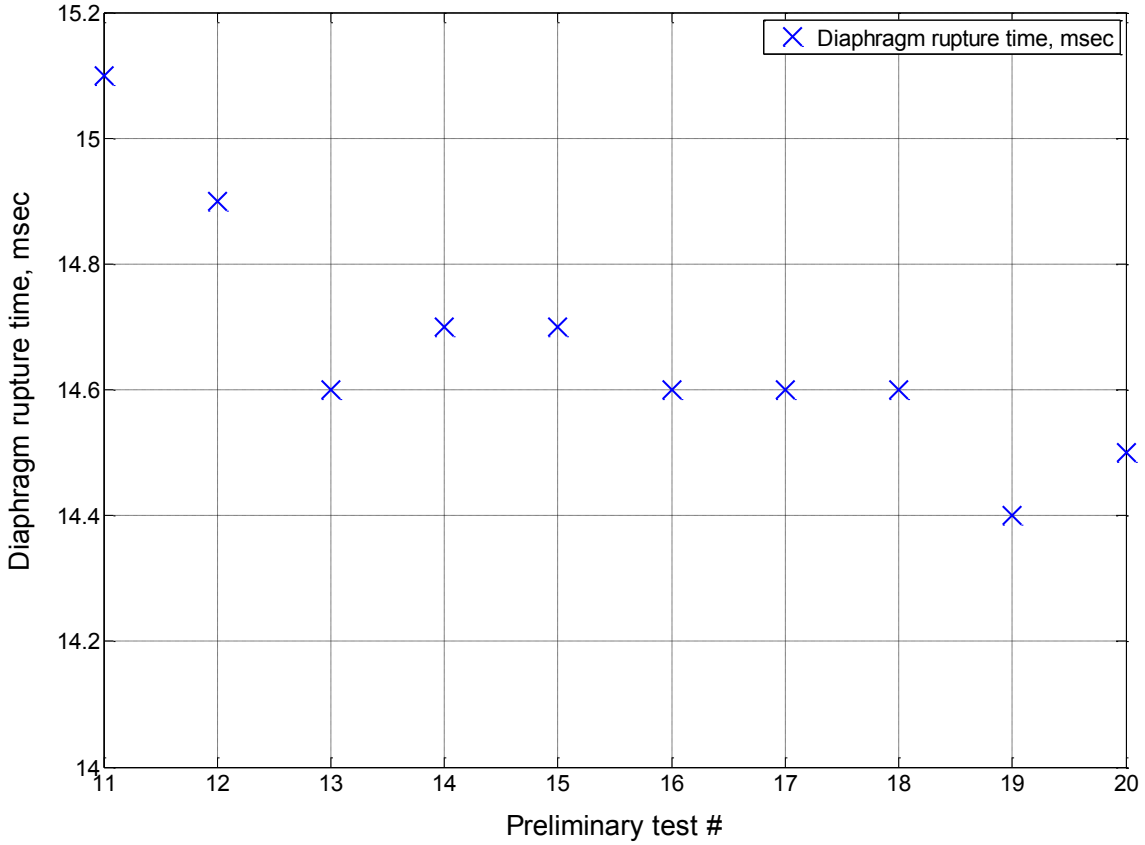

Figure 3.8 Diaphragm rupture time variation after ignition in the pre-chamber

The consistency of the rupture pressure in the pre-chamber indicates the consistency of the scoring process as well as the consistent burning rate of the ethylene-air mixture in the pre-chamber in Figure 3.9. This reinforces the earlier assumption of the torch jet having identical properties ejecting through the nozzle. The diaphragm rupture pressure varies from 52.9 to 56.3 psig with a mean rupture pressure of 54.1 psig and a standard deviation 1.0 psi.

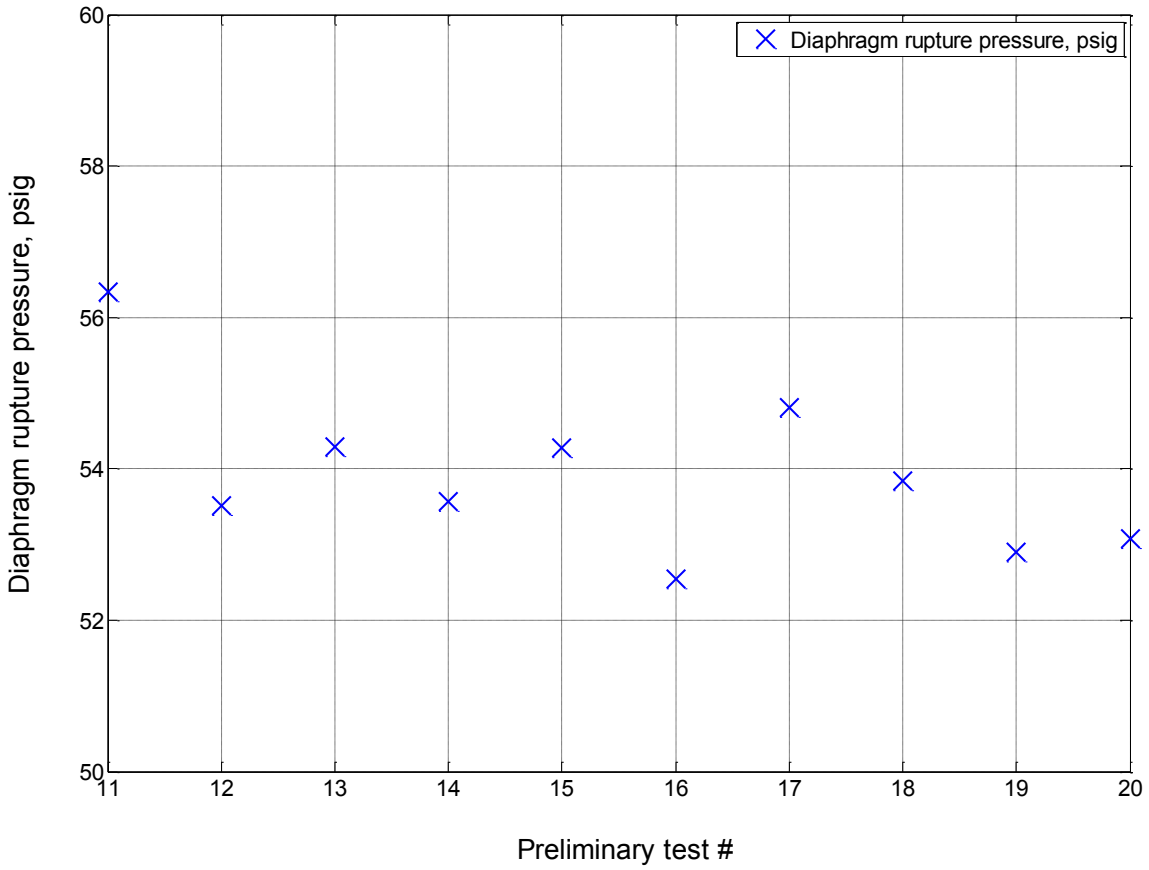

Figure 3.9 Diaphragm rupture pressure variation in the pre-chamber

The maximum pressure reached in the pre-chamber is dependent on the burning rate of the ethylene-air mixture, the pressure built in the pre-chamber while the mass outflow through the nozzle and the heat loss to the pre-chamber. Figure 3.11 shows that all these effects varied in a similar way in all of these preliminary tests. The maximum pressure in these tests varied from 91.0 to 93.7 psig. The average maximum pressure in the pre-chamber was 92.3 psig with a standard deviation of 1.0 psi for these tests.

The consistency of the diaphragm scoring method is illustrated with Figure 3.10. the figure indicate the diaphragm rupture time after the trigger signal on the x-axis and the rupture pressure from the measured pressure inside the pre-chamber. The same preliminary test used to plot both Figures 3.8 and 3.9 were used to construct this figure. The red circle indicate 7 tests where, the calculated diaphragm rupture time and the

measured diaphragm rupture pressure (at the calculated diaphragm rupture time) are clustered together. The 2 out of the 3 outlying data points were also found to be within the acceptable variations observed for both the diaphragm rupture time and pressure in the pre-chamber at 95% confidence limit. The diaphragm rupture was calculated to be approximately 14.7 ms with a standard deviation of 0.2 ms. The diaphragm rupture pressure varied between 52.5 to 55.0 psig for 9 out of the 10 preliminary tests, indicating the consistency and the repeatability of the combustion process in the pre-chamber and the diaphragm scoring method.

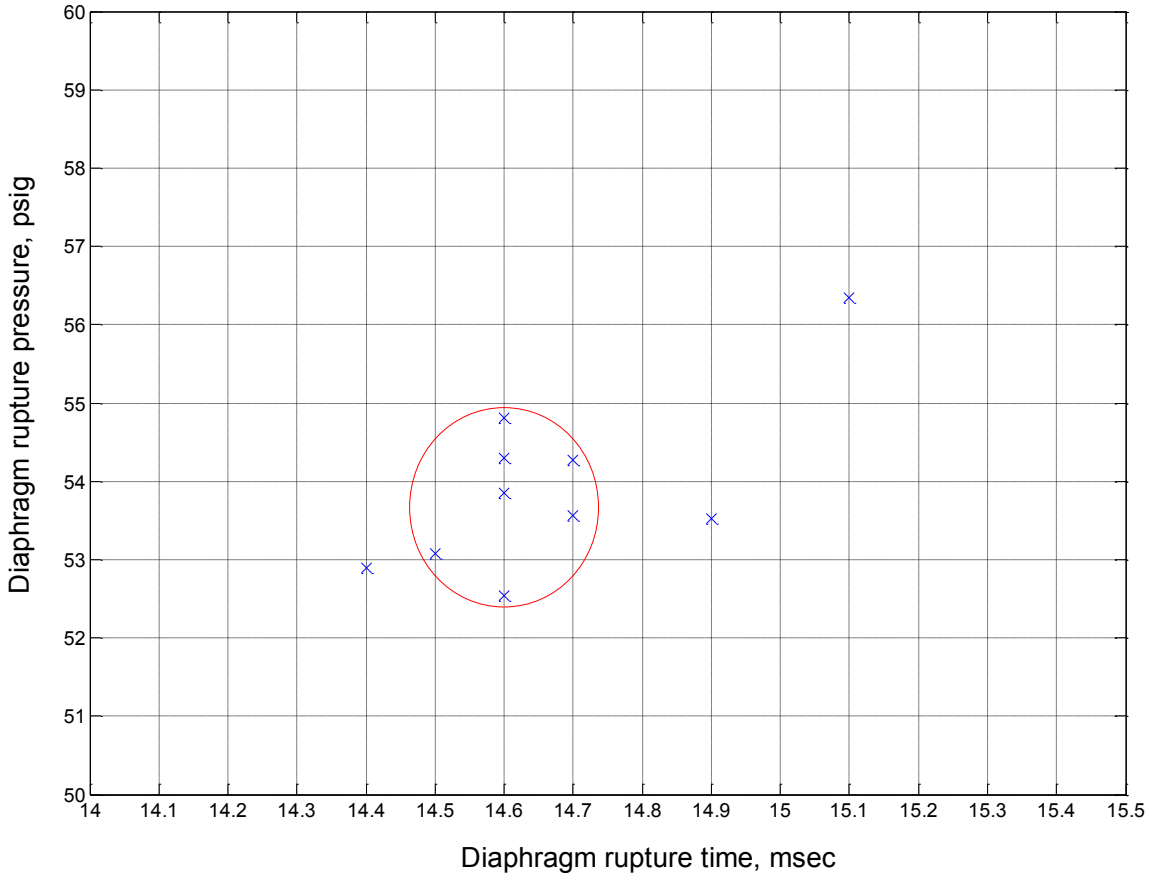

Figure 3.10 Diaphragm rupture pressure variation with diaphragm rupture time from trigger signal

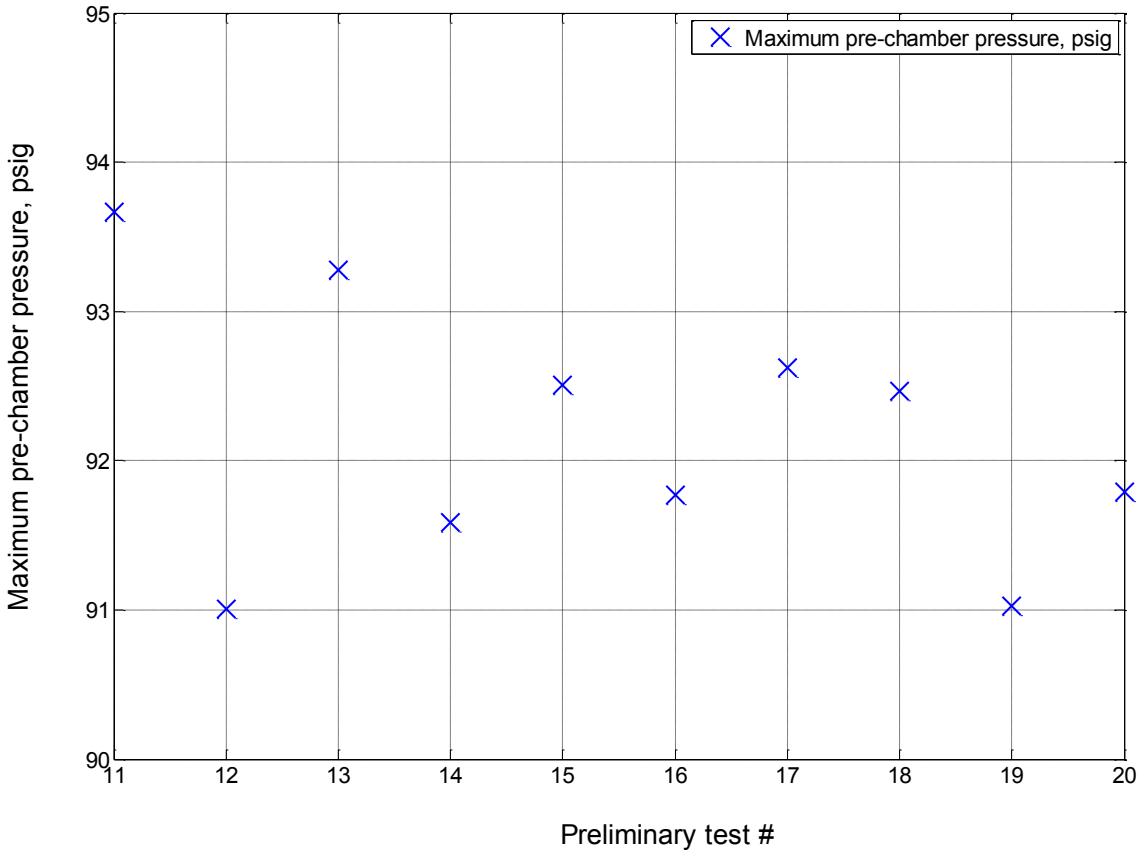

Figure 3.11 Maximum pressure variation in the pre-chamber

The results from the preliminary test in Figure 3.5 through to Figure 3.11, indicate the consistency of the torch jet conditions provided that the equivalence ratio (maintained at 1.1) and the pre-chamber initial pressure and initial temperature are maintained (atmospheric pressure and room temperature respectively). These preliminary experiments indicated the reliability and consistency of the pre-chamber torch jet and reliability of the results from the main study.

3.5. Detection of Ignition in the Main Chamber using Pressure Histories

The ignition of the fuel-air mixture in the main chamber with the torch jet was investigated as a preliminary test with test numbers 021 and 023. Ethylene was used as the fuel in the pre-chamber in both experiments. The initial pressure and the initial

temperature were set at atmospheric pressure and room temperature in both chambers in the two tests. For preliminary test 021, the equivalence ratio of ethylene-air mixture prepared was 1.1 and 1.0 in the pre-chamber and the main chamber respectively. While for preliminary test 023 the main chamber was filled with atmospheric air but the pre-chamber was fueled with an identical mixture prepared for the pre-chamber in preliminary test 021. The summary of the test conditions and the rupture conditions are given in Table 3.2.

Table 3.2 Test conditions and pre-chamber rupture conditions

Preliminary Test #	Pre-chamber equivalence ratio, ϕ	Main chamber equivalence ratio, ϕ	Diaphragm rupture time (ms)	Diaphragm rupture pressure (psig)	Pre-chamber max. pressure (psig)
021	1.1	1.0	15.6	52.7	88.6
023	1.1	0	15.8	53.5	88.8

The objective of these preliminary experiment were to investigate the difference between the pressure histories from an ignition test and a no ignition test from PT-1, PT-2, and PT-3 pressure transducers. Figure 3.12 through 3.15 clearly illustrate the change in the pressure histories of the pressure transducers in the main chamber for preliminary tests 021 and 023. The ethylene-air mixture in the main chamber ignited in preliminary test 021 but there was no ignition in preliminary test 023. The temporal pressure variation at these locations can be used to detect ignition in the main chamber combustible mixture due the rise in pressure with limitations pertaining to spatial locations. Example of such a spatial limitation is when the ignition location in the mixture is between two pressure transducers, and both indicate a delay in recording the pressure rise due to the finite time taken for the pressure disturbance to reach the pressure transducer location from the ignition source location.

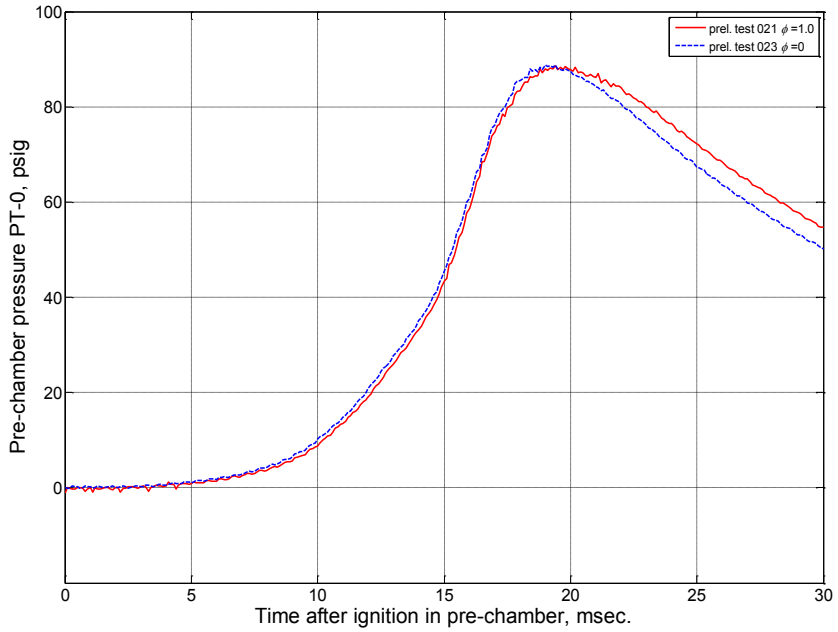

Figure 3.12 Ignition and no ignition in the main chamber comparison - pre-chamber pressure trace from PT-0

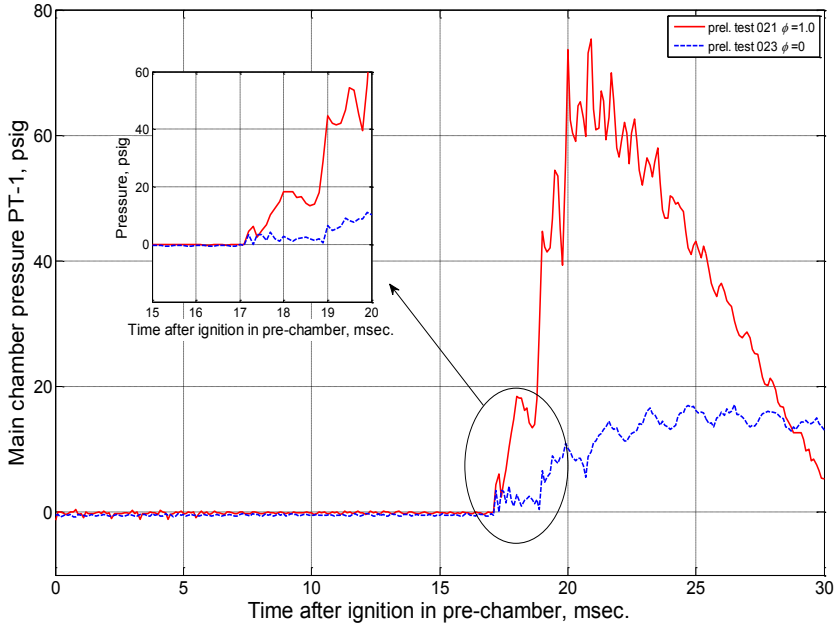

Figure 3.13 Ignition and no ignition in the main chamber comparison - main chamber pressure trace from PT-1

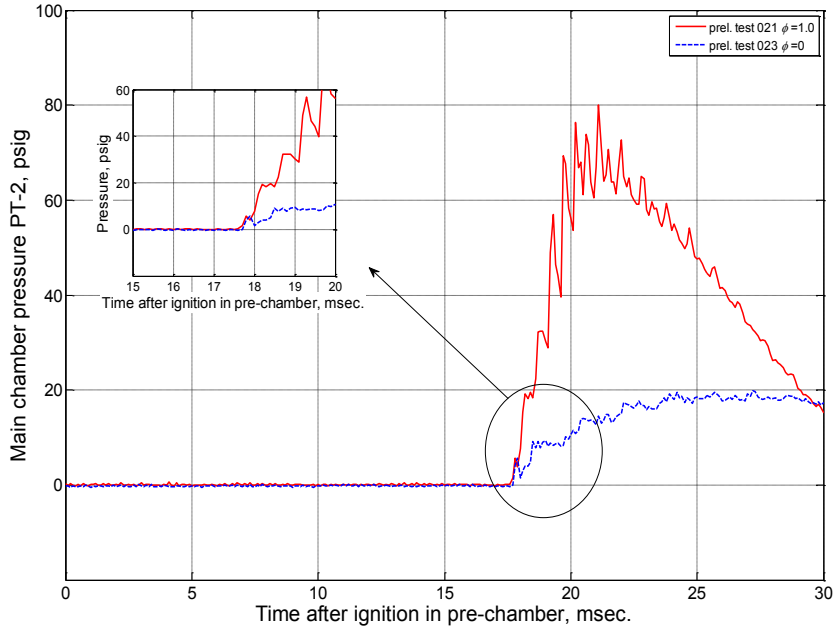

Figure 3.14 Ignition and no ignition in the main chamber comparison - main chamber pressure trace from PT-2

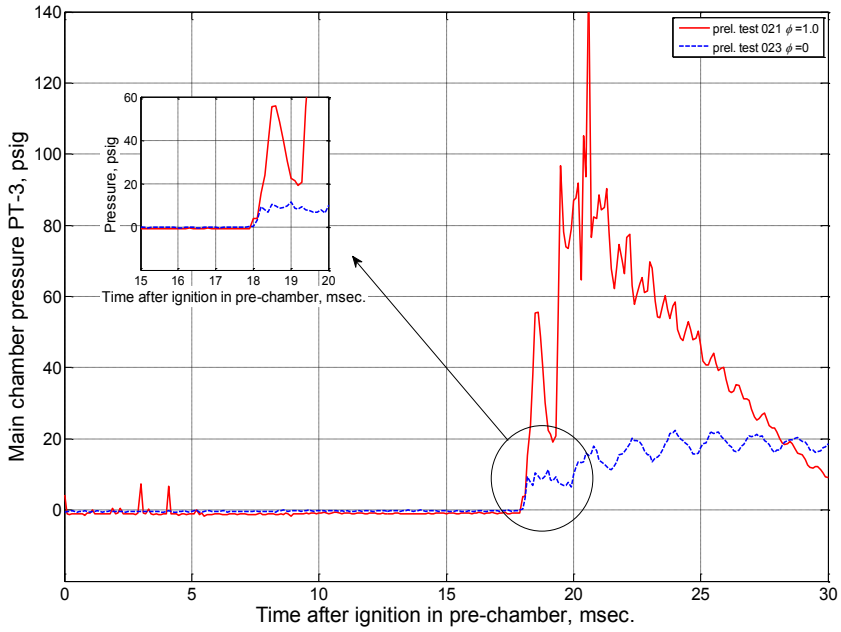

Figure 3.15 Ignition and no ignition in the main chamber comparison - main chamber pressure trace from PT-3

3.6. Detection of Ignition in the Main Chamber using Image Processing

High-speed video images were captured using a Phantom® v9.0 monochrome camera equipped with a CMOS (Complementary Metal Oxide Semiconductor) sensor. The captured images were used to determine ignition in the main chamber using a computer based image processing method. As described earlier in chapter 2, the Phantom v9.0 camera spectral response is 400-1,000 nm, which incorporates both the visible spectrum as well as near-infrared spectrum from 700-1,000 nm of the electro-magnetic spectrum (Refer Appendix D). When the sensor is exposed to the object of interest, light or photons from the object fall on the pixels. The amount of photons that create useful charge is called the quantum efficiency (QE) of the sensor. This QE is dependent upon the wavelength of the electro-magnetic waves incident on the sensor. The photons of light absorbed by the sensor surface are converted into electric charge using the photoelectric effect. The charge stored on individual capacitor per pixel was consequently converted into a voltage. The pixel capacitors on the sensor are brought to a reference level, using the "black referencing" values obtained when setting up the camera. Then the pixels are kept exposed to the incident photons for the preset exposure time. At the end of the exposure time the electronic shutter cuts off the photons incident on the sensor which causes the accumulated voltage to pass though the sensor output. The cycle time of the electronic shutter operation is based on the frame rate. The sensor pixels are returned to the reference state ready for the next cycle.

Different types of combustion related research use different spectral ranges depending on the gas constituents of interest and the temperature range of the gas mixture [35]. Walton et al investigated ignition properties of syngas using a rapid compression facility to observed visible light emission and pressure to detect ignition [36]. A few preliminary experiments were conducted with a Hoya 52 mm RM-90 infrared transmitting filter (Specifications provided under Appendix G) which eliminates the full-spectrum of visible light where the luminous intensity observed was largely reduced due to the transmittance of the filter being above 80% in the 1,000-2,700 nm spectrum. The transmittance in the spectral response of the filter varied from 0-80% in the 750-1,000 nm

range. This did not give a clear insight into the spectral range of the luminosity observed in the experiments except that the amount of luminosity was low with the filter in-place all testing was conducted without the use of the filter.

The image processing method used to identify ignition was based on the algorithm illustrated in Figure 3.16. The high-speed video images from the camera were analyzed using the code developed using MATLAB® to eliminate the human error in identifying ignition.

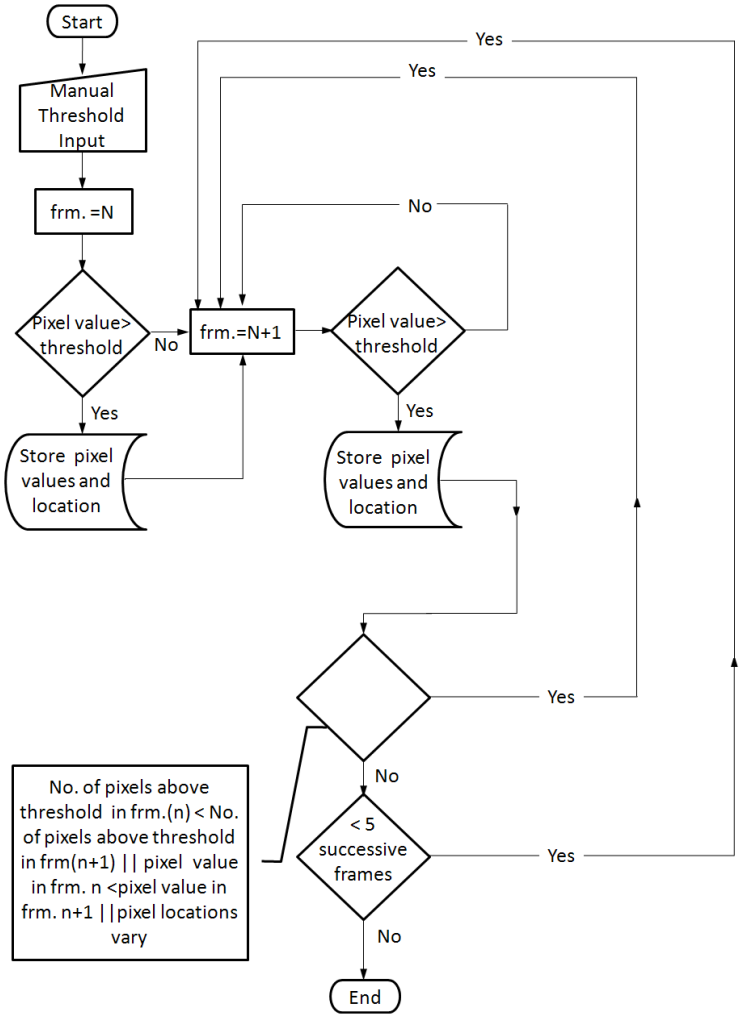

Figure 3.16 Image processing algorithm used to identify ignition in the main chamber

Figure 3.17 illustrates the injection of the combustion torch jet into the main chamber and subsequent ignition and the flame propagation in the chamber. The top strip of Figure 3.17 shows the image processed edge of the luminous area above a critical threshold arbitrarily selected by the user. The color-code illustrated from red-blue respectively correspond to frames # 173-179.

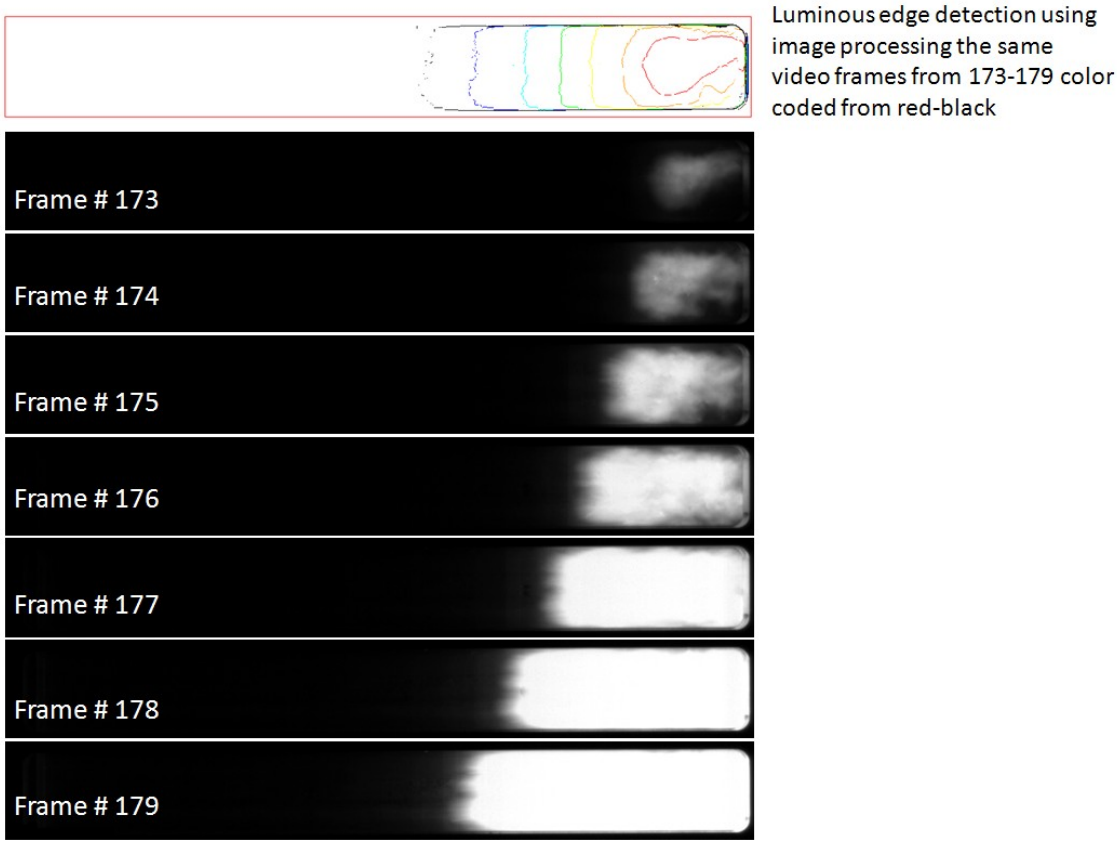

Figure 3.17 Ignition and subsequent flame propagation using image processing on the luminous region with threshold value equal to 10% of the full scale signal

The threshold value equal to 10% of the full scale signal was arbitrarily selected where the full scale signal is the 8-bit grayscale map from the high-speed video. The signal in 8-bit grayscale ranging from 0 for “black” to 255 for “white”. An alternative threshold equal to 80% of the full-scale signal was used to determine ignition in the main chamber although the variation was not high for ethylene mixtures, methane mixtures

tended to show a larger deviation due to the time required for the luminous intensity to build. This latter threshold level was used by Wójcik and Kotyra [37], but the authors claim that the threshold was chosen arbitrarily for their study.

3.7. Diaphragm Debris and Rupture Patterns

During the preliminary test two potential problems were foreseen. These problems are the rupturing of the diaphragm and the inflowing combustion torch jet blowing aluminum diaphragm debris into the main chamber. This phenomenon was visible and recorded in the high-speed video images captured. The problem was that in some instances the ignition in the main chamber occurred in a location in the vicinity of the trail left by the path of these particles. In the preliminary experiments, this occurred approximately in 15% of the experiments, deeming it a variable that eliminated by conducting a sufficient amount of experiments in which this phenomenon did not occur.

The other drawback foreseen with the use of the pre-chamber diaphragm was depending on the depth of the score made on the diaphragm the diaphragm wouldn't rupture into four symmetric petals. This leads to variations in the flow field and properties of the torch jet affecting the ignition in the main chamber. This was observed and recorded to in less than 10% in the preliminary experiments. To check if this was a random occurrence, or related to the scoring method used, or the pressure rise in the main chamber, the diaphragm was marked as indicated in Figure 3.18 prior to being sandwiched between the nozzle insert and the nozzle plate. The numbers referring to the score path made on the diaphragm starting from the numbered side. The diaphragms petal configurations were given naming conventions to identify the rupture patterns as indicated in the bottom row of Figure 3.18.

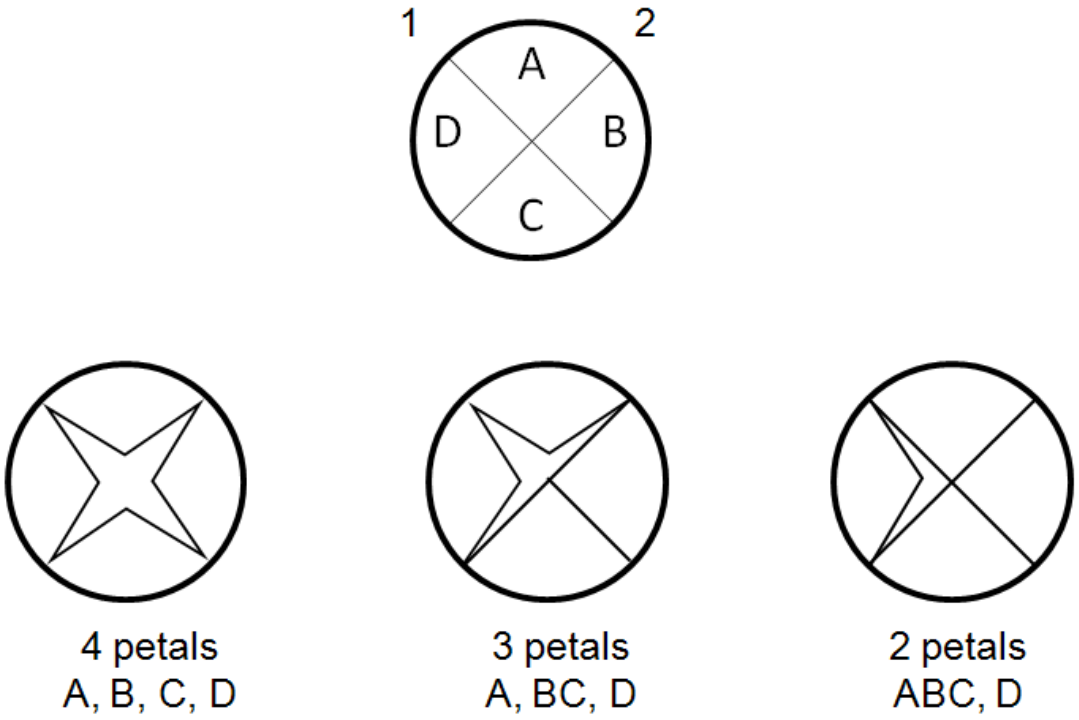

Figure 3.18 Diaphragm rupture patterns: (top) Diaphragm marking, (bottom) Rupture patterns

3.8. Mixing Effects on the Experiment

The effects of mixing of the fuel and air supplied to each of the chambers in the experiment was looked into with some preliminary experiments. Three preliminary test were analyzed here with preliminary test 025 allowed only 5 minutes of mixing time for the main chamber fuel-air mixture and the other two experiments (preliminary tests 026 and 027) left in the chambers to mix overnight for over 17 hours. The pressure transducer data from PT-0 in the pre-chamber, PT-1 to PT-3 in the main chamber are illustrated below in Figure 3.19 to Figure 3.22. There was a slight increase in the pressure histories from the pre-chamber for overnight tests 026 and 027 when compared with the preliminary test 025. These variations were well within the pre-chamber pressure variation for the experiment.

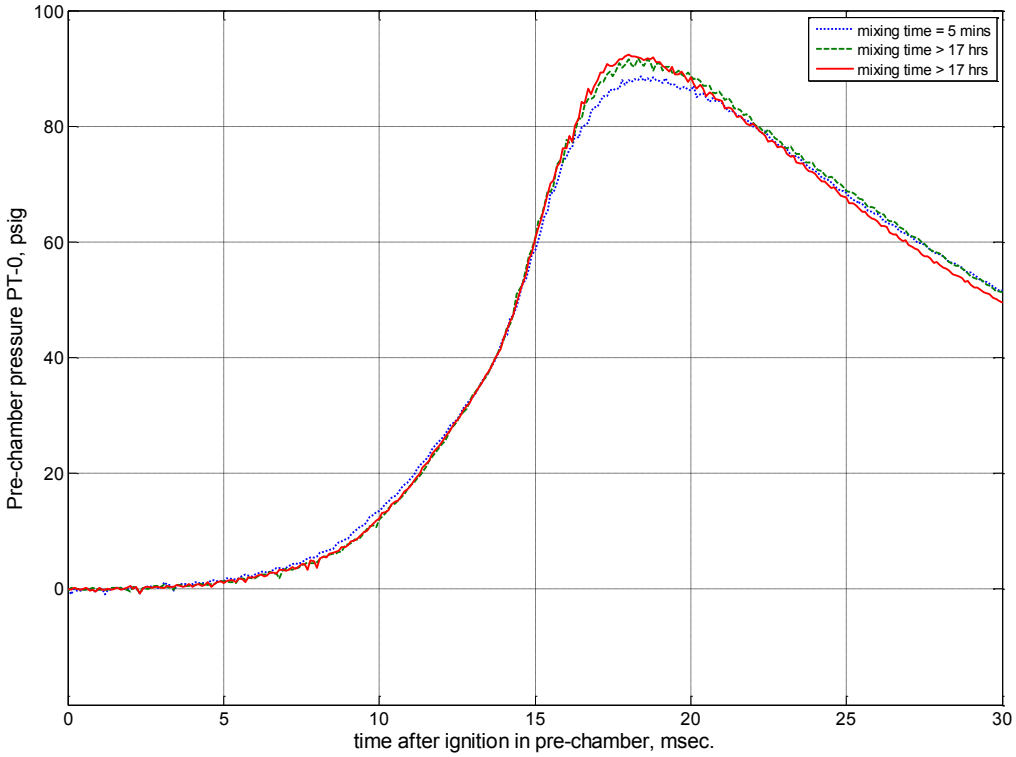

Figure 3.19 Mixing time effects on ignition in the pre-chamber from pressure transducer PT-0

The main chamber pressure histories again indicated slight pressure differences for overnight tests compared to the 5 minute mixture test. But the important feature to be noticed in Figure 3.20 to Figure 3.22 was the time instance of combustion pressure spike in all three pressure transducer data are similar in both overnight and 5 minute mixture tests. The difference in the pressure distributions might be attributed to the fuel-air mixture difference in the main chamber for the two types of tests. Influence of pre-chamber variations were not considered since the pre-chamber conditions are identical in the two types of tests. The overnight tests having had enough time to form a better uniform mixture along the channel compared to the 5 minute tests. High-speed video images for preliminary tests 025 and 026 are shown in Figure 3.23.

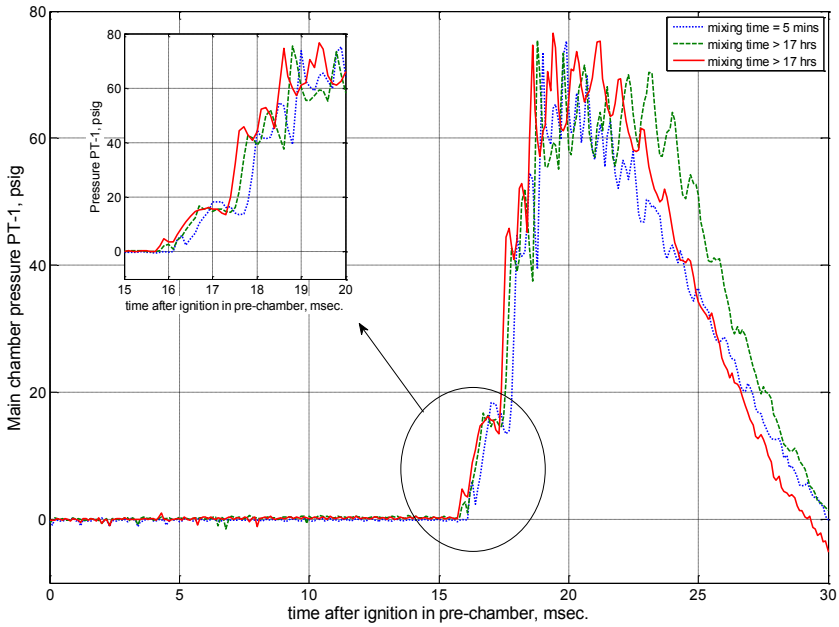

Figure 3.20 Mixing time effects on ignition in main chamber from pressure transducer PT-1

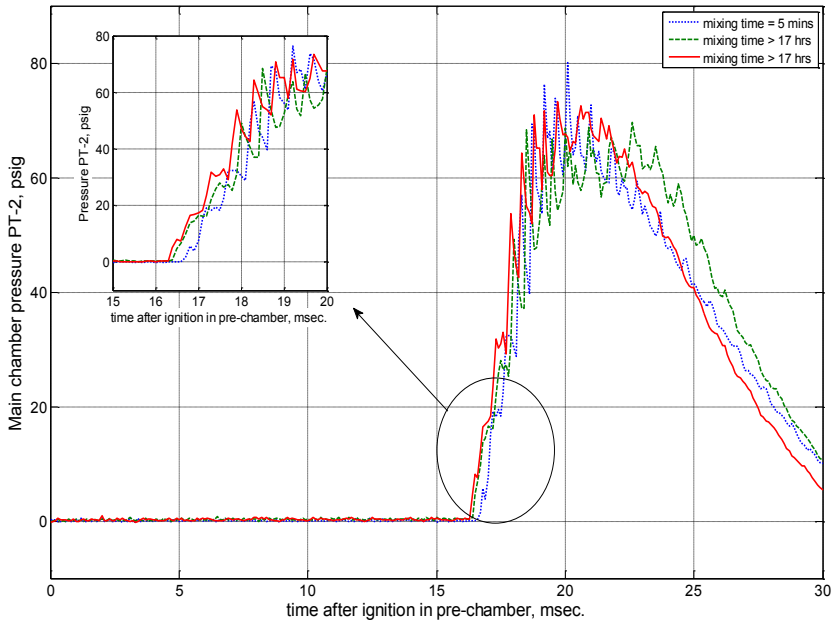

Figure 3.21 Mixing time effects on ignition in main chamber from pressure transducer PT-2

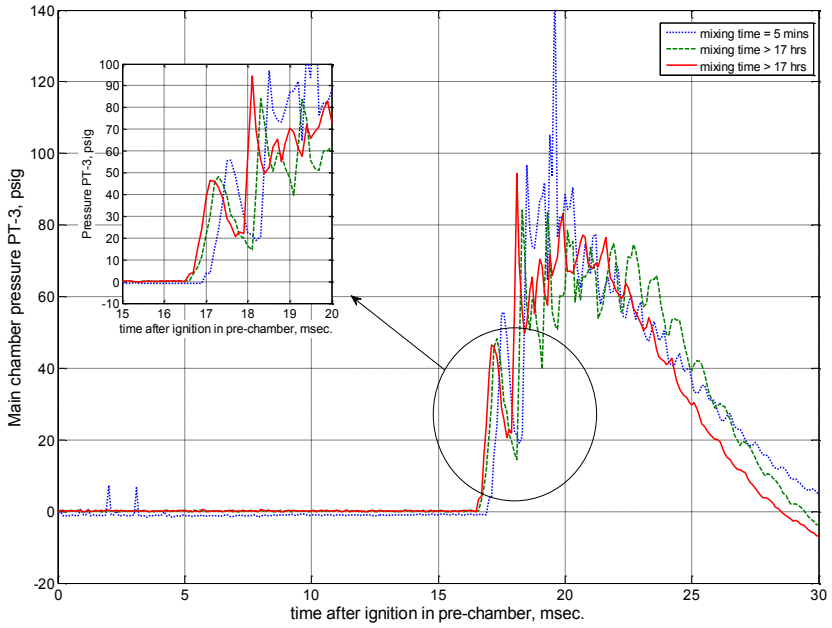

Figure 3.22 Mixing time effects on ignition in main chamber from pressure transducer PT-3

These images were arranged from the diaphragm rupture in the pre-chamber indicated by the horizontal line marked in red. The torch jet injecting into the main chamber were similar as per the high-speed images, confirming the repeatability and reliability of the pre-chamber torch jet. In both tests the ignition in the main chamber is a finite distance from the right edge of the viewing window after a finite resident time. The combustion flame quickly penetrated into the main chamber. There were no major differences between the high-speed video images for tests 025 and 026 in the ignition and flame propagation in the main chamber. However, the change in the quality of the images in the two tests was due to a camera malfunction that left the left-half of the camera distorting the image by displaying black pixels randomly under extremely bright luminous levels. Therefore, it was decided 5 minutes provided sufficient mixing time for the experiments.

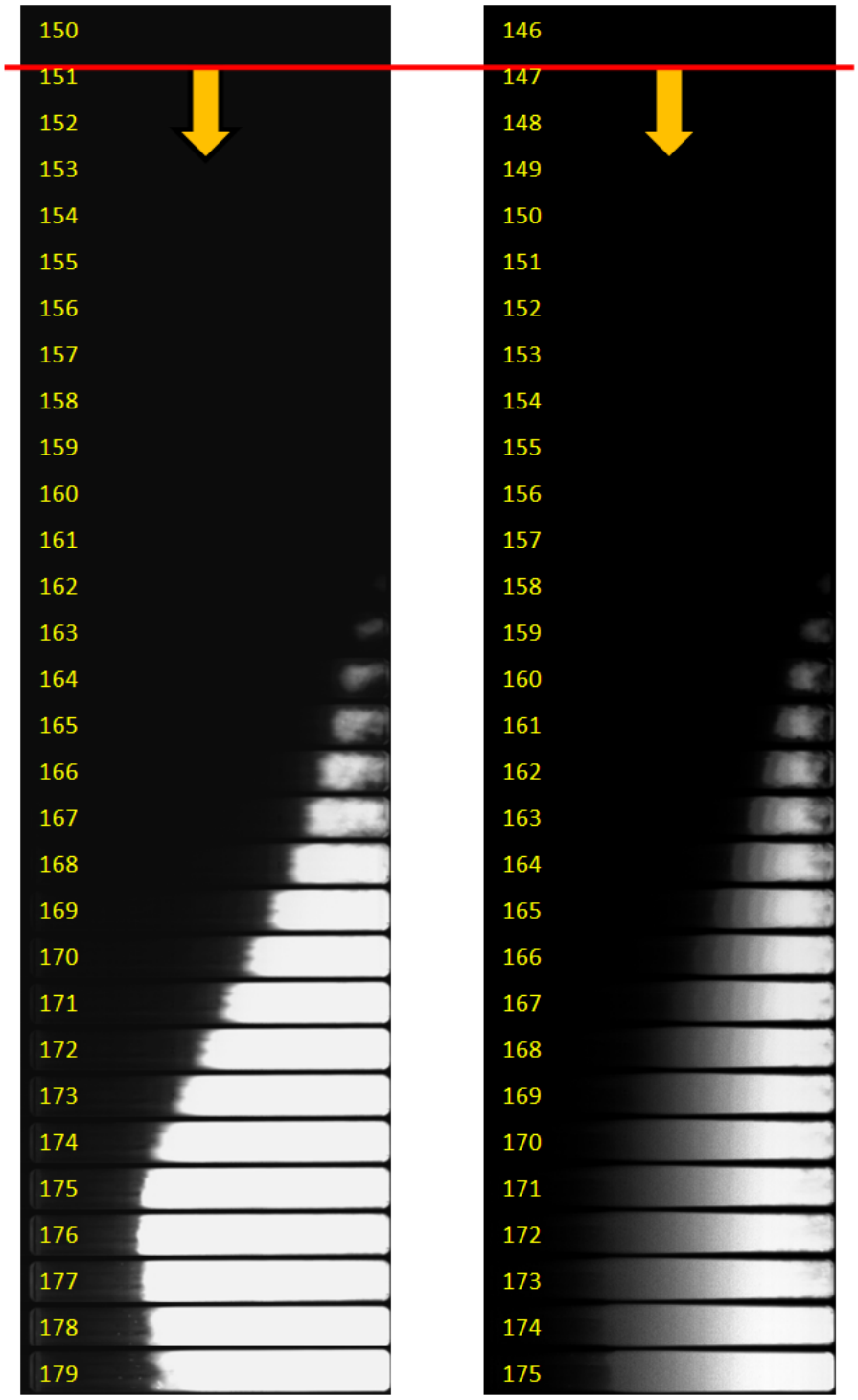

Figure 3.23 Comparison between high-speed images obtained from preliminary Test numbers 025 and 026

CHAPTER 4. EXPERIMENTAL PROCEDURE, DEFINITIONS OF EXPERIMENTAL PARAMETERS, AND RELATED COMBUSTION KINETICS

This chapter explains the experimental procedure and definitions used in the processing of information obtained from the experiments used in the study. In addition key combustion chemical kinetics of methane, ethylene, and propane fuels under experimental conditions used in the study are also discussed.

4.1. Experimental Procedure

Every experiment was prepared using the method described in this section. The pre-chamber and the main chamber were prepared by purging both chambers with pressurized air. After the purging process the pre-chamber was sealed using the pressure transducer insert and nozzle insert assembly with the aluminum diaphragm. The main chamber was sealed using the latex diaphragm assembly and then covered with the main chamber fueling plate. The pre-chamber was the first to be fueled with the required amount of fuel for the desired equivalence ratio using the fueling system described in Section 2.5. The partial pressure method described in Section 3.1 was used in preparing the fuel-air mixture in the pre-chamber. After the pre-chamber was fueled, the fueling system was purged with pressurized air for 3 minutes. Then the main chamber was fueled using the same procedure used to fuel the pre-chamber. The main chamber fuel air-mixture was left to mix for 5 minutes before the ignition system was triggered in the pre-chamber to start the experiment. The main chamber fueling plate was removed from the main chamber channel inlet face and the main chamber was positioned flush against the pre-chamber nozzle face before the ignition system was triggered. The pre-chamber nozzle exit was aligned with the main chamber channel with the use of the graduated tape in the pre-chamber and the horizontal laser line generator mounted on the high speed-

camera. The procedure for on aligning the laser alignment system was described in Section 2.4.1.

4.2. Ignition

Ignition has been defined in various ways by different researchers. Van Dolah [10] describes ignition as the initiation of flame which is identified by high temperature, high pressure rises and release of "light" and radiation. The "light" as explained by this research was the self illumination of the combustible mixture as the combustion products convert into reactants releasing radiation in the visible spectrum of the electromagnetic spectrum. This radiation of visible light was observed by some past jet ignition research conducted by Wolfhard [9], Vanpée [11], Bruszak [12], Fink [13], and Cato [14].

Ignition is defined by Lifshitz [38] as the bulk of the energy released in an exothermal reaction, which in turn rapidly increases the pressure and temperature of the combustion products. Lifshitz [38] also states different experimental properties that can be used to identify ignition such as pressure, density gradients, heat flux, emission of specific species, or the total emission from the hot combustion gases, optical measurements such as ultraviolet, infrared, and laser absorption, or any combination of these properties. Although these studies concentrated more on shock ignition of fuel-air mixtures, the same experimental properties can be used in combustion torch jet ignition studies.

This study used the radiation emission in the range from 400-1,000 nm of the electromagnetic spectrum which the high-speed camera sensor was able to detect in order to identify ignition in the main chamber. The evolution of the luminous region was used to identify the self propagating flame that traverse the main chamber both downstream as well as upstream. In addition to this, optical method, the spatial pressure measurements from the pressure transducers in the main chamber were used to validate the ignition and subsequently the ignition delay time.

4.3. Ignition Delay Time

Ignition delay time is defined by Lifshitz [38] as the induction time where only a fraction of the energy of an exothermal reaction is released before the majority of the energy is released suddenly within a small time duration. The ignition event is preceded by the ignition time delay where the pressure and temperature of the combustible mixture in which the chain initiation reactions set the other reactions in motion. This leads to the chain-branching reactions and a near adiabatic temperature rise and exponential pressure increment during the energy released during the exothermal reaction. The ignition delay time is said to be dependent upon the initial pressure, initial temperature, initial mixture fraction of the combustible mixture, and the reaction mechanisms which govern the ignition process.

To define ignition delay two time events have to be identified that is common from one experiment to the next experiment. Due to this constraint the definition of ignition delay time varies among researchers. Some of the variations are due to the measuring equipment and methods and some on the physical variations of the experimental facility. In most shock ignition experiments the ignition time is measured from the time event where the shock wave hits the closed end of the driven section until the reflected shock from the same end ignites the combustible mixture. Pressure transducers mounted on the closed wall or close to the end wall are used to measure the event of the shock arrival [39, 40]. The ignition event was determined using photomultipliers [39, 40] in some of the studies while in others the emission of specific species like OH, CH, and C_2 radicals were used [41-43]. The photomultiplier used by Baker and Skinner [39] had a spectral response to wavelengths ranging from 185-650 nm. Brown and Thomas [43] used a photomultiplier to monitor CH emission at a wavelength of 431.5 nm at the end wall of the driven section of the shock tube. Myers and Bartle [47] used an optical system to observe the radiation from different species in the reaction zone. The electromagnetic spectrum ranging from 250-800 nm was observed in these studies which were to find ignition delays in oxidation of propane. The observed species and radicals included CO, CO_2, OH, CN, CH, C_2, and H_2O.

The radiation emitted from combustion products including the species and radicals from oxidation of methane, ethylene, and propane in shock tube experiments emit in the wave ranges from 185-800 nm. Although not discussed in the shock tube studies, soot radiation is another important candidate which emits in the "visible" and infrared wavelengths [48-49]. The high-speed camera spectral response covers the entire visible and the near-infrared spectra ranging from 400-1,000 nm as illustrated in Appendix D. The fact that species or radicals generated with ignition of these fuels with hot combustion torch jets also radiate in the visible spectrum was evident from the discussion in Section 3.6.

For the current study the diaphragm rupture time described in Section 3.3 was used as the event to begin measuring the ignition delay time. The optical observation from the high-speed camera was primarily used to determine ignition event in the main chamber as described in Section 3.6. The pressure histories from the main chamber were used to validate the image processing ignition delay times making corrections to the spatial variations due to the propagation of the pressure disturbance in relation to the pressure transducer location in the main chamber.

4.4. Kinetics of Methane, Ethylene, and Propane

The combustion reaction mechanisms explained below are extracted from references [42, 50, 51] related to the reaction temperatures in the range assumed to be present in hot combustion torch jet experiments. The kinetics for methane and propane chain-initiation reactions is similar to each other which yield in producing methyl radicals.

$$CH_4 + M \rightarrow CH_3 + H + M \qquad \text{Eq. 4.1}$$

$$C_3H_8 + M \rightarrow CH_3 + C_2H_5 + M \qquad \text{Eq. 4.2}$$

Ethylene, on the other hand, initiates with the possibility of the three reactions listed below.

$$C_2H_4 + M \rightarrow C_2H_2 + H_2 + M \quad \text{Eq. 4.3}$$
$$C_2H_4 + M \rightarrow C_2H_3 + H + M \quad \text{Eq. 4.4}$$
$$C_2H_4 + C_2H_4 \rightarrow C_2H_3 + C_2H_5 \quad \text{Eq. 4.5}$$

The reaction rate of Equation 4.5 is stated to be negligible compared to the reaction rates as the other ethylene initiation reactions unless in an ethylene rich environment.

The H-atom abstraction of methane reactions takes effect next with the following list of reactions.

$$CH_4 + H \rightarrow CH_3 + H_2 \quad \text{Eq. 4.6}$$
$$CH_4 + OH \rightarrow CH_3 + H_2O \quad \text{Eq. 4.7}$$
$$CH_4 + O \rightarrow CH_3 + OH \quad \text{Eq. 4.8}$$
$$CH_4 + HO_2 \rightarrow CH_3 + H_2O_2 \quad \text{Eq. 4.9}$$

For propane the H-atom abstraction reactions are listed below:

$$C_3H_8 + M \rightarrow iC_3H_7 + H + M \quad \text{Eq. 4.10}$$
$$C_3H_8 + M \rightarrow nC_3H_7 + H + M \quad \text{Eq. 4.11}$$

Ethylene reacts under H-atom abstraction and formation of activated complexes.

$$C_2H_4 + H \rightarrow C_2H_3 + H_2 \quad \text{Eq. 4.12}$$
$$C_2H_4 + OH \rightarrow C_2H_3 + H_2O \quad \text{Eq. 4.13}$$
$$C_2H_4 + O \rightarrow CH_3 + HCO \quad \text{Eq. 4.14}$$
$$C_2H_4 + O \rightarrow CH_2O + CH_2 \quad \text{Eq. 4.15}$$
$$C_2H_4 + OH \rightarrow CH_3 + CH_2O \quad \text{Eq. 4.16}$$

The CH_3 and C_2H_3 radicals created in reactions represented by Equation 4.12-4.14 and 4.16 recombining will create higher carbon to hydrogen ratio species which promote soot

formation under ethylene rich environments. These reactions also have a negative effect as they serve as chain terminating reactions.

$$CH_3 + C_2H_3 \rightarrow C_3H_6 \quad \text{Eq. 4.17}$$

$$C_2H_3 + C_2H_3 \rightarrow C_4H_6 \quad \text{Eq. 4.18}$$

The methane reactions at temperatures of 1,100 K (approximately the temperature estimated to be around the mixing zone of the torch jet [30]) follow in the methyl reactions listed below:

$$CH_3 + O_2 \rightarrow CH_3O + O \quad \text{Eq. 4.19}$$

$$CH_3 + CH_3 \rightarrow C_2H_5 + H \quad \text{Eq. 4.20}$$

$$CH_3 + CH_3 \rightarrow C_2H_4 + H_2 \quad \text{Eq. 4.21}$$

$$CH_3 + CH_3 \rightarrow C_2H_6 \quad \text{Eq. 4.22}$$

Under normal combustion temperatures the methyl radicals recombine to make ethane and this reaction equation dominates over Equations 4.20 and 4.21. This recombination makes methane oxidation different from ethylene and propane oxidation and the affinity for recombination reactions increases with richer mixtures of methane. This also indicates that methane oxidation can be separated into two distinct mechanism paths. The first, recombining methyl radicals and then subsequent oxidation of these recombined species in reaction were stated in Equations 4.20-4.22. The second path, where methyl radical oxidation into methoxy radicals and then to formaldehydes, as indicated by the reaction from Equations 4.23-4.28.

These methyl radicals react in a variety of reactions.

$$CH_3 + O \rightarrow CH_2O + H \quad \text{Eq. 4.23}$$
$$CH_3 + OH \rightarrow CH_2O + H_2 \quad \text{Eq. 4.24}$$
$$CH_3 + OH \rightarrow CH_3O + H \quad \text{Eq. 4.25}$$
$$CH_3 + CH_2O \rightarrow CH_4 + HCO \quad \text{Eq. 4.26}$$
$$CH_3 + HCO \rightarrow CH_4 + CO \quad \text{Eq. 4.27}$$
$$CH_3 + HO_2 \rightarrow CH_3O + OH \quad \text{Eq. 4.28}$$

Finally, these CH_3O and CH_2O created were oxidized into CO and then these CO oxidizes into CO_2 reacting with OH, H, and HO_2.

The created iC_3H_7 and nC_3H_7 propyl radicals from reaction Equations 4.10 and 4.11 decay into species with smaller numbers of carbon atoms as listed below.

$$iC_3H_7 + M \rightarrow C_2H_4 + CH_3 \quad \text{Eq. 4.29}$$
$$nC_3H_7 + M \rightarrow C_2H_4 + CH_3 \quad \text{Eq. 4.30}$$
$$iC_3H_7 + M \rightarrow C_3H_6 + H \quad \text{Eq. 4.31}$$
$$nC_3H_7 + M \rightarrow C_3H_6 + H \quad \text{Eq. 4.32}$$

From these 4 propyl decay reactions Equation 4.31 and 4.32 are favored since the abstracted H-atoms from these reactions consume the propane in the following reactions:

$$C_3H_8 + H \rightarrow iC_3H_7 + H_2 \quad \text{Eq. 4.33}$$
$$C_3H_8 + H \rightarrow nC_3H_7 + H_2 \quad \text{Eq. 4.34}$$

In addition to the third body effects breaking the propane molecule into propyl radicals, propane oxidation will also lead to the same propyl radicals.

$$C_3H_8 + O \rightarrow iC_3H_7 + OH \quad \text{Eq. 4.35}$$
$$C_3H_8 + O \rightarrow nC_3H_7 + OH \quad \text{Eq. 4.36}$$
$$C_3H_8 + OH \rightarrow iC_3H_7 + H_2O \quad \text{Eq. 4.37}$$
$$C_3H_8 + OH \rightarrow nC_3H_7 + H_2O \quad \text{Eq. 4.38}$$
$$C_3H_8 + HO_2 \rightarrow iC_3H_7 + H_2O_2 \quad \text{Eq. 4.39}$$
$$C_3H_8 + HO_2 \rightarrow nC_3H_7 + H_2O_2 \quad \text{Eq. 4.40}$$

Westbrook and Dryer [50] state that Equations 4.37 and 4.38 involving OH radicals are more important for lean and stoichiometric mixtures, and equations involving H radicals are important in propane rich mixtures.

At temperatures assumed to be existent in hot combustion torch jet ignitions at around 1,100 K the reactions involving radical oxidation using O_2 is given priority.

$$iC_3H_7 + O_2 \rightarrow C_3H_6 + HO_2 \quad \text{Eq. 4.41}$$
$$nC_3H_7 + O_2 \rightarrow C_3H_6 + HO_2 \quad \text{Eq. 4.42}$$

The created propene is considered to react with third body or decay into either methyl radical or H-atom abstraction. The ethene molecules created in the above two reaction equations decay to lower carbon species. These reactions were discussed by Westbrook and Dryer [50] for shock tube problems since the activation energy for these reactions is high.

$$C_3H_6 + M \rightarrow C_2H_3 + CH_3 + M \quad \text{Eq. 4.43}$$
$$C_3H_6 + M \rightarrow C_3H_5 + H + M \quad \text{Eq. 4.44}$$

Another reaction mechanism involves oxidation or H-atom abstraction of the propene molecule [50] which is also referred to by Turns [51].

$$C_3H_6 + O \rightarrow C_2H_5 + HCO \quad \text{Eq. 4.45}$$
$$C_3H_6 + OH \rightarrow C_3H_5 + H_2O \quad \text{Eq. 4.46}$$
$$C_3H_6 + OH \rightarrow C_2H_5 + CH_2O \quad \text{Eq. 4.47}$$
$$C_3H_6 + H \rightarrow C_3H_5 + H_2 \quad \text{Eq. 4.48}$$
$$C_3H_6 + CH_3 \rightarrow C_3H_5 + CH_4 \quad \text{Eq. 4.49}$$
$$C_3H_6 + HO_2 \rightarrow C_3H_6O + OH \quad \text{Eq. 4.50}$$
$$C_3H_6 + C_2H_5 \rightarrow C_3H_5 + C_2H_6 \quad \text{Eq. 4.51}$$

The H-atom abstraction reactions are said to require higher activation energies [50] and might not occur in combustion torch jet ignition experiments. The formyl radicals and the formaldehyde oxidizes into CO. The decay reactions of C_3H_6 and C_3 radical species are not reliable to date when compared with other radical species in propane oxidation. The recombination of CH_3, C_2H_3, C_2H_5 in creating large species with higher carbon to hydrogen ratios lead to soot formation under fuel rich conditions for both methane and propane, similar to ethylene.

The importance of all these listed kinetic mechanisms was to give an insight into the creation of the species which emit radiation in the spectral response range of the camera. Knowledge of the species or radical species which radiate in the measurable spectrum and the possible reaction mechanisms that create these radical species will help in discussion of ignition and ignition delay time in the next chapter.

CHAPTER 5. EXPERIMENTAL RESULTS AND DISCUSSION

The chapter reports the ignition study results for ethylene-air, methane-air, and propane-air mixtures. The experimental variables and their effect on ignition are also discussed.

5.1. Ignition Analysis

Ignition analysis conducted for a series of experiments are discussed in this section to familiarize the reader with the methods and procedures used in analyzing the data obtained from the tests and the range of possible test outcomes. The tests conditions and the results for test numbers 096, 118, 136, and 139 are summarized in Table 5.1.

Table 5.1 Test conditions and summary

Test #	Pre-chamber		Main chamber		Diaphragm rupture time, ms	Ignition / no ignition	Ignition frame #	Ignition time, ms	Ignition delay time, ms
	Fuel type	ϕ	Fuel type	ϕ					
136	Ethylene	1.1	Ethylene	0.3	15.6	No	N/A	N/A	N/A
139	Ethylene	1.1	Ethylene	0.8	15.2	Ignition	159	15.8	0.6
118	Ethylene	1.1	Ethylene	1.6	15.5	Ignition	194	19.3	3.8
096	Ethylene	1.1	Ethylene	2.8	15.3	No	N/A	N/A	N/A

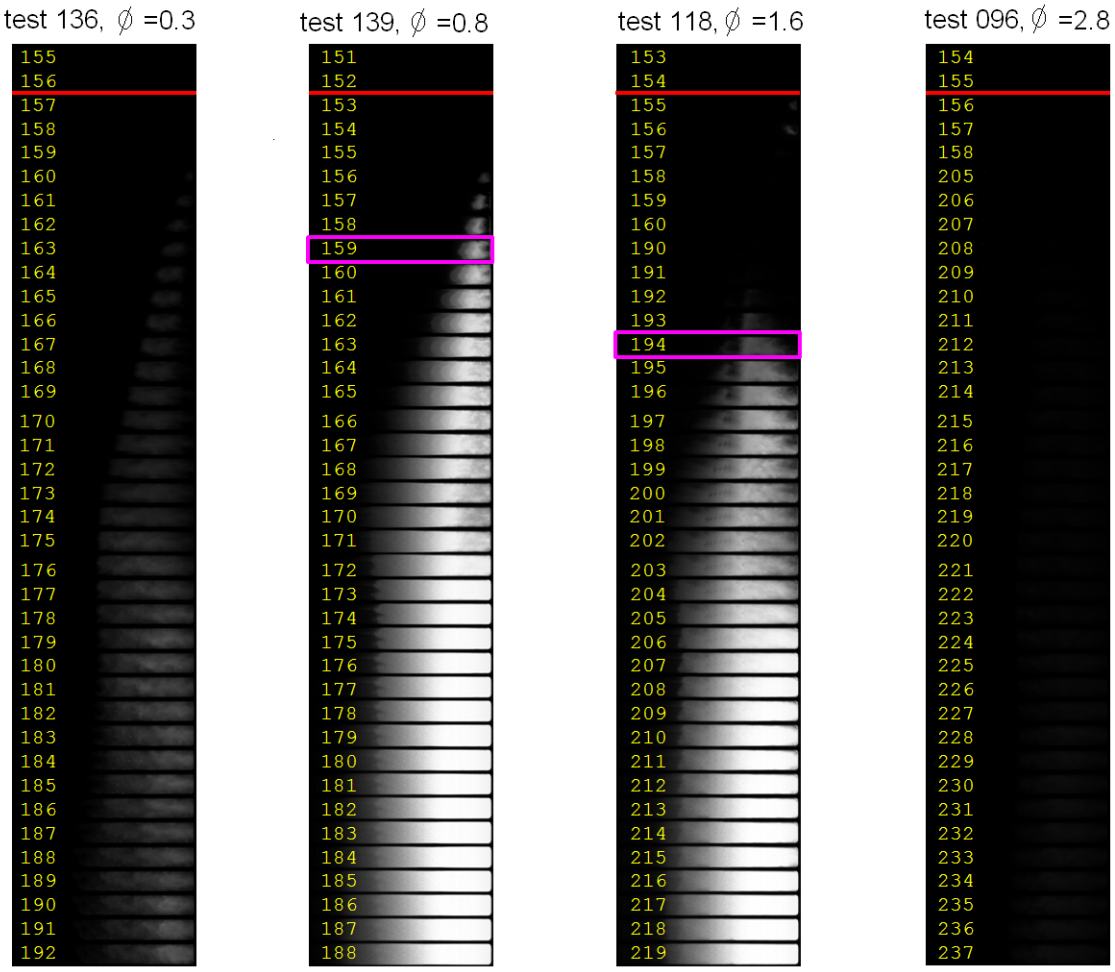

Figure 5.1 Image processed high-speed video images from test # 096, 118, 136, and 139

The intensity of recorded luminosity in test numbers 096, 118, 136, and 139 are illustrated in Figure 5.1. The high-speed video images were captured at 10,000 fps, exposure time of 96.75 μs, and an EDR exposure time of 0 μs. The image frames where ignition was detected according to the threshold values used are outlined in Figure 5.1 for test 139 and 118. The calculated diaphragm rupture time is indicated by red lines for each test. In all tests except test 096 the torch jet entering the main chamber was visible. Since the state of the torch jet was similar in all 4 tests, the variation in the torch jet visibility has to be related to main-chamber equivalence ratio. The torch jet in test 139 was clearly visible, and a finite amount of time after the jet was first visible the torch jet ignites the

ethylene-air mixture in the main chamber. The finite amount of time from the diaphragm rupture to the ignition was assumed as the ignition delay time, as described in Section 4.3. During this time, the torch jet mixed with the ethylene-air mixture in the main chamber. The mixing of the hot combustion products with the ethylene-air mixture, leads to ethylene reacting with the air in the main chamber as well as radicals and other combustion products in the torch jet. The energy required for these chemical reactions are provided by the energy from the torch jet.

In test 118, the torch jet was visible in the first few image frames. The luminosity of the initial jet ceased after some time and a finite amount of time later a luminous region formed in the main chamber. This indicated the region near the entrance to the channel reached a critical temperature, the mixture ignited and the constituents of the burned mixture in this region started emitting radiation in the response spectrum of the camera. It is evident that the constituents in the mixing region had an effect on this observation. The torch jet and the mixing region were visible throughout in test 139 and 136 but with varying intensities, where the main chamber had ethylene lean mixtures (Table 5.1). The torch jet was initially visible and later the mixture region was visible in test 118, where the main chamber fuel-air mixture was ethylene rich (ϕ = 1.6). In test 096 the main chamber ethylene-air mixture was ϕ = 2.8. The initial torch jet was not observable at the image processing levels set. In test 136 the initial jet was visible as well as the mixture began to emit in the response spectrum of the camera, but the luminous region never evolved into an adequate level to go beyond the luminosity threshold defined as ignition in the current study.

The initial pressure and the initial temperature of both the pre-chamber and the main chamber were maintained at atmospheric pressure and room temperature. The pressure histories obtained from PT-0 pressure transducer in the pre-chamber and PT-1 to PT-3 in the main chamber are plotted on separate charts illustrated from Figure 5.2 to Figure 5.5. The captured high-speed video from the tests specified in Table 5.1 were

image processed at default settings. The image processed high-speed images are shown in Figure 5.1.

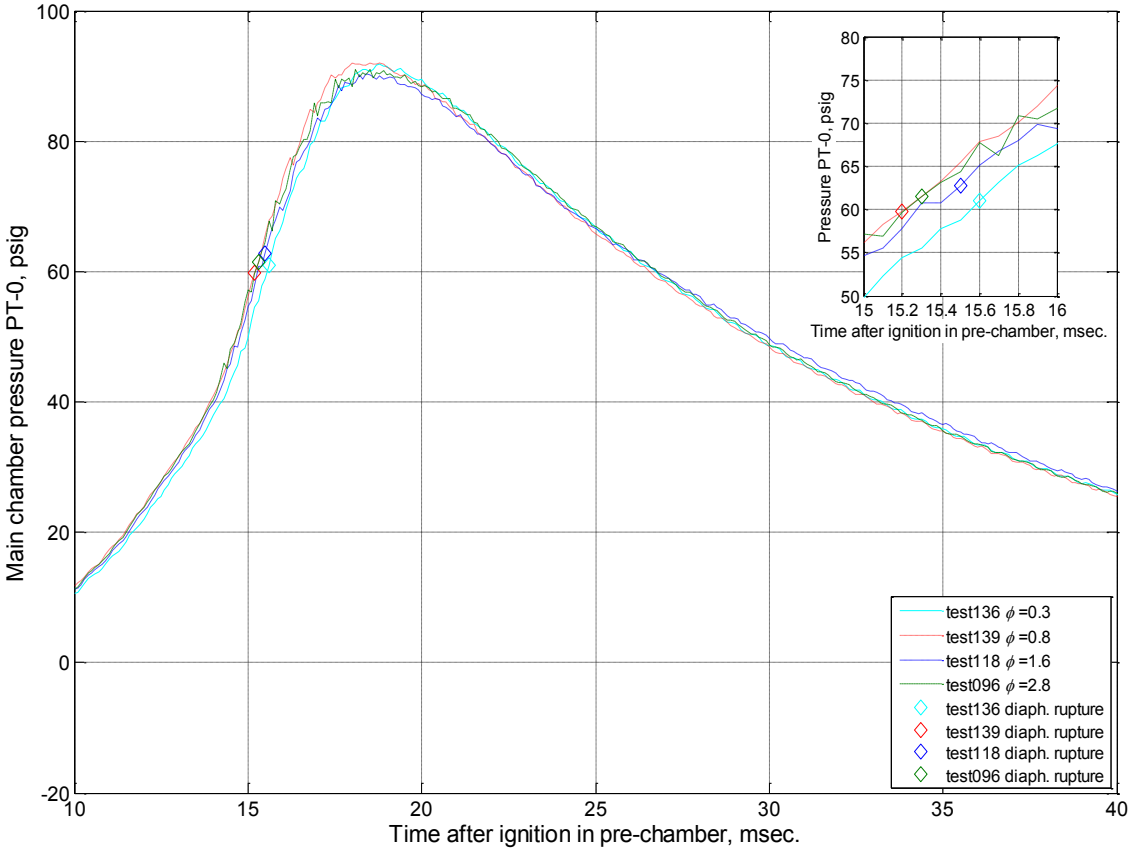

Figure 5.2 Pre-chamber PT-0 pressure histories for test # 096, 118, 136, and 139

The consistent torch jet characteristics are evident from the pressure traces from the pre-chamber pressure transducer PT-0 for the 4 tests. Including the diaphragm rupture, diaphragm rupture pressure, and maximum pressure rise. The diaphragm rupture event for the test numbers 139, 096, 118, 136 are also indicated in Figure 5.2.

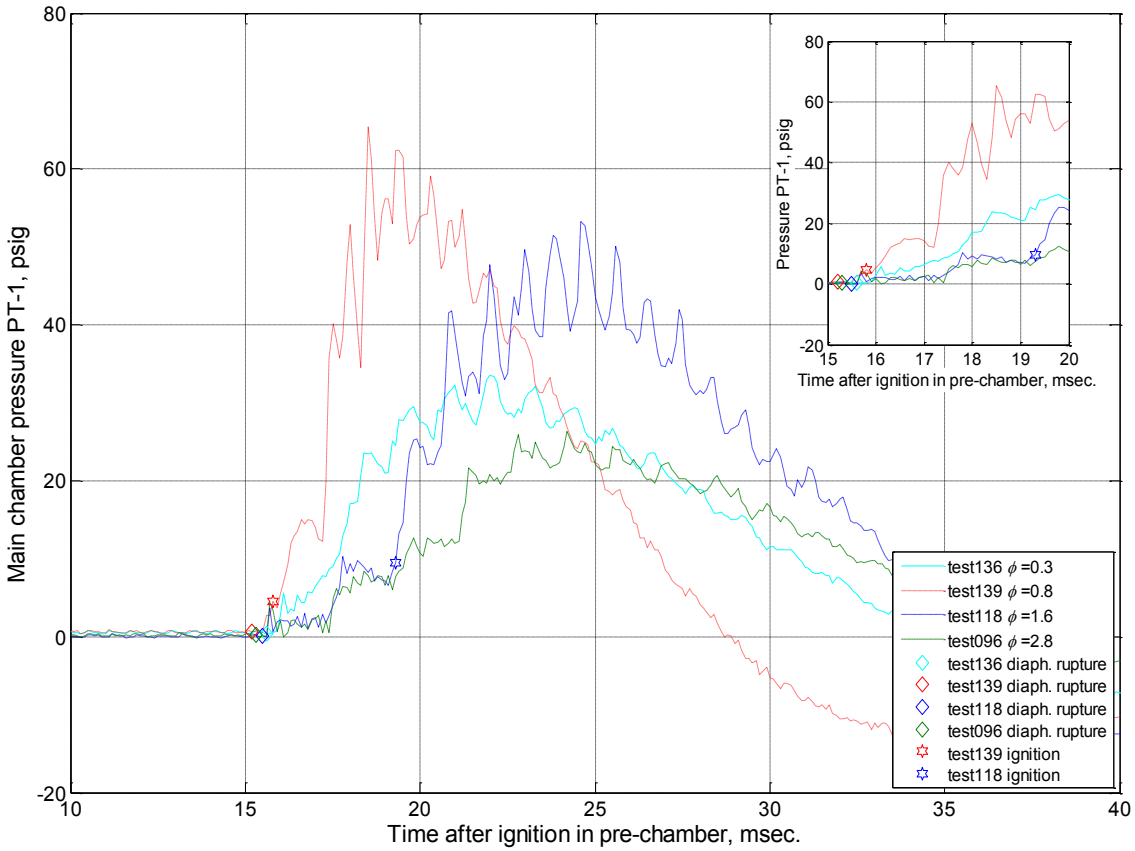

Figure 5.3 Main chamber PT-1 pressure histories for test # 096, 118, 136, and 139

The successive ignition in the main chamber from the combustion torch jet was denoted for tests # 139 with ϕ = 0.8 and 118 with ϕ = 1.6 respectively in Figure 5.3. In addition to the ignition, the diaphragm rupture time for all 4 tests are also denoted. The ignition event was computed using the image processing method described in Section 3.6 and superimposed on the pressure history data obtained from the pressure transducers.

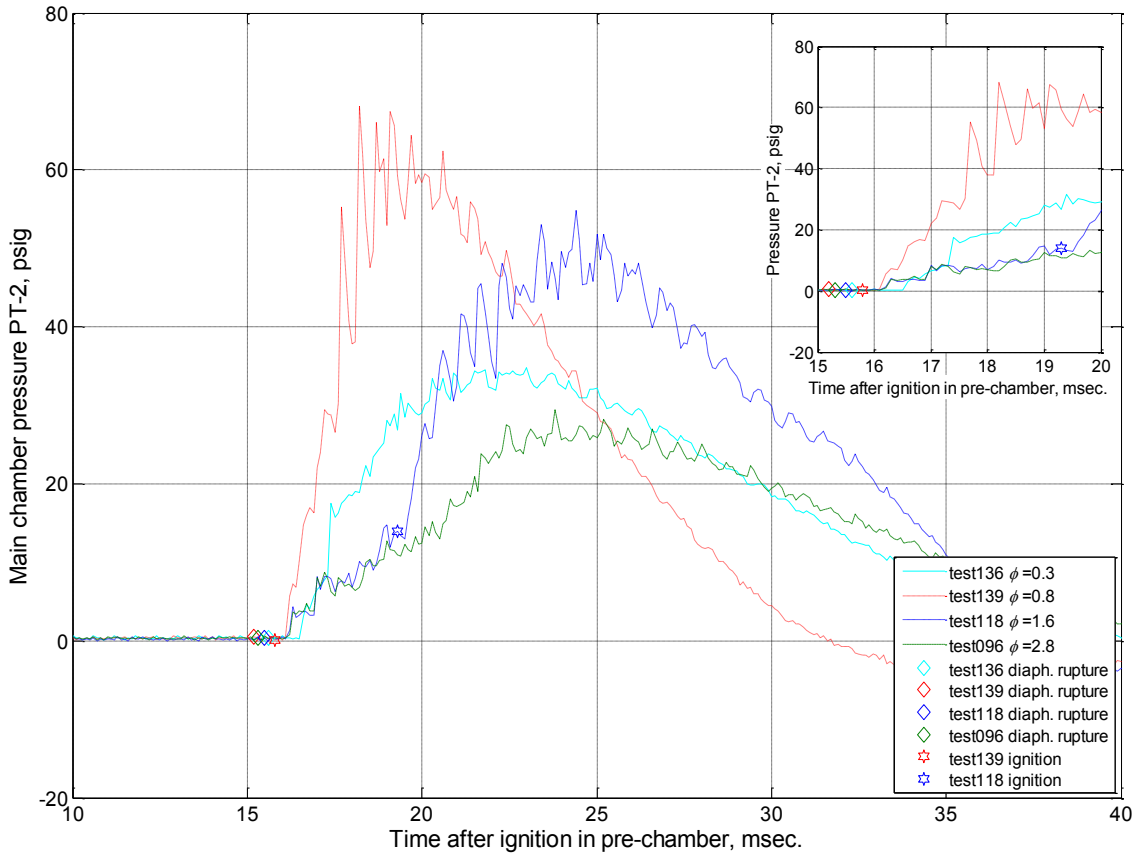

Figure 5.4 Main chamber PT-2 pressure histories for test # 096, 118, 136, and 139

The ignition in test 139 was evident in high-speed video images as well as the pressure transducer measurements from the main chamber. The high intensity of emitted luminosity in frame # 159 in Figure 5.1, develops and increases in area in the subsequent frames indicating ignition. The PT-1 transducer trace show a pressure rise of approximately 15 psi in less than 1 ms after the image processed ignition event. The steepness of the pressure gradient in test 139 compared to the other 3 tests, conducted with the same ethylene ϕ = 1.1 torch jet can also be used to conclude that there was ignition in the in the main chamber.

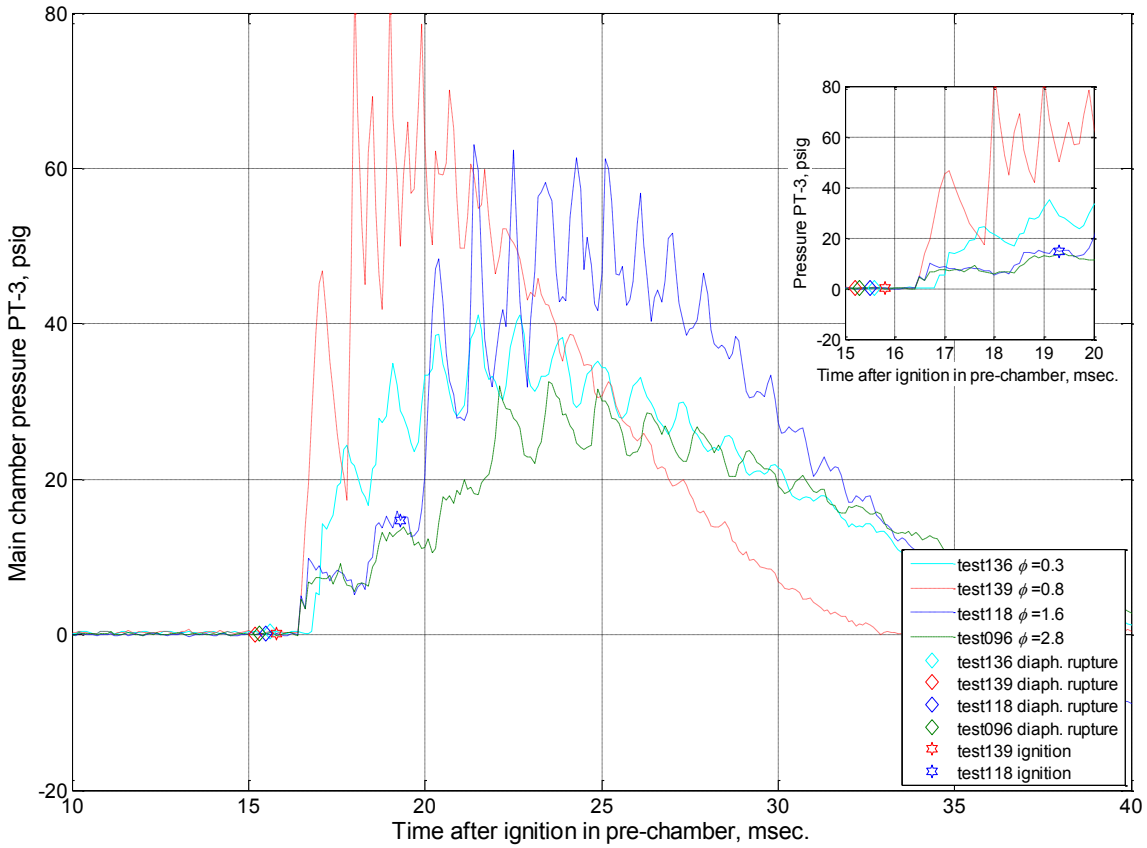

Figure 5.5 Main chamber PT-3 pressure histories for test # 096, 118, 136, and 139

The test 136 with ϕ = 0.3 indicated there was a significant pressure rise at all pressure transducer locations in the main chamber (Figures 5.3 to 5.5). The pressure rise in test 136 was quicker and the pressure magnitude was larger compared to test 118 in the initial phase. Since the luminous intensity and luminous region in test 136 didn't exceed the threshold limits used to define ignition in the current study, test 136 was classified as there was no ignition in the main chamber although there was limited amount of luminosity in the main chamber as indicated in Figure 5.1. The pressure traces and image processing method both concluded that there was ignition in the main chamber in test 118. Figures 5.3 to 5.5, illustrate there was a longer ignition delay in test 118 compared to test 139. The pressure gradually increased in test 118 until the pressure spike due to combustion compared to the instant pressure rise in test 139. The time lag between the ignition marked on the pressure traces in Figures 5.3 to 5.5 (computed by image

processing the high-speed video images) and steep pressure rise in pressure transducer measurements was due to the spatial effects. This is because; the pressure fluctuations take time to propagate from the ignition location to the pressure transducer locations.

5.2. Ignition Identification with Change of the Fuel

The intensity of the radiation emitted from the luminous mixing region in the main chamber was observed to change with different main chamber equivalence ratios even with the same fuel in the Section 5.1. The following analysis based on the high-speed images indicated that, the effect of varying the main-chamber fuel had no significant effect on the ignition definition used in the current study.

5.2.1. Image Processed Inspection of High-Speed Video for Fuel-Air Mixture Ignition

Results from the analysis of test numbers 136, 137, 156, 159, 164, 241, 245, and 249 are used in the following discussion. The initial experimental variables and the test results are summarized in Table 5.2 below. Tests from ethylene-air, propane-air, and methane-air ignition limit equivalence ratios were compared to assess the reliability of the threshold used in determining ignition event when the fuel type is varied.

The high-speed video camera settings and image processing setting used were the same as the settings used in Section 5.1. The sequence of images as time passes are arranged one image below the other in Figures 5.6 to 5.8. The frame number of each image in the sequence from ignition trigger signal in the pre-chamber is labeled on the left of each image.

Table 5.2 Test conditions and results summary for lean limit ignition

Test #	Pre-chamber		Main chamber		Diaphragm rupture time, ms	Ignition / no ignition	Ignition frame #	Ignition time, ms	Ignition delay time, ms
	Fuel type	ϕ	Fuel type	ϕ					
136	Ethylene	1.1	Ethylene	0.3	15.6	No	N/A	N/A	N/A
137	Ethylene	1.1	Ethylene	0.4	15.1	Ignition	171	17.0	0.6
164	Ethylene	1.1	Propane	0.3	14.9	No	N/A	N/A	N/A
159	Ethylene	1.1	Propane	0.4	14.9	Ignition	183	18.2	3.3
156	Ethylene	1.1	Propane	0.6	14.6	Ignition	173	17.2	2.6
241	Ethylene	1.1	Methane	0.3	14.6	No	N/A	N/A	N/A
245	Ethylene	1.1	Methane	0.4	15.2	Ignition	198	19.7	4.5
249	Ethylene	1.1	Methane	0.6	14.8	Ignition	180	17.9	3.1

Test 136 images are on the left and test 137 images are arranged on the right of Figure 5.6. The jet is visible from the initial penetration in both tests. The first few images in the two sequences were identical, but the latter images varied in both the increase of the luminous region and the intensity of the luminous. The luminosity of the jet and the mixing increased in both tests at different intensities but the defined ignition threshold was not reached in test 136 (ϕ = 0.3). In test 137 (ϕ = 0.4), the torch jet penetrating into the combustible mixture in the main chamber, the subsequent increase in the luminosity in the mixing region, and the flame propagation to the closed end of the main chamber is clearly visible in Figure 5.6.

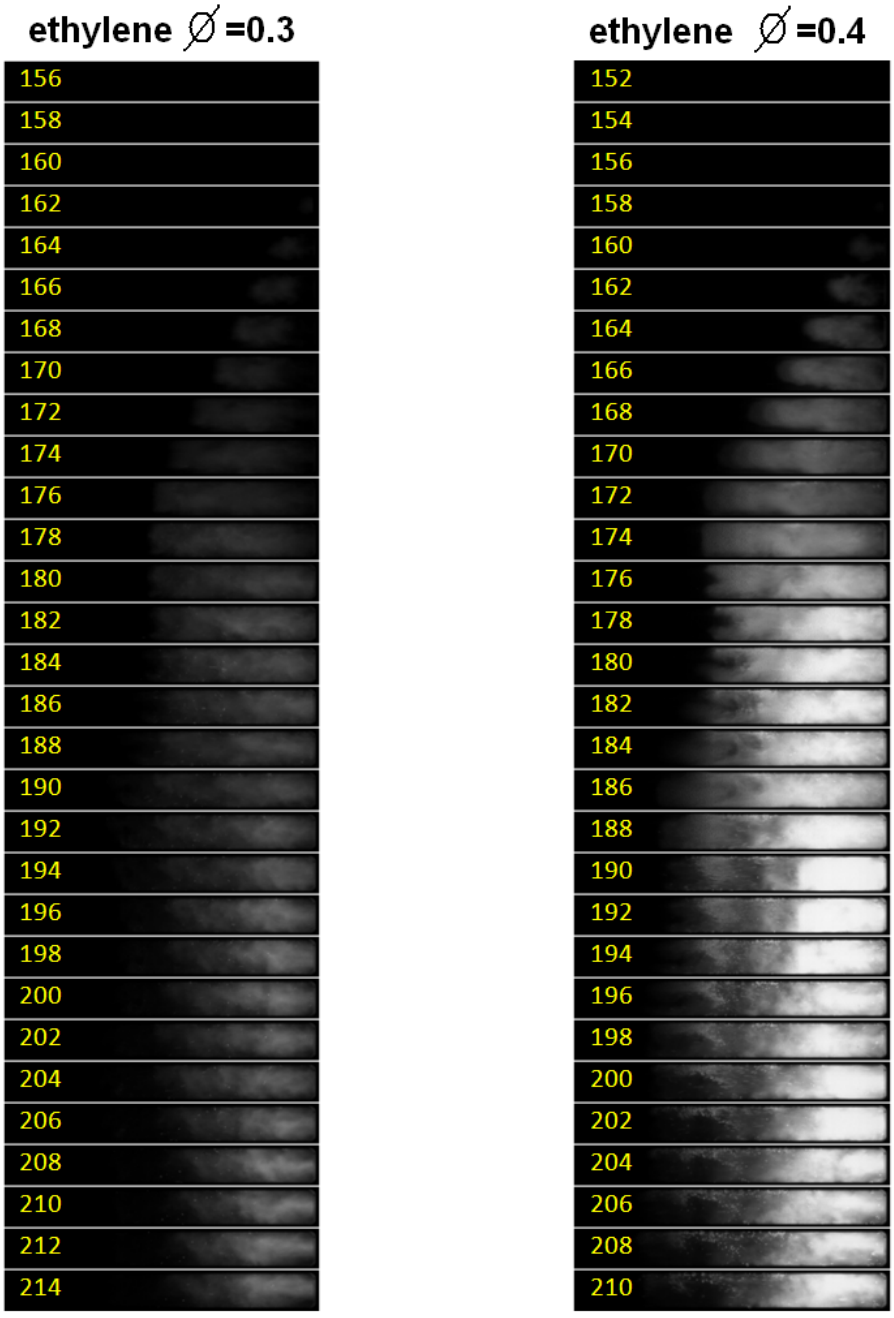

Figure 5.6 Ethylene ignition lean limit from tests # 136 (left) and 137 (right)

The only possible reason for this increase in luminosity and increased luminous area in the mixing region was ignition in test 137 and therefore test 137 was concluded as

an ignition test while test 136 was designated as a no ignition. These conclusions were purely based on image processing criterion defined for ignition although, the pressure transducer measurements indicated (Section 5.1) a “weak-combustion” that was not detectable with the visual inspection. The level of ambiguity in the method was reduced by the use of the computer based image processing method described in Section 3.6 as compared to a manual inspection method. The luminosity level and the luminous region gradually decreased in both tests after the sequence of images displayed in Figure 5.6. Similar analyses were carried out for both lean and rich ignition limits for propane and methane ignition limit equivalence ratios.

Propane ignition limit ranged from equivalence ratio 0.3-0.4 on the propane lean side to 2.2-2.4 on the propane rich side. In these propane-air mixtures in the main chamber tests (test numbers 156, 159, and 164), the torch jet initial penetration was not visible but when the torch jet mixed with the main chamber propane-air mixing region was visible. The addition of hot combustion torch jet products lead to the main chamber increasing in luminosity but at different luminous levels of intensity. The light intensity of the mixture in test 156 increasing after frames # 182-184, as illustrated in Figure 5.7. A similar but greater luminosity increase was displayed in test 156 from frames # 180-184. These two tests were identified as ignition cases by the image processing method. Test 164 showed no visible luminosity until frame # 194 and remained at the same luminosity level until the torch jet ceased. This was due to, the reduction in pressure in the pre-chamber owing to the mass outflow from the pre-chamber into the main chamber. Therefore test 164 (propane $\phi = 0.3$) test was not considered as an ignition test.

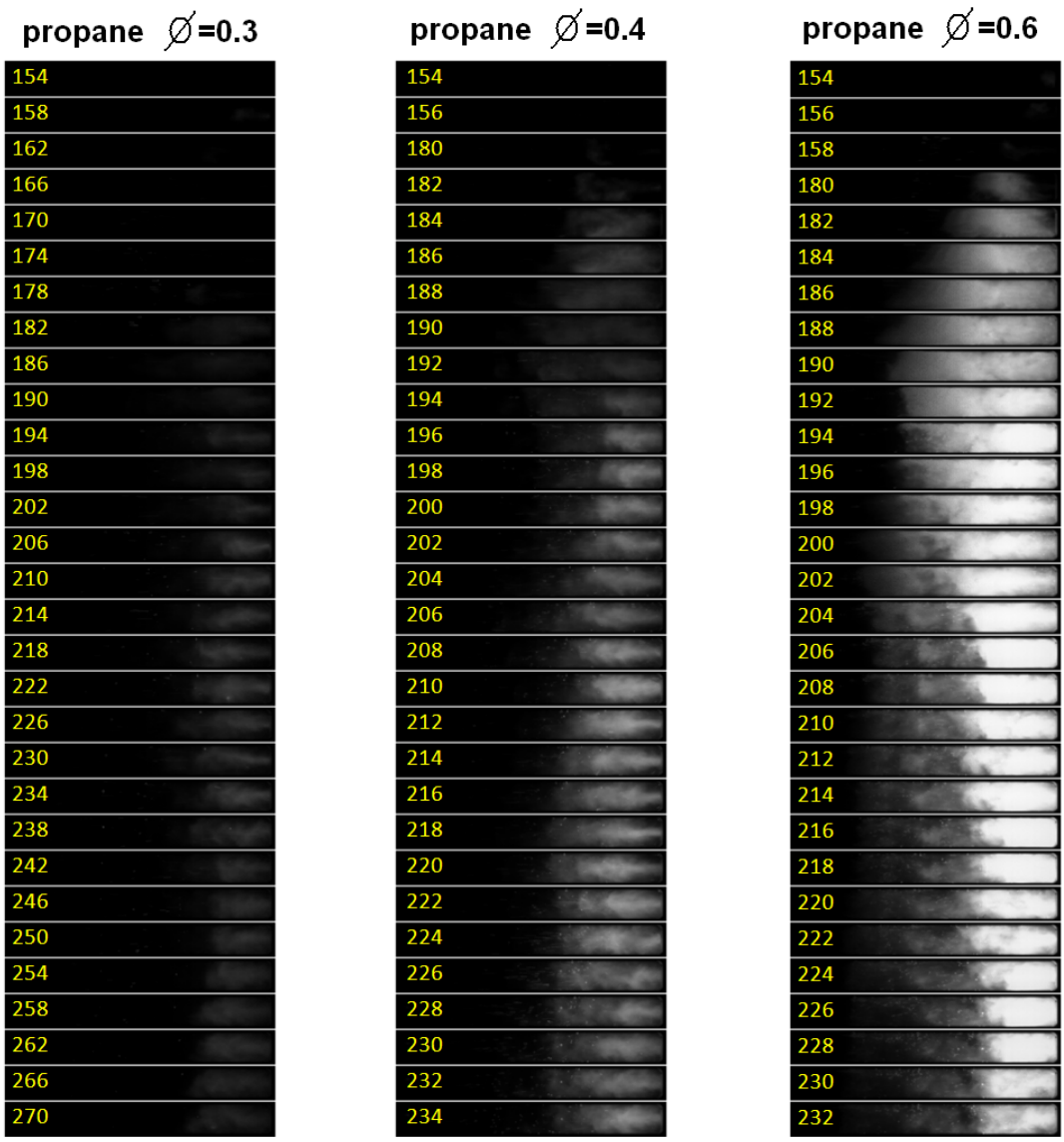

Figure 5.7 Propane ignition lean limit from tests # 164 (left), 159 (middle), and 156 (right)

Methane lean limit was analyzed the same way, using captured images from test numbers 241, 245, and 249 and is illustrated in Figure 5.8. The luminosity increased in both test numbers 245 and 249 approximately after frames # 198 to 200 and 180 to182 respectively. Test 241 indicated very low luminosity from frames # 206 to 286. This

luminosity did not reach the predetermined threshold value defined as ignition and therefore was classified as a no ignition test in the main chamber.

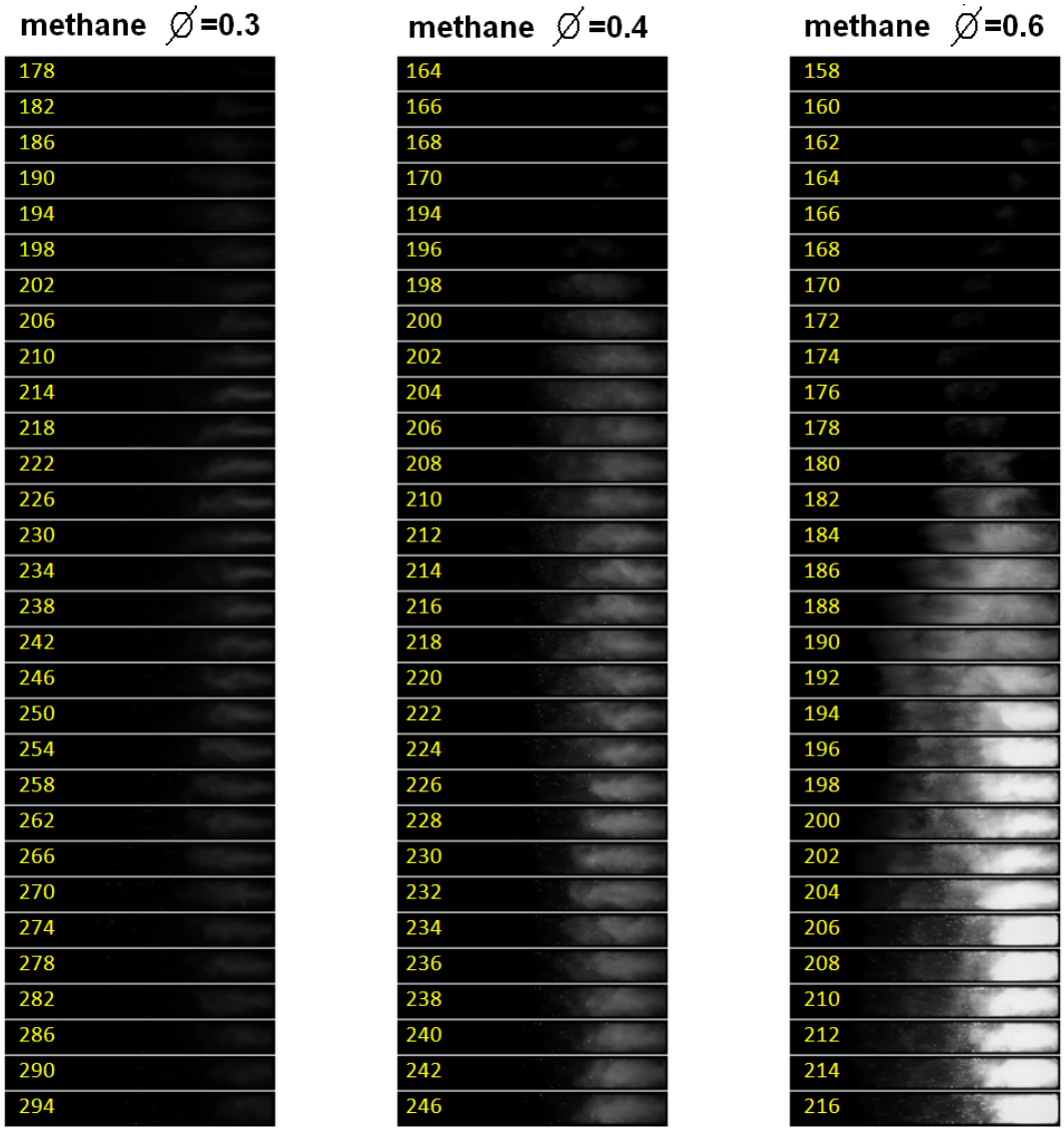

Figure 5.8 Methane ignition lean limit from tests # 241 (left), 245 (middle), and 249 (right)

Similar analysis was preformed for the fuel rich ignition limit for all three fuels and the results are given in Table 5.3. The rich ignition limit of both ethylene and

propane equivalence ratios ranged from 2.2 to 2.4 where a number of test indicated ignition and others did not. This is further discussed in later in the chapter. The methane tests showed a similar variation at the rich limit of 1.2 to 1.4, where not all tests at this limit would be classified as an ignition test.

Table 5.3 Test conditions and results summary for rich limit ignition

Test #	Pre-chamber		Main chamber		Diaphragm rupture time, ms	Ignition / no ignition	Ignition frame #	Ignition time, ms	Ignition delay time, ms
	Fuel type	ϕ	Fuel type	ϕ					
112	Ethylene	1.1	Ethylene	2.2	15.5	Ignition	223	22.2	6.7
105	Ethylene	1.1	Ethylene	2.4	15.4	No	N/A	N/A	N/A
110	Ethylene	1.1	Ethylene	2.6	15.5	No	N/A	N/A	N/A
190	Ethylene	1.1	Propane	2.2	14.6	Ignition	238	23.7	9.1
167	Ethylene	1.1	Propane	2.4	14.8	No	N/A	N/A	N/A
191	Ethylene	1.1	Propane	2.6	14.5	No	N/A	N/A	N/A
274	Ethylene	1.1	Methane	1.2	14.6	Ignition	250	24.9	10.3
270	Ethylene	1.1	Methane	1.4	14.6	Ignition	285	28.4	13.8
266	Ethylene	1.1	Methane	1.6	14.5	No	N/A	N/A	N/A

The only ambiguity in using the image processing method to identify ignition was the predetermined luminosity of the threshold used. In order to eliminate the ambiguity associated with the 10% threshold, an alternative threshold of 1% of the full scale signal was used to analyze the same test cases. The results of this alternate threshold are compared against the 10% threshold in Table 5.4.

The ignition analysis using the 10% full-scale signal threshold and the analysis using the 1% full-scale signal threshold limit generated the same classification of ignition success. The ignition and the no ignition outcome remained the same for both threshold

limits. The only variation was the reduction in the ignition delay time for test 249 by 0.1 ms.

Table 5.4 Comparison of image processing threshold

Test #	Diaph. rupture time, ms	10% full scale signal				1% full scale signal			
		Ignition / no ignition	Ignition frame #	Ignition time, ms	Ignition delay time, ms	Ignition / no ignition	Ignition frame #	Ignition time, ms	Ignition delay time, ms
136	15.6	No	N/A	N/A	N/A	No	N/A	N/A	N/A
137	15.1	Ignition	171	17.0	1.9	Ignition	171	17.0	1.9
164	14.9	No	N/A	N/A	N/A	No	N/A	N/A	N/A
159	14.9	Ignition	183	18.2	3.3	Ignition	183	18.2	3.3
241	14.6	No	N/A	N/A	N/A	No	N/A	N/A	N/A
245	15.2	Ignition	180	17.9	3.1	Ignition	179	17.8	3.0

5.2.2. Pressure Trace Inspection of Fuel-Air Mixture Ignition

In order to identify ignition, comparison of the pressure history in the main chamber for test numbers 135, 136, and 137 were selected. The initial conditions of the pre-chamber and the main chamber are given in Table 5.5. In addition to this, the image processed ignition information at the threshold of 10% full-scale signal is provided in Table 5.5.

The pressure traces at the pressure transducer locations for test numbers 135, 136, and 137 are illustrated in Figures 5.9 to 5.12. The pre-chamber pressure histories for the said tests are shown in Figure 5.9 and the main chamber pressure transducer measurements are given in Figures 5.9 to 5.12. The pre-chamber pressure variations were similar in the 4 tests since the fuel, the equivalence ratio, and the pre-chamber initial conditions were are maintained as described in Table 5.5. The rupture time of the diaphragm varied from 15.0-15.6 ms, but this was within the diaphragm rupture variation for pre-chamber tests. Test 136 indicated the largest diaphragm rupture time and also had

the highest maximum pressure in the pre-chamber. This higher pressure in the pre-chamber for test 136 might be attributed to the delay in the rupture time of the aluminum diaphragm leading to a higher pressure built-up in the pre-chamber. This can be verified by the diaphragm rupture pressure as well.

Table 5.5 Pressure trace comparison for test 135, 136, and 137

Test #	Pre-chamber		Main chamber		Diaphragm rupture time, ms	Ignition / no ignition	Ignition frame #	Ignition time, ms	Ignition delay time, ms
	Fuel type	ϕ	Fuel type	ϕ					
135	Ethylene	1.1	Ethylene	0.2	15.0	No	N/A	N/A	N/A
136	Ethylene	1.1	Ethylene	0.3	15.6	No	N/A	N/A	N/A
137	Ethylene	1.1	Ethylene	0.4	15.1	Ignition	171	17.0	0.6

Pressure histories from the main chamber pressure transducers for test 135 indicated pressure fluctuations which were similar to tests conducted with either no fuel in the main chamber or a main chamber filled with an ethylene-air mixture of ϕ = 0.1. These pressure variations were generated from the fluid dynamic phenomena associated with the high-pressure under-expanded nozzle flow from the pre-chamber entering the main chamber. No ignition was detected in test 135 with the image processing method confirming this conclusion. Test 136 and 137 indicated similar pressure fluctuation, but the pressure peaks were much steeper and the pressure magnitudes were higher in test 137 as compared to test 136. The pressure rise in the main chamber pressure transducers in test 136 indicated although pressure increased in the main chamber it was not sufficient to generate a sustainable combustion in the main chamber resulting in a "weak-combustion." The existence of high temperature gas mixture near the PT-1 pressure transducer was identified by the thermal drift effect, where the PT-1 pressure transducer reference pressure shifted down from 0 psig at the beginning of the tests to approximately -5 to -10 psig vacuum pressure near the end of the experimental observation time. This thermal drift effect was not observed at PT-2 for test 135 and 136, or at PT-3 location for any tests (Figures 5.11 and 5.12).

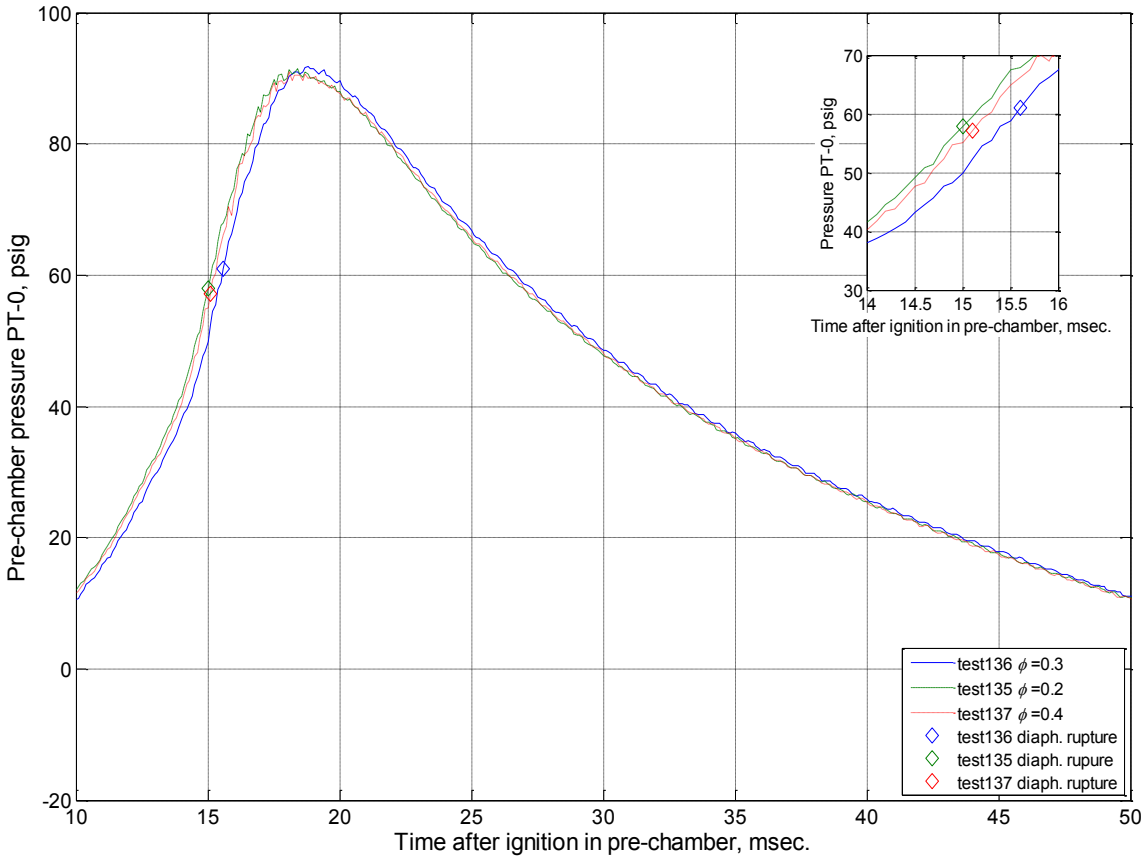

Figure 5.9 Pre-chamber pressure histories for lean limit tests

The steepness of the pressure rise was higher at PT-2 and PT-3 pressure transducer locations in test 137, when compared to the same pressure transducers in test 136. The measured pressure at pressure transducer locations in test 136 indicated local pressure fluctuations similar to test 137. Since, the pressure rise of the ethylene-air mixture in a constant volume combustor is proportional to the heat released in the chemical reactions; test 136 was regarded as the limit of lean limit equivalence ratio. This was concluded as the reason behind the lack of radiation in the response spectrum of the camera for test 136.

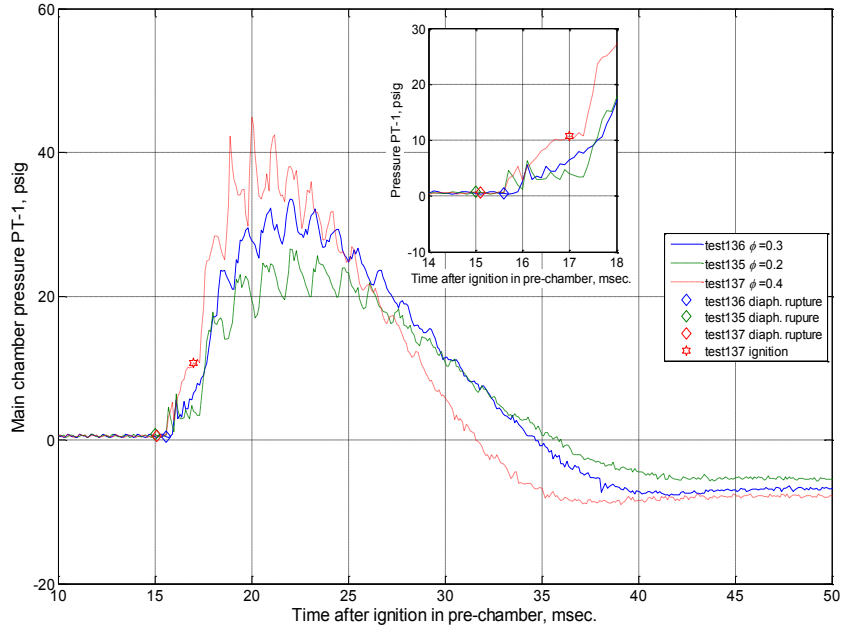

Figure 5.10 Main chamber PT-1 pressure transducer pressure measurement for lean limit tests

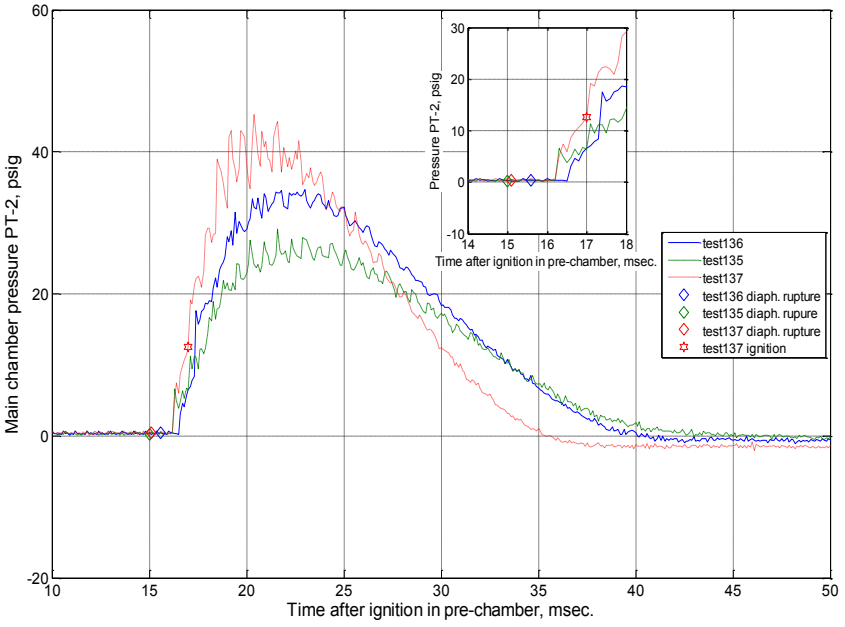

Figure 5.11 Main chamber PT-2 pressure transducer pressure measurement for lean limit tests

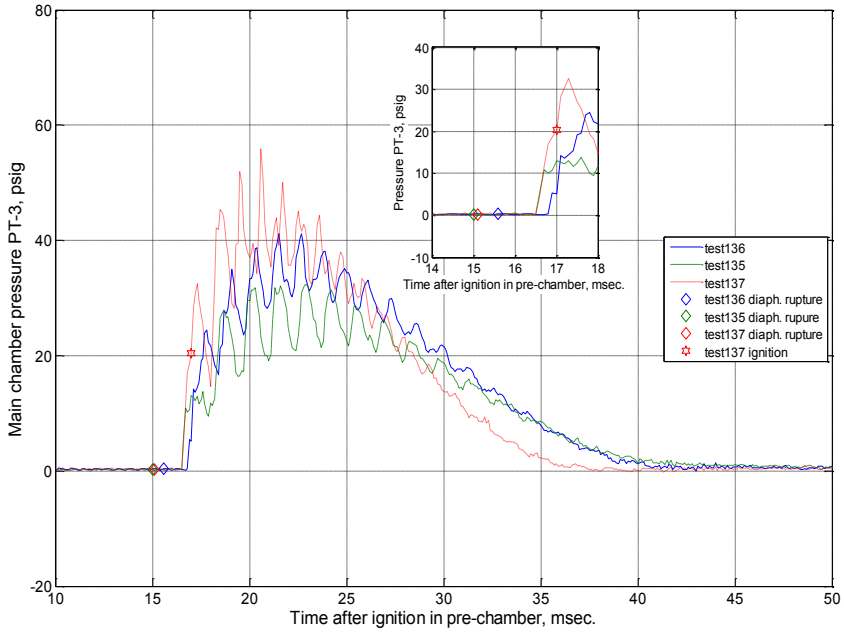

Figure 5.12 Main chamber PT-3 pressure transducer pressure measurement for lean limit tests

Similarly, the fuel rich and fuel lean ignition limits for all three fuels were identified. These ignition limit equivalence ratios are applicable only to the hot combustion torch jet initial conditions and nozzle geometry used in the study.

5.3. Nozzle Geometry Variations on Ignition Delay Time

The pre-chamber combustion torch jet nozzle used for all preliminary tests used Nozzle # 1. In order to identify an appropriate nozzle for the main study a series of experiments were conducted with different nozzle inserts with varying cross-sectional areas and geometries. The nozzles used are listed in Table 2.2. The area variation and the exit and throat diameters are also specified in the table. The design drawings of the nozzles are in Appendix B.

The pre-chamber and the main chamber for these tests were maintained at ethylene-air equivalence ratios of 1.1 and 1.0. In total, 19 tests were conducted in the series with all of them rupturing the aluminum diaphragm in the desired manner. The

ignition delay results are indicated in Figure 5.13. Ignition was not detected in the main chamber for 4 tests which were conducted with nozzles # 4 and 5. From the tests in which ignition was detected in the main chamber, 3 tests were not conclusive as to whether the torch jet or the aluminum diaphragm debris ignited the main chamber combustible mixture. Figure 5.13, illustrates only the tests where ignition was detected that was initiated by the torch jet. The minimum ignition delay times were observed for nozzles # 1 and 7, while nozzle # 6 had the longest ignition delay times. Nozzles # 1-4 were convergent nozzles with curved internal walls varying in only the throat diameter as specified in Table 2.2.

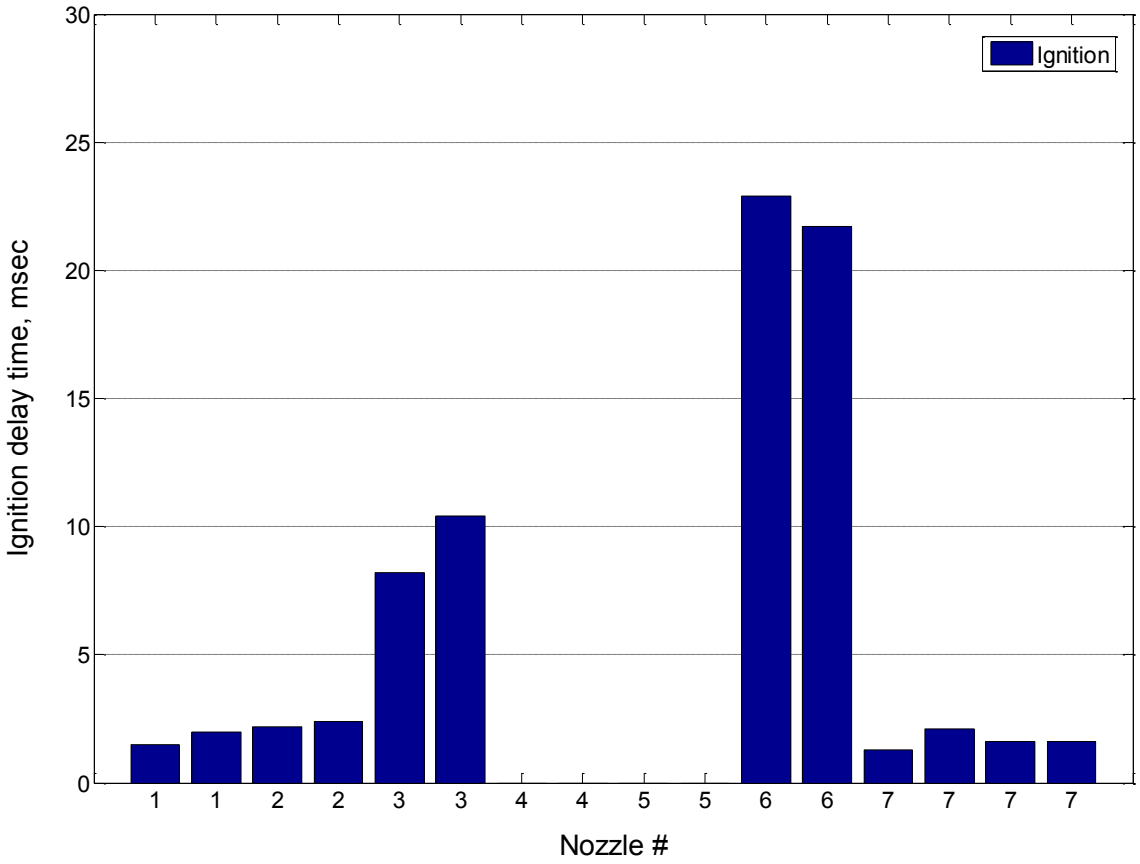

Figure 5.13 Ignition delay of with different nozzles

As the nozzle throat diameter decreased, the ignition potential of the torch jet deceased until in nozzle # 4 where there was no ignition detected in the main chamber.

This is due to the heat loss in the combustion torch jet to the nozzle walls as the torch jet was forced to travel through a narrow throat exit. A quadratic correlation was found between the nozzle throat to nozzle inlet area ratio and the ignition delay time for these converging nozzles.

The same observation was made with the nozzles # 5 and 7. These nozzles were straight-cone converging-diverging (De Laval) nozzles with identical inlet diameters. The throat diameter and the exit diameter were different in the two nozzles. Nozzle # 5 had a larger heat loss due to its smaller throat and exit diameters compared to nozzle # 7. Nozzle # 6 had a hemispherical converging section and a straight-cone diverging section. The converging section of this nozzle had the largest surface area to volume ratio compared with the other nozzles and had the longest ignition delay time observed for the nozzles tested.

Nozzle # 1 was selected for the main study due to lower ignition delay time observed from these studies. In addition to this reason nozzle # 1 was preferred over nozzle # 7 since all the preliminary testing was carried out with nozzle # 1.

5.4. Pre-Chamber Equivalence Ratio Effect on Ignition Delay Time

Pre-chamber equivalence ratio effect on the ignitability of the main chamber from the combustion torch jet was investigated with a range of test. Ethylene was used as the pre-chamber fuel due to lower ignition delay time and higher maximum pressure rise after diaphragm rupture (Table 3.1) compared to propane and methane. The main chamber was fueled with ethylene, propane, and methane mixtures of 1.0 equivalence ratio at atmospheric pressure and room temperature to observe the effect of pre-chamber equivalence ratio for the different fuels.

The pre-chamber initial pressure and the initial temperature were sustained at atmospheric pressure and room temperature for all experiments, while the pre-chamber equivalence ratio was varied. This series of experiments contained 30 tests, with all 30 of

the diaphragms rupturing into 4 symmetric petals. All main chamber fuel-air mixture ignited except in propane and methane mixtures injected with the lean ethylene torch jets produced in the pre-chamber. There was no observable evidence in any of these tests of aluminum diaphragm debris initiated ignition in the main chamber from the high-speed camera images. The pre-chamber ethylene-air equivalence ratio was varied from 0.6 to 1.5. Figure 5.14, illustrates the ignition time variation to the pre-chamber for all three fuel-air mixtures of equivalence ratio 1.0.

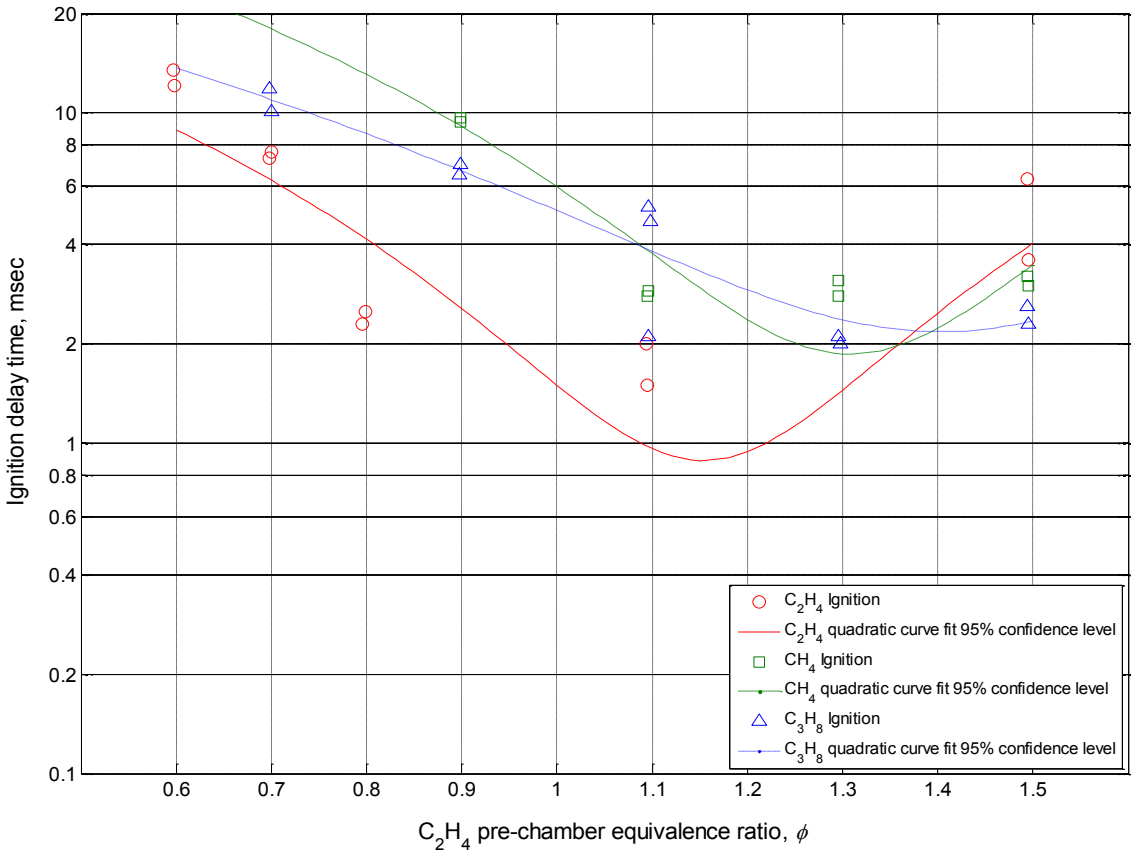

Figure 5.14 Ignition delay time vs. different pre-chamber equivalence ratios

Figure 5.14 illustrates the ignition delay time in the main chamber and the quadratic curve fits that were plotted based on the experimental data. The minimum ignition delay times corresponded to pre-chamber ethylene-air equivalence ratios of 1.1 and above. Although the curve fit data indicated that propane and methane ignition delay

time to be lower for pre-chamber torch jet initial equivalence ratios of 1.3 to 1.5 the experimental data points were used in deciding upon the pre-chamber initial equivalence ratio for the main testing. Therefore, a slightly richer ethylene-air mixture of equivalence ratio 1.1 was selected for the pre-chamber torch jet in the main study. The same ignition delay time information was used to plot a chart of ignition time delay vs. adiabatic flame temperature instead of ignition delay time vs ethylene equivalence ratio as illustrated in Figure 5.15.

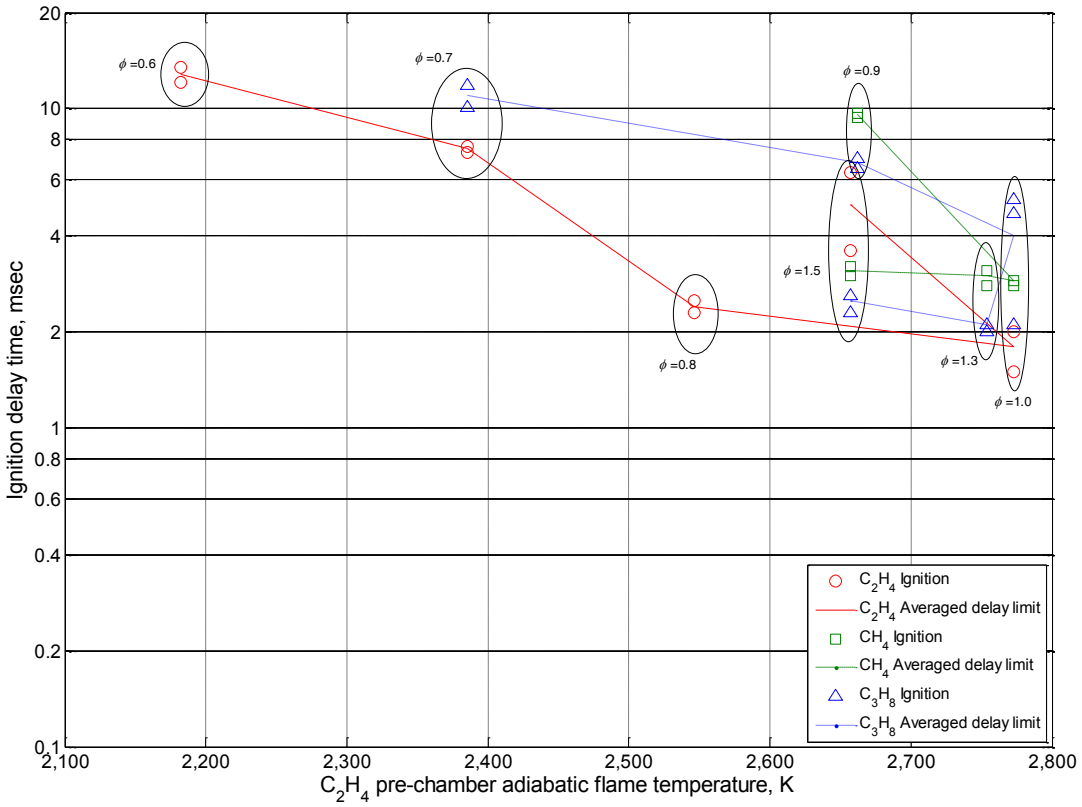

Figure 5.15 Ignition delay time variation to different pre-chamber adiabatic flame temperatures

Figure 5.15, indicates the ignition delay time with computed adiabatic flame temperature. This adiabatic flame temperature was calculated for the pre-chamber ethylene-air equivalence ratio. These adiabatic flame temperature were calculated assuming the energy released in the combustion does not dissipate as heat to the pre-

chamber material. The computer code for equilibrium products of hydrocarbon-air combustion "UVFLAME" supplied with [51] was used for these calculations.

Figure 5.15, illustrates the variation of ignition delay time with adiabatic flame temperature. Assuming that the adiabatic flame temperature is related to the combustion torch jet temperature in the sense if adiabatic flame temperature of a combustible mixture is high the torch jet temperature is also high, as the ethylene-air equivalence ratio increases, the ignition delay time reduces due to the increase in the combustion torch jet temperature. This reduction in the ignition delay time stop when the equivalence ratio of 1.1 is reached, afterwards the ignition delay time increases with the increase in equivalence ratio. This might be attributed to the reduction in the calculated adiabatic flame temperature as the equivalence ratio is increased from ethylene equivalence ratio of 1.1.

The variation of the pre-chamber equivalence ratio causes the adiabatic flame temperature to vary. The pre-chamber ethylene-air ϕ = 1.1 mixtures have the same adiabatic flame temperature, but the ignition delay time varies from 1.5 ms to 5 ms as the main chamber fuel type was changed. This is directly related to the chemical kinetics of the three different fuels at the temperature in the mixing region. This mixing region was discussed in Section 5.1. Methane had the highest ignition delay due to the slow chemical kinetic mechanisms associated with methane as discussed in Section 4.4. Although the adiabatic flame temperature of ethylene-air ϕ = 1.3 is slightly lower than for ethylene-air ϕ = 1.1, the ignition delay times were similar in magnitude for propane-air ϕ = 1.0 in the main chamber.

The ignition delay time in the main chamber decreased until a local minimum is approached at pre-chamber ethylene-air equivalence ratios close to 1.0, and then deviated in the direction of increasing ignition delay time. Both, methane and propane appear to have a lower ignition delay time in the pre-chamber ethylene-air rich experiments compared to the ethylene-air lean experiments. Ethylene ignition delay time varied contradicting this trend at higher equivalence ratios. This is indicated by the change of

direction in the ethylene observed delay limit line after ethylene-air equivalence ratio 1.1 compared to propane and methane observed delay limit lines in Figure 5.15.

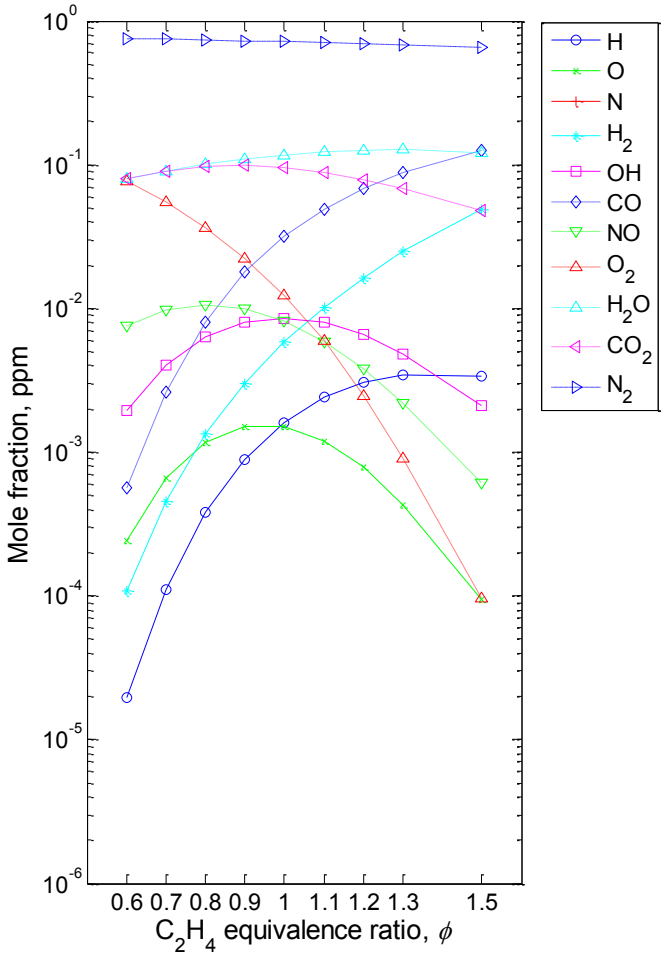

Figure 5.16 Mole fraction of product species generated from combustion of ethylene-air mixtures under constant volume conditions

Alternatively the reduction of the ignition delay time at ϕ = 1.1 can be explained using the radical species present in the combustion torch jet. Figure 5.16, illustrates the product species generated in the combustion of ethylene-air mixtures at different initial equivalence ratios. The UVFLAME computer code [51] was used to calculate the equilibrium composition of the combustion products. The amount of OH, O, and H radicals are all high at the equivalence ratio of 1.1 relative to the three radical levels at the

other equivalence ratios. Although, these values for the product species are computed at equilibrium conditions, similar increase of radicals can be expected for ethylene-air mixture of equivalence ratio of 1.1 at time of diaphragm rupture in the pre-chamber. These radicals in the torch jet will initiate the ignition in the main chamber reducing the ignition delay time when compared with torch jets generated with other equivalence ratios; provided the torch jet is of sufficient temperature.

5.5. Ethylene Experiments

All ethylene experiments were conducted with the initial pressure and initial temperature in the pre-chamber and the main chamber maintained at atmospheric pressure and room temperature. The experiments were conducted by varying the equivalence ratio in main chamber from 0.1 to 3.0 while maintaining the equivalence ratio in the pre-chamber at 1.1 with the nozzle # 1. A total of 60 tests were conducted under these conditions and in three tests the diaphragm did not rupture into 4 symmetric petals. From the remaining tests, 33 mixtures ignited. In the other tests the main chamber mixture did not ignite. Based on the high-speed video images 8 ignition cases were defined as ignited by the diaphragm debris. If the ignition in the main chamber initiated (increase in the luminous intensity from no luminosity) near diaphragm debris, the test was classified as a ignition due to diaphragm debris with visual inspection. Every test case was visually inspected for the probability of the main chamber combustible mixture igniting with diaphragm debris using the Phantom Camera Control software by adjusting the “Contrast” and “Gamma” settings to 10.00 and 2.00 respectively.

Figure 5.17, illustrates the ignition probability of each equivalence ratio tested and the number of ignition tests conducted for each equivalence ratio. Ignition was not observed in the main chamber for equivalence ratios leaner than 0.4 and richer than 2.4. Ignition test data for Figure 5.17 does not includes the tests in which ignition initiated from diaphragm debris. The ethylene-air mixture test with equivalence ratios 0.4 to 2.0 all ignited but the lower probability indicated in Figure 5.17 was due to diaphragm ignition tests being filtered out. The torch jet tests where ignition was detected was

plotted with ignition delay time vs main chamber ethylene equivalence ratio in Figure 5.18.

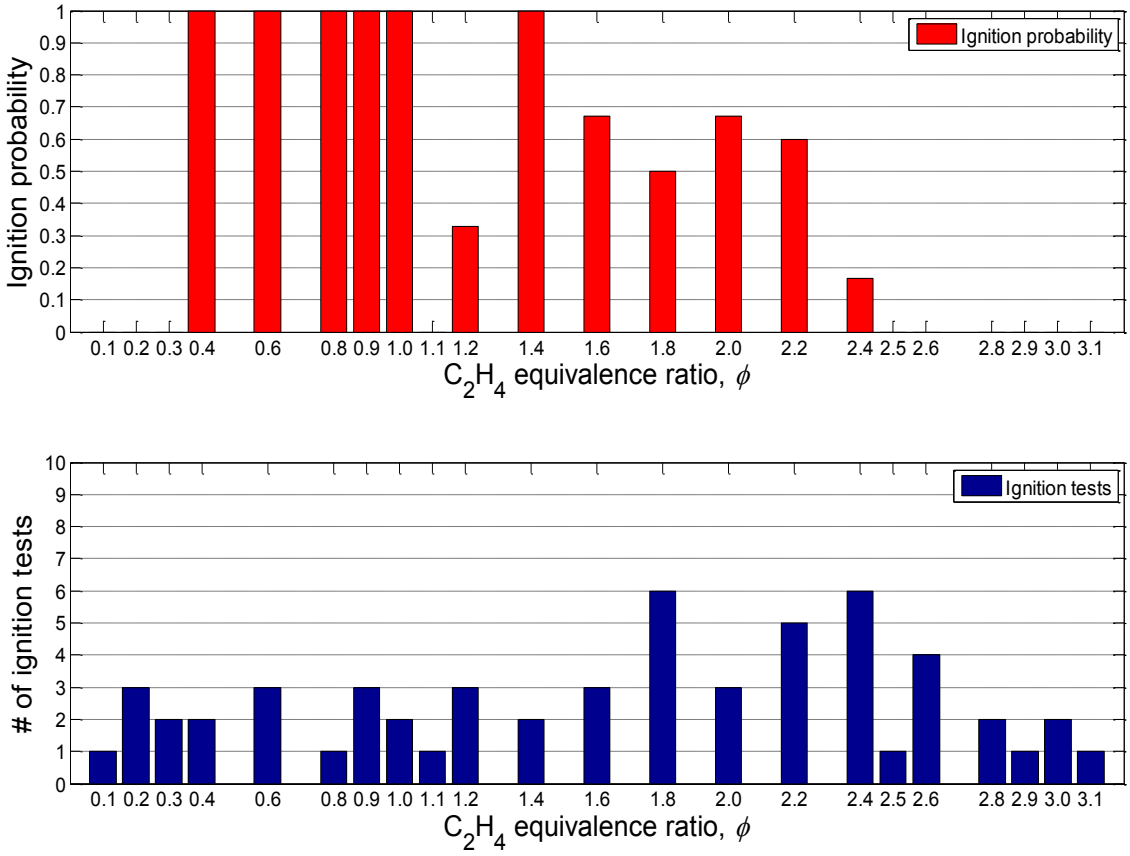

Figure 5.17 Ignition of ethylene experiments: (top) Ignition probability of equivalence ratios, (bottom) Number of tests conducted for each equivalence ratio

Figure 5.18, indicates the experimental delay time obtained from assessing the diaphragm rupture time (Section 3.3) and the ignition detection time (Section 3.6) for each ethylene experiment. Figure 5.18 also show the 4th order polynomial curve fit used to fit the observed ignition delay time data. The minimum ignition delay time was observed for lean ethylene-air equivalence ratios of 0.6 and 0.8. The ignition delay time increased around this local minimum values on both increasing and decreasing sides of equivalence ratio until the lean limit and the rich limit ethylene-air equivalence ratios as explained above.

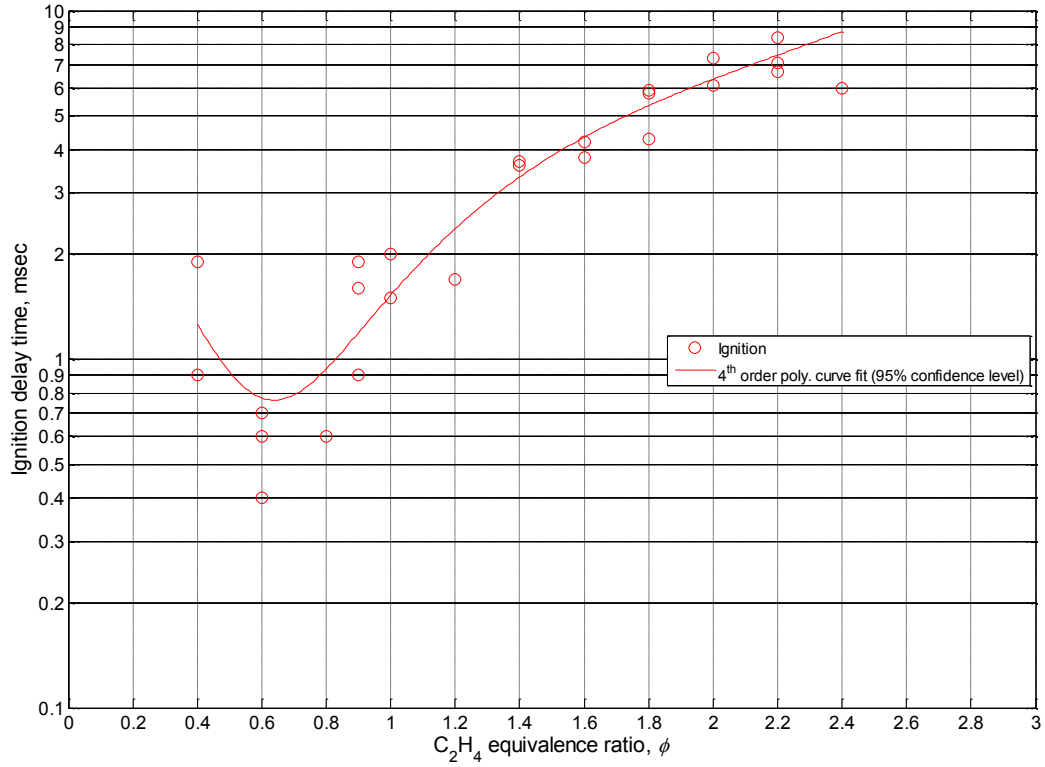

Figure 5.18 Ignition delay of different equivalence ratios of ethylene mixtures

5.6. Propane Experiments

Propane-air mixture experiments were conducted similarly to the ethylene-air experiments. The lean-limit and the rich-limit propane-air equivalence ratios were identified with the same combustion torch jet that was used for ethylene-air experiments explained in Section 5.1. The pre-chamber initial conditions were set the same as per the pre-chamber settings for ethylene-air experiments. The main chamber initial pressure and initial temperature were maintained at atmospheric pressure and room temperature as per the ethylene experiments described in Section 5.1. The main chamber was fueled using propane instead of ethylene. Figure 5.19 indicates the summary of the propane-air ignition limit equivalence ratios.

A total of 41 tests were conducted with propane-air mixtures in the main chamber. No ignition was observed in the main chamber for 10 tests, with 22 experiments igniting

with the combustion torch jet. There were 9 experiments where the ignition in the main chamber was defined as initiated by diaphragm debris. The ignition tests on Figure 5.19, illustrates only combustion torch jet ignition. The figure shows the ignition probability of a propane-air mixture equivalence ratio that were ignited by the torch jet and the number of tests done for each propane-air mixture equivalence ratio.

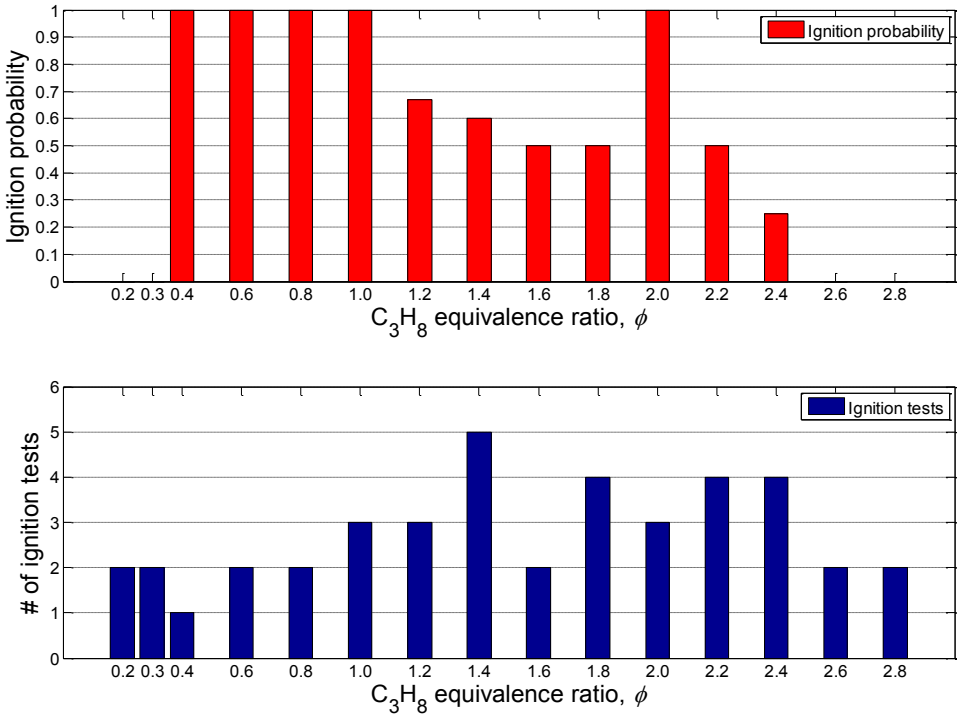

Figure 5.19 Ignition of propane experiments: (top) Ignition probability of equivalence ratios, (bottom) Number of tests conducted for each equivalence ratio

The lean limit and the rich limit equivalence ratio ignitable by the torch jet appear to be similar to equivalence ratio range for ethylene-air mixture. Ignition in the main chamber was not observed for propane-air equivalence ratios below 0.4 and propane rich equivalence ratios over 2.4. The equivalence ratios between 0.4 to 2.2 had an ignition probability of 100% which included ignition detected associated with diaphragm debris.

The ignition delay time was evaluated from the calculated diaphragm rupture time and ignition determined by image processing the high-speed video images. Figure 5.20 show the variation of the ignition delay time for different propane-air equivalence ratios.

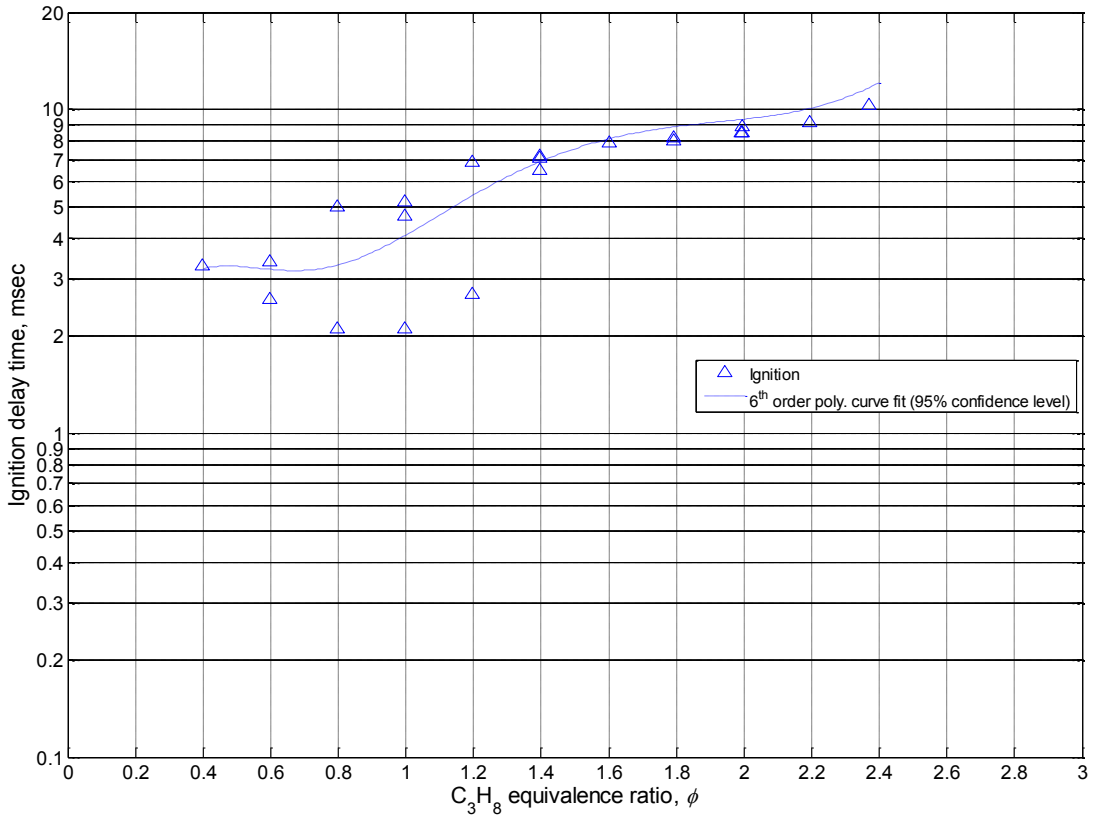

Figure 5.20 Ignition delay of different equivalence ratios of propane mixtures

The minimum ignition delay was observed at near-stoichiometric mixtures to the propane lean side. The ignition delay time increased on either side of this minimum ignition delay time equivalence ratio as the equivalence ratio was varied. An interesting feature was observed for these propane experiments where there appeared to be two distinct sets of ignition delay times for the same equivalence ratio for equivalence ratios from 0.6 to 1.2. The higher of the ignition delay times for these equivalence ratios appearing to the have a linear variation across the ignitable equivalence ratio range when the ignition delay times are plotted on a semi-log scale as can be seen in Figure 5.20.

The difference in the main chamber ignition of two identical tests at propane-air equivalence ratio of 1.0 are illustrated in Figure 5.21. The high-speed video was recorded at 10,000 fps in both tests. The torch jet was visible in the low ignition delay time test on the left and was not visible in the high ignition delay time test on the right.

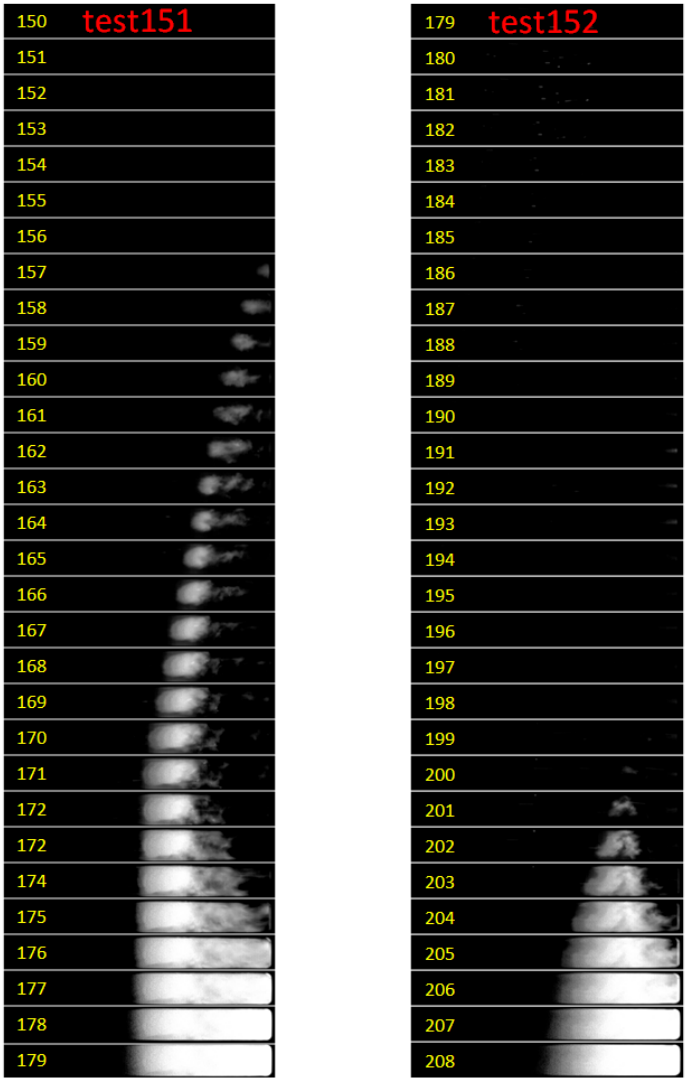

Figure 5.21 High-speed video images from propane mixtures with ϕ = 1.0

The torch jet plume was clearly visible until subsequent ignition in the main chamber. The high ignition delay test on the right was not visible until the mixture

temperature increase and ignition occurs in the mixing region of the channel. This was observed at all equivalence ratios where two separate ignition delay times was observed.

5.7. Methane Experiments

Methane experiments were conducted to find the effect on ignition delay time when the main chamber methane-air equivalence ratio is varied, with a constant pre-chamber torch jet. The torch jet was made of an ethylene-air mixture at an equivalence ratio of 1.1 similar to both ethylene and propane tests described before in Sections 5.5 and 5.6. The methane-air equivalence ratio was varied from 0.2 to 3.0 in the main chamber for these experiments. The diaphragm failed to rupture 3 times in the desired manner out of 49 tests. These 3 aluminum diaphragms were not ruptured into 4 symmetric petals. There were 19 experiments where there was no ignition in the main chamber. While 4 tests indicated having the diaphragm debris interact with the ignition, 18 tests ignited with the combustion torch jet.

The lean methane ignitable equivalence ratio was found to be 0.4 and the rich methane ignitable equivalence was 1.4. Methane had the smallest ignitable equivalence ratio range from the fuels tested in the study. Methane mixtures of equivalence ratios leaner than 0.4 and richer than 1.4 were not ignitable by the ethylene torch jet. Figure 5.22 illustrates the ignition probability of the equivalence ratios tested and the number of tests conducted for each equivalence ratio. The diaphragm debris ignition tests were filtered out from these figures. The lower ignition probability at methane equivalence ratio of 1.2 is due to this filtering.

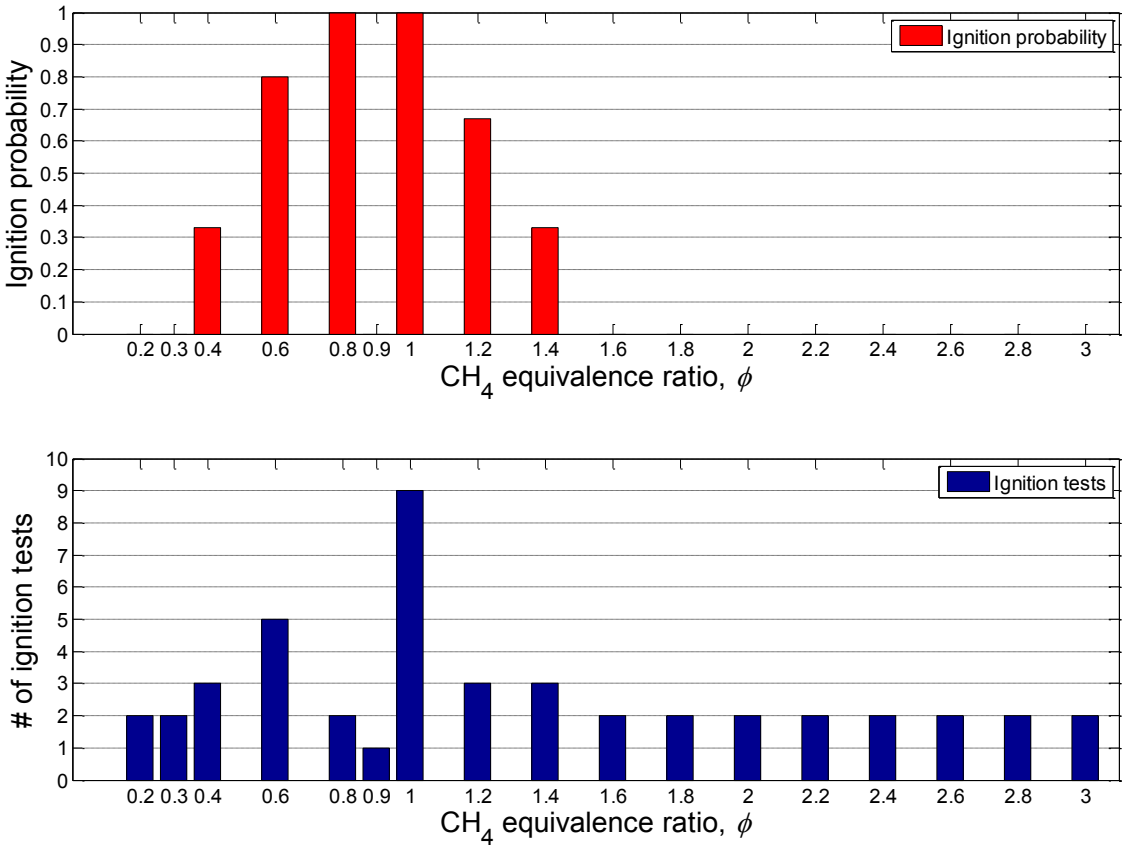

Figure 5.22 Ignition of methane experiments: (top) Ignition probability of equivalence ratios, (bottom) Number of tests conducted for each equivalence ratio

Figure 5.23, shows the ignition delay time for the different methane-air mixture equivalence ratios. A quadratic curve fit was used to represent the ignition delay time variation. Similar to propane-air mixture ignition observations there appeared to be two distinct sets of high and low ignition delay times for equivalence ratios from 0.6 to 1.0.

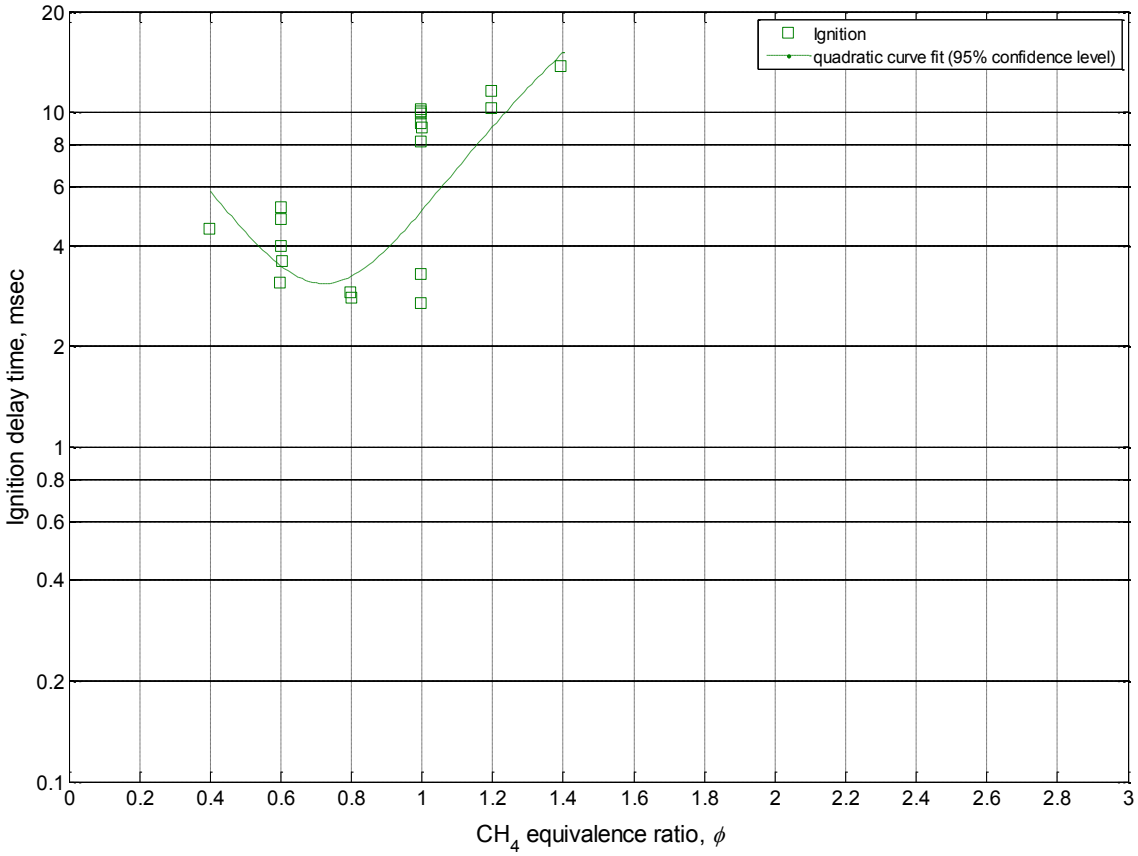

Figure 5.23 Ignition delay of different equivalence ratios of methane mixtures

The variation of the ignition delay time from high-speed video images for methane-air main chamber equivalence ratio at 1.0 are illustrated in Figure 5.24. The high-speed video was captured at 10,000 fps as for all other tests. Test 230 is a high ignition delay time test and the tests 231 and 234 are low ignition delay time tests. The torch jet was visible from initial penetration until ignition in the main chamber in the low ignition delay time. The high ignition delay time test only became visible after the mixing region in the main chamber reached a critical temperature which then intensified and increased in size until ignition.

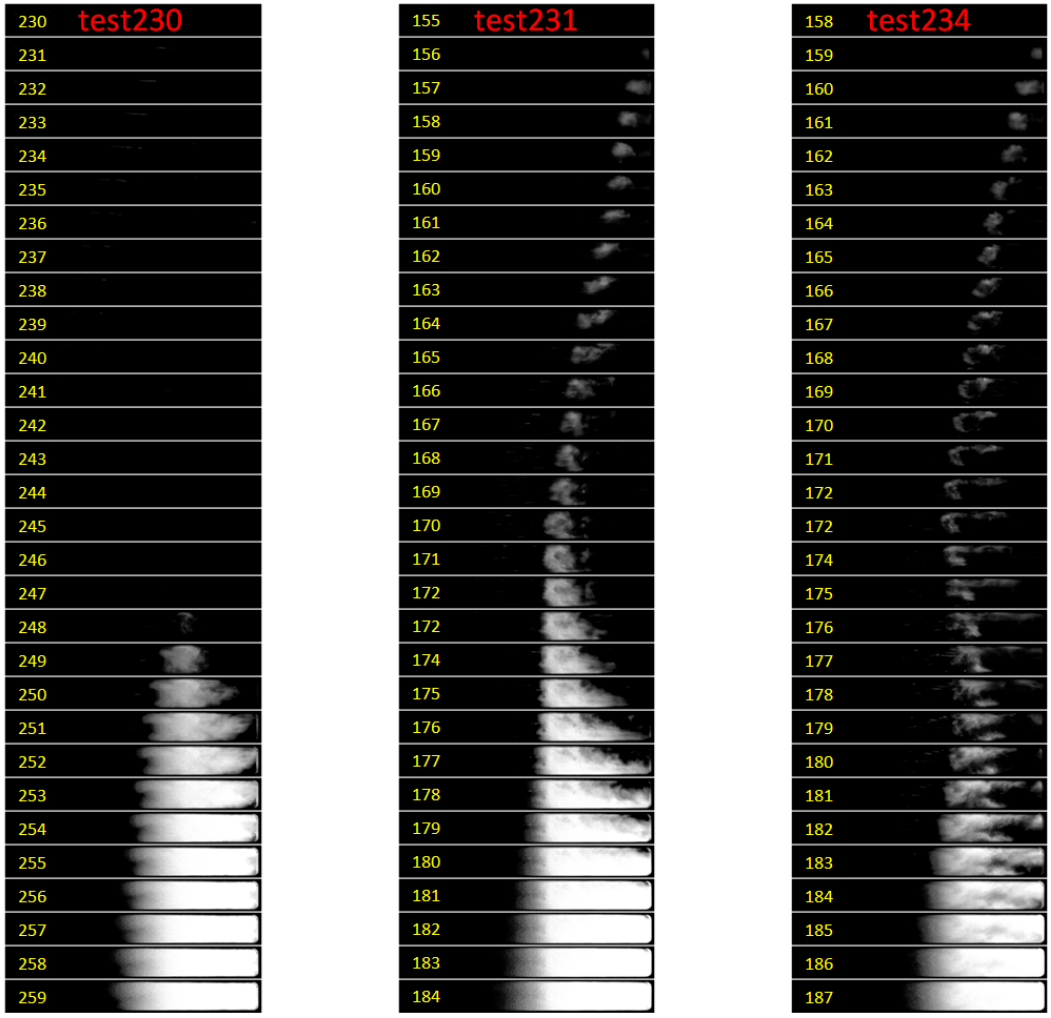

Figure 5.24 High-speed video images from methane mixtures with ϕ = 1.0

The research in the area of radical activated ignition [17-25] results matched with the lean ignition limits observed for both methane and propane in the current study. This lean ignition limit was about ϕ = 0.4 for both the fuels, for the combustion torch jet produced in the pre-chamber.

CHAPTER 6. CONCLUSIONS AND RECOMMENDATIONS

This chapter includes both the concluding remarks of the conducted experimental study and recommendations for future work.

6.1. Conclusions

The experimental study was prepared and conducted to evaluate the ignition of methane, ethylene, and propane using hot combustion torch jet. Fuel-lean mixture and fuel-rich mixture ignition limit equivalence ratios of fuel-air mixtures were identified for all three fuels. The fuel-lean ignition limits found in the current study for methane and propane were similar to the lean methane-air and lean propane-air mixture ignition using radical laden gas jets generated in pre-chambers [17-25]. These equivalence ratios were well below the lean mixture equivalence ratios that are ignitable by conventional spark plugs.

The effect of the jet characteristics on ignition delay times in the main-chamber ethylene-air mixtures was observed with both sonic and super-sonic nozzles in the pre-chamber. Nozzles with exit diameters of above a critical value ignited, while the surface area of the nozzle cavity and the geometric-shape of the nozzle were both influential in the main chamber combustible mixture ignition. Nozzle # 1 was selected for the main study based on these experiments.

The effect of different pre-chamber conditions on main chamber fuel-air mixture ignition was tested varying the ethylene-air equivalence ratio in the pre-chamber. The lowest ignition delay time for varying pre-chamber equivalence ratios were achieved at

slightly ethylene-rich pre-chamber mixtures ranging from 1.1 to 1.3. The slightly richer ethylene 1.1 equivalence ratio was selected to produce the torch jet in the pre-chamber.

The ignition delay times for the range of ignitable fuel-air equivalence ratios were experimentally determined for a slightly rich ethylene-air torch jet. All fuels indicated a shorter ignition delay time for lean equivalence ratios compared to the fuel-rich equivalence ratios. Lean mixtures of methane-air and propane-air mixtures that are near-stoichiometric, indicated the lowest ignition delay time in these specific fuels. Ethylene lean mixtures in the range 0.6 to 0.8 had the smallest ignition delay times from the fuel-air mixtures tested.

6.2. Future Recommendations

The following section describes work that can be undertaken to further analyze and address limitations and shortcomings of the current study.

1. To have a good understanding of the time available for combusting the channel contents in a wave rotor combustor, the ignition and the flame propagation in the channels have to be observed. The jet characteristics are different in the transient stationary torch jet studied under the present work, when compared with the transient translating torch jet [52]. The mixing and ignitability of the fuel-air mixture in the wave rotor combustor channels vary due to the difference in the translating jet as compared to the stationary jet [53]. Therefore, the ignition delay characteristics should be investigated for the relative motion between the torch igniter and the channel. In addition to this, the flame propagation speeds need to be investigated to understand the time scales associated with complete combustion of the combustible mixture residing in the length of the channel.

2. The fluid flow phenomena that occur when a transient jet injects into a confined volume, is an underlying effect in the study of wave rotor combustor ignited by torch jet. The single channel wave rotor combustion rig and the experimental setup used for

this study, does not have the capability of visualizing the flow phenomena in the channel This limitation associated with the main chamber led to the redesign of the main chamber in the current single-channel wave rotor combustion rig. The main chamber was redesigned with two viewing windows offering optical access through the main chamber to be incorporated with a visualization technique known as the schlieren imaging technique [54]. The redesigned main chamber design drawings are attached as Appendix I. In addition to this, the main chamber was redesigned with a new sealing mechanism instead of the latex diaphragm assembly used in the current rig used for fueling the main chamber. A simpler version of this sealing mechanism was tested successfully on the current rig with fueling and stationary ignition in the pre-chamber. The testing with the redesigned main chamber with schlieren optical method would shed light on fluid motion, ignition event, ignition location, flame propagation, and fluid-flame interaction in the main chamber. This would enable the use of high-speed video images to identify ignition in the main chamber with less ambiguity compared with the current study.

3. The ignition of the main chamber combustible mixture by aluminum diaphragm debris is another aspect that needs further investigation. The possibility of eliminating the generation of this debris would mean that a modification or a redesign of the pre-chamber is required, or an alternative diaphragm material is required to be investigated. The use of Mylar® polyester (PET) films did not have the intended effect since they melted due to the heat in the pre-chamber.

4. The ignition delay time definition in the current study used the rupture of the aluminum diaphragm as the trigger event. Since the diaphragm was at the inlet side of the nozzle insert the torch jet has to travel approximately 1 inch along the nozzle to enter the main chamber. The modification of the nozzle insert assembly with the diaphragm at the exit side could provide a better trigger for the ignition delay time.

5. The current study used a numerical method for determining the rupture time of the aluminum diaphragm. This numerical method was validated using high-speed video

images, where the deviation between the numerical method and the high-speed video images was 130±116 μs. Alternate physical measurement of the diaphragm rupture time would provide better ignition delay time assessments.

6. The ignition in the main chamber from the pre-chamber combustion torch jet was identified with the use of luminosity emitted by the combustion. The current study observed limitations of detecting the luminosity at both lean limit and rich limit equivalence ratios, The pressure transducer data for these limit equivalence ratios indicated pressure fluctuations above the pressure variations recorded in tests when the main chamber was filled with atmospheric air (ϕ = 0). An ignition classification dependant on more than emitted luminosity from the main chamber might be suited for future work.

7. The use of absolute pressure transducers instead of the 113A32 dynamic pressure transducers used in the present study would provide precise pressure readings inside both the pre-chamber and the main chamber.

LIST OF REFERENCES

LIST OF REFERENCES

[1] Akbari, P., and Nalim, M. R., "Review of Recent Developments in Wave Rotor Combustion Technology," *Journal of Propulsion and Power*, Vol. 25, No. 4, 2009, pp. 833-844.

[2] Nalim, M. R., "Longitudinally Stratified Combustion in Wave Rotors," *Journal of Propulsion and Power*, Vol. 16, No. 6, 2000, pp. 1060-1068.

[3] Weber, R., "A Pressure-Wave Machine with Integrated Constant Volume Combustion," *Swiss Energy Research Report 1977-1997*, National foundation of Energy Research, Switzerland, Project No. 426, 1997, pp. 142-153.

[4] Akbari, P., Nalim, M. R., and Snyder, P. H., "Numerical Simulation and Design of a Combustion Wave Rotor for Deflagrative and Detonative Propagation," AIAA paper 2006-5134, 2006.

[5] Nalim, M. R., and Paxon, D. E., "A Numerical Investigation of Premixed Combustion in Wave Rotors," *Journal of Engineering for Gas Turbines and Power*, Vol. 119, No. 3, 1997, pp. 668-675.

[6] Nalim, M. R., "Assessment of Combustion Modes for Internal Combustion Wave Rotors," *Journal of Engineering for Gas Turbines and Power*, Vol. 121, No. 2, 1999, pp. 265-271.

[7] Snyder, P. H., Alparslan, B., and Nalim, M. R., "Gas Dynamic Analysis of the Constant Volume Combustor, A Novel Detonation Cycle," AIAA paper 2002-4069, 2002.

[8] Würmel, J., Silke, E. J., Curran, H. J., Ó Conaire, M.S., and Simmie, J. M., "The Effects of Diluent Gases on Ignition Delay Times in the Shock Tube and in the Rapid Compression Machine," *Combustion and Flame*, Vol. 151, No. 1-2, 2007, pp. 289-302.

[9] Wolfhard, H. G., "The Ignition of Combustible Mixtures by Hot Gases," *Jet Propulsion*, Vol. 28, No. 12, December 1958, pp. 798-804

[10] Van Dolah, R. W., Zabetakis, M. G., Burrgess, D. S., and Scott, G. S., "Ignition or the Flame-Initiation Process," *Fire Technology*, Vol. 1, No. 1, 1965, pp. 32-42.

[11] Vanpée, M., and Wolfhard, H. G., "Comparison between Hot Gas Ignition and Limit Flame Temperatures," *ARS Journal*, Vol. 29, No. 7, 1959, pp. 517-519.

[12] Bruszak, A. E., Burgess, D., and Wijnen, M. H., "Reaction Kinetics in Hot-gas Ignition of Ethane-Air," *Combustion and Flame*, Vol. 7, 1963, pp. 245-251.

[13] Fink, Z. J., and Vanpée, M., "Overall Kinetics of Hot Gas Ignition," *Combustion Science and Technology*, Vol. 11, No. 5-6, 1975, pp. 229-238.

[14] Cato, R. J., and Kuchta, J. M., "Hot Gas Ignition Temperatures of Hydrocarbon Fuel Vapor-Air Mixtures," Bureau of Mines, AD0643518, 1966.

[15] Simmons, R. F., and Wolfhard, H. G., "Some Limiting Oxygen Concentrations for Diffusion Flame in Air Diluted with Nitrogen," *Combustion and Flame*, Vol. 1, No. 2, 1957, pp. 155-161.

[16] Westbrook, C. K., and Dryer, F. L., "Chemical Kinetic Modeling of Hydrocarbon Combustion," *Progress in Energy and Combustion Science*, Vol. 10. No. 1, 1984, pp. 1-57.

[17] Gussak, L. A., "High Chemical Activity of Incomplete Combustion Products and a Method of Prechamber Torch Ignition for Avalanche Activation of Combustion in Internal Combustion Engines," SAE Technical Paper 750890,1975.

[18] Oppenheim, A. K., Teichman, K., Hom, K., and Stewart, H. E., "Jet Ignition of an Ultra-Lean Mixture," SAE Technical Paper 780637, 1978.

[19] Murase, E., Ono, S., Hanada, K., and Oppenheim, A. K., "Pulsed Combustion Jet Ignition in Lean Mixtures," SAE Technical Paper 942048, 1994.

[20] Murase, E., Hanada, K., Yun, J. H., and Oppenheim, A. K., "Radical Emission and Fluorescence Measurements in Pulsed Flame Jet," *4th international Symposium on Diagnostics and Modeling of Combustion in Internal Combustion Engines (COMODIA)*, Kyoto, Japan, July 20-23, 1998, pp. 399-404.

[21] Wallesten, J., and Chomiak, J., "Investigation of Spark Position Effects in a Small Pre-Chamber on Ignition and Early Flame Propagation," SAE Technical Paper 2000-01-2839, 2000.

[22] Valle, R. M., Cândido de Sá, D. C., and Ramalho Filho, F. A., "Constructive Parameters Analysis of combustion Pre-Chamber Adapted in Torch-Ignition System of Otto Cycle Engine," SAE Technical Paper 2003-01-3713, 2003.

[23] Toulson, E., Watson, H. C., and Attard, W. P., "Gas Assisted Jet Ignition of Ultra-Lean LPG in a Spark Ignition Engine," SAE Technical Paper 2009-01-0506, 2009.

[24] Toulson, E., Watson, H. C., and Attard, W. P., "Modeling Alternative Prechamber Fuels in Jet Assisted Ignition of Gasoline and LPG," SAE Technical Paper 2009-01-0721, 2009.

[25] Attard, W. P., Fraser, N., Parsons, P., and Toulson, E., "A Turbulent Jet Ignition Pre-Chamber Combustion System for Large Fuel Economy Improvements in a Modern Vehicle Powertrain," SAE Technical Paper 2010-01-1457, 2010.

[26] Yamaguchi, S., Ohiwa, N., and Hasegawa, T., "Ignition and Burning in a Divided Chamber Bomb," *Combustion and Flame*, Vol. 59, 1985, pp. 177-187.

[27] Tarzhanov, V. I., Telichko, I. V., Vil'danov, V. G., Sdobnov, V. I., Makarov, A. E., Mukhin, S. L., Koretskii, I. G., Ogarkov, V. A., Vlasov, V. V., Zinchenko, A. D., Vorob'ev, A. V., Grachev, A. N., Matkin, V. A., and Potashnikov, V. A., "Detonation of Propane-Air Mixtures under Injection of Hot Detonation Products," *Combustion, Explosion and Shock Waves*, Vol. 42, No. 3, 2006, pp. 336-345.

[28] Mayinger, F., Jordan, M., Eder, A., Zaslonko, I.S., karpov, V. P., and Frolov, S. M., "Flame-Jet Ignition of fuel-Air Mixtures. Experimental Findings and Modeling," *17th International Colloquium on the Dynamics of Explosions and Reactive Systems (ICDERS)*, Heidelberg, Germany, July 25-30, 1999.

[29] Bilgin, M., Keller, J. J., and Breidenthal, R. E., "Ignition and Flame Propagation with Rotating Hot jets In a Simulated Wave Engine Test Cell," AIAA Paper 98-3399, 1998.

[30] Bilgin, M., "Stationary and Rotating Hot Jet Ignition and Flame Propagation In a Premixed Cell," Ph.D. Dissertation, Aeronautics and Astronautics Dept., University of Washington, Seattle, WA, 1998.

[31] Baronia, D., Nalim, M. R., and Akbari, P., "Numerical Study of Wave Rotor Ignition and Flame Propagation in a Single-Channel Rig," AIAA Paper 2007-5054, 2007.

[32] Baronia, D., "Numerical Analysis of Hot Jet Injection and Premixed Flame Propagation in a Channel," Thesis, Mechanical Engineering Dept., Indiana University-Purdue University, Indianapolis (IUPUI), Indianapolis, IN, 2006.

[33] Wilson, J., "An Experimental Determination of Losses in a Three-Port Wave Rotor," *Journal of Engineering for Gas Turbines and Power*, Vol. 120, No. 4, 1998, pp. 833-842.

[34] Wilson, J., Welch, G. E., and Paxon, D. E., "Experimental Results of Performance Test on a Four-Port Wave Rotor," AIAA Paper 2007-1250, 2007.

[35] Li, D., "Thermal Image Analysis using Calibrated Video Imaging," Ph.D. Dissertation, Computer Science Dept., University of Missouri, Columbia, MO, 2006.

[36] Walton, S. M., He, X., Zigler, B. T., and Wooldridge, M. S., "An Experimental Investigation of the Ignition Properties of Hydrogen and Carbon Monoxide mixtures for Syngas Turbine Applications," *Proceedings of the Combustion Institute*, Vol. 31, No. 2, 2007, pp. 3147-3154.

[37] Wójcik, W., and Kotyra, A., "Combustion Diagnosis by Image Processing," *Photonics Letters of Poland*, Vol. 1, No. 1, 2009, pp. 40-42.

[38] Lifshitz, A., "Chemical Reactions in Shock Waves and Detonations," *Handbook of Shock Waves*, Academic Press, New York, 2001, Chap. 16.5.

[39] Baker, J. A., and Skinner, G. B., "Shock-Tube Studies on the Ignition of Ethylene-Oxygen-Argon Mixtures," *Combustion and Flame*, Vol. 19, No. 3, December 1972, pp. 347-350.

[40] Bhaskaran, K. A., and Srinivasa, C., "Shock Tube Study of High Temperature Ethylene-Oxygen Reaction," *Proceedings of the Fourth National Conference on I.C. Engines and Combustion*, 1977, pp. c2-23-c2-27.

[41] Hidaka, Y., Kataoka, T., and Suga, M., "A Shock-Tube Investigation of Ignition in Ethylene-Oxygen-Argon Mixtures," *Bulletin of the Chemical Society of Japan*, Vol. 47, No. 9, 1974, pp. 2166-2170.

[42] Drummond, L. J., "Shock-Initiated Exothermic Reactions," *Australian Journal of Chemistry*, Vol. 21, No. 11, 1968, pp. 2641-2648.

[43] Brown, C. J., and Thomas, G. O., "Experimental Studies of Shock-Induced Ignition and Transition to Detonation in Ethylene and Propane Mixtures," *Combustion and Flame*, Vol. 117, No. 4, 1999, pp. 861-870.

[44] Skinner, G. B., Lifshitz, A., Scheller, K., and Burcat, A., "Kinetics of Methane Oxidation," *Journal of Chemical Physics*, Vol. 56, No. 8, 1972, pp. 3853-3861.

[45] Burcat, A., Lifshitz, A., Scheller, K., and Skinner, G. B., "Shock-Tube Investigation of Ignition in Propane-Oxygen-Argon Mixtures," *13th Symposium (International) on Combustion*, Vol. 13, No. 1, 1971, pp. 745-755.

[46] Burcat, A., Scheller, K., and Lifshitz, A., "Shock-Tube Investigation of Comparative Ignition Delay Times for C_1-C_5 Alkanes," *Combustion and Flame*, Vol. 16, No. 1. 1971, pp. 29-33.

[47] Myers, B. F., and Bartle, E. R., "Reaction and Ignition Delay Times in the Oxidation of Propane," *AIAA Journal*, Vol. 7, No. 10, 1969, pp. 1862-1869.

[48] Baukal, C. E., "Heat Transfer Modes," *Heat Transfer in Industrial Combustion*, CRC press, Florida, 2000, pp. 65-109.

[49] Grosshandler, W. L., "RADCAL: A Narrow-Band Model for Radiation Calculations in a Combustion Environment," NIST Technical Note 1402, NIST TN 1402, Springfield, VA, April 1993.

[50] Westbrook, C. K., and Dryer, F. L., "Chemical Kinetics Modeling of Hydrocarbon Combustion," *Progress in Energy and Combustion Science*, Vol. 10, No. 1, 1984, pp. 1-57.

[51] Turns, S. R., "Some Important Chemical Mechanisms," *An Introduction to Combustion: Concepts and Applications*, 2nd ed., McGraw-Hill, 2000.

[52] Wijeyakulasuriya, S. D., and Nalim, M. R., "Transient Translating Gas Jets in Confined Channels," *45th AIAA/ASME/SAE/ASEE Joint Propulsion Conference & Exhibit,* Denver, CO, 2009.

[53] Wijeyakulasuriya, S. D., Perera, I. U., and Nalim, M. R., "Mixing and Ignition Potential of Transient Confined Turbulent Jet in a Wave-Rotor Constant-Volume Combustor," *46th AIAA/ASME/SAE/ASEE Joint Propulsion Conference & Exhibit,* Nashville, TN, 2010.

[54] Settles, G. S., *Schlieren and Shadowgraph Techniques: Visualization Phenomena in a Transparent Media*, Springer-Verlag, New York, 2001.

APPENDICES

Appendix A Pre-Chamber and Main Chamber Design Drawings

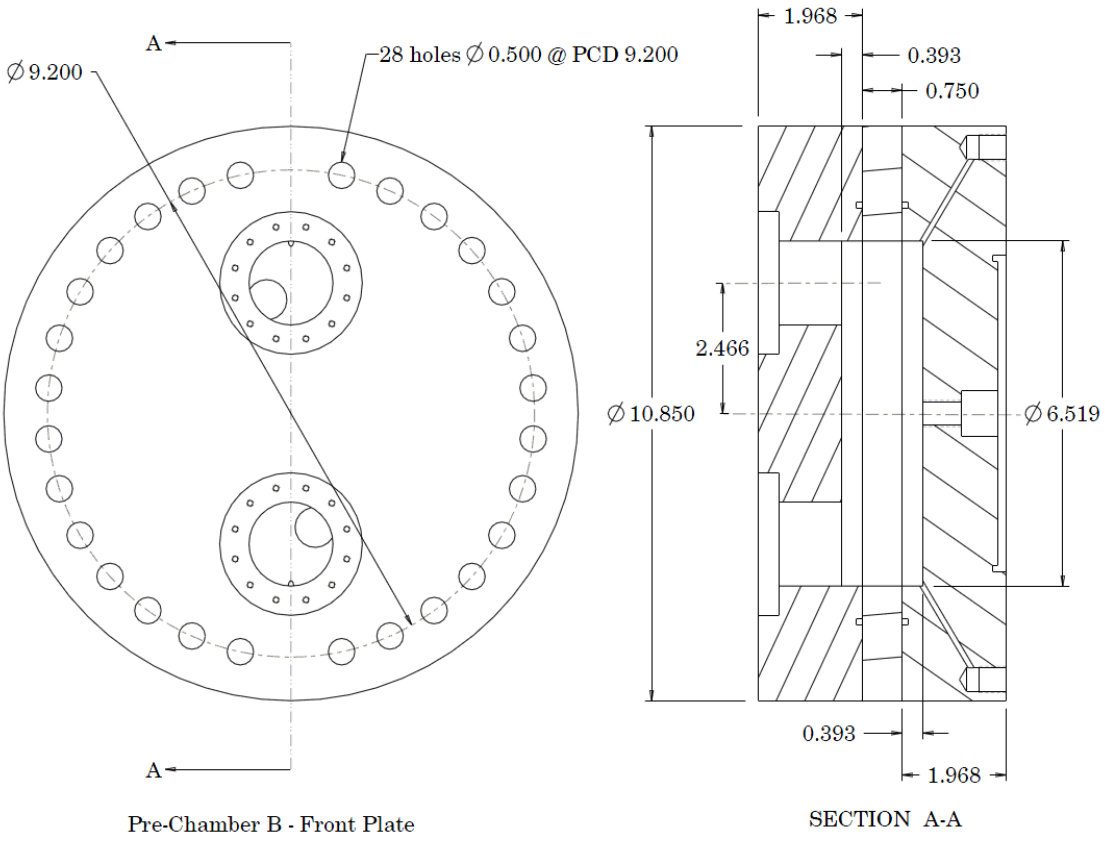

Figure A.1 Pre-chamber dimensions

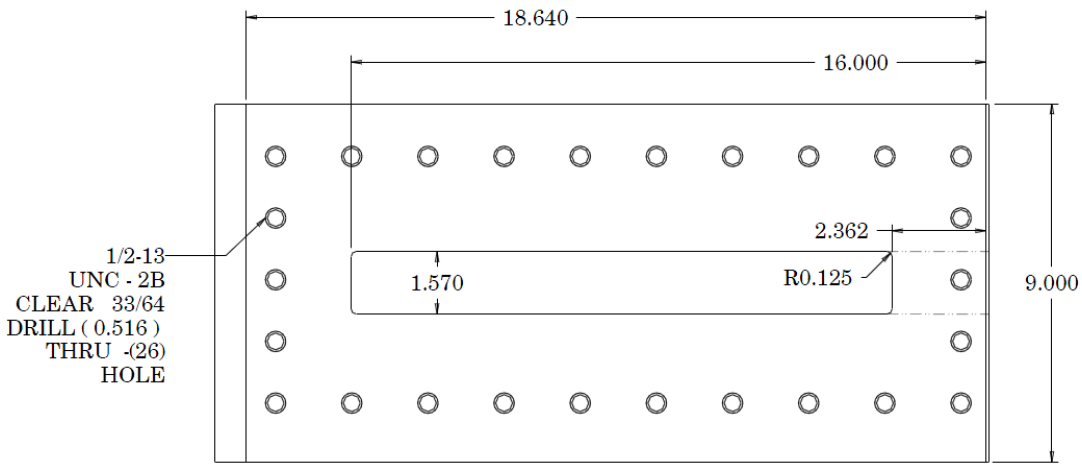

Figure A.2 Main chamber dimensions

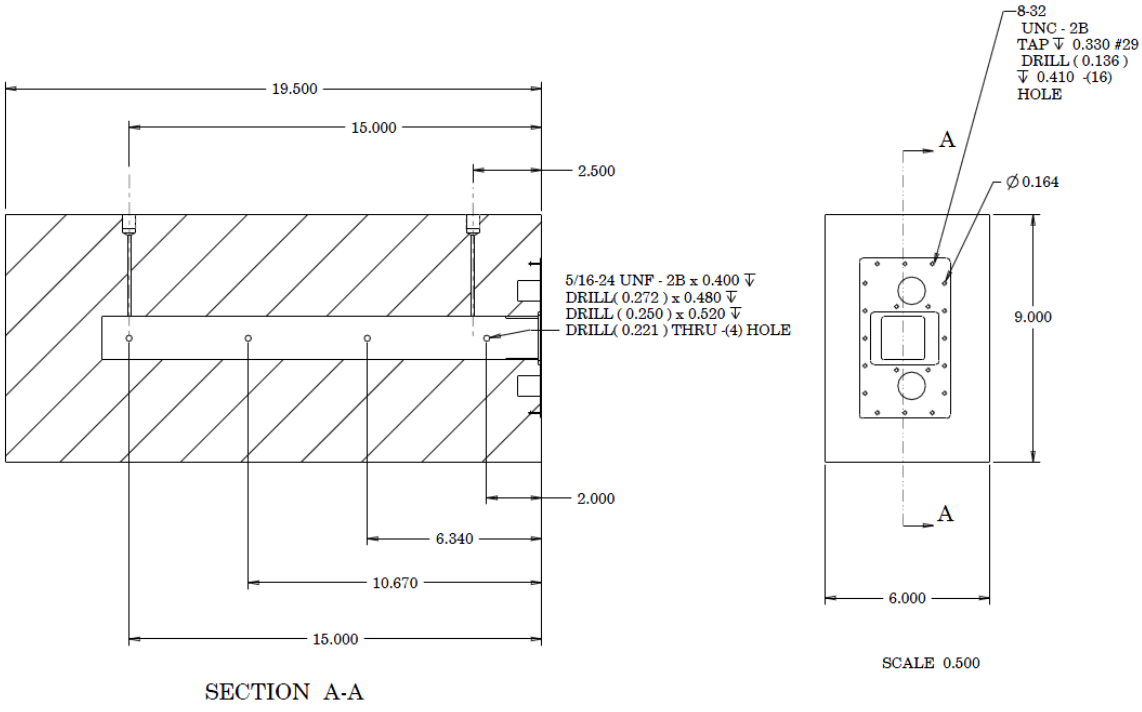

Figure A.3 Main chamber pressure transducer locations

Appendix B Nozzle Dimensions

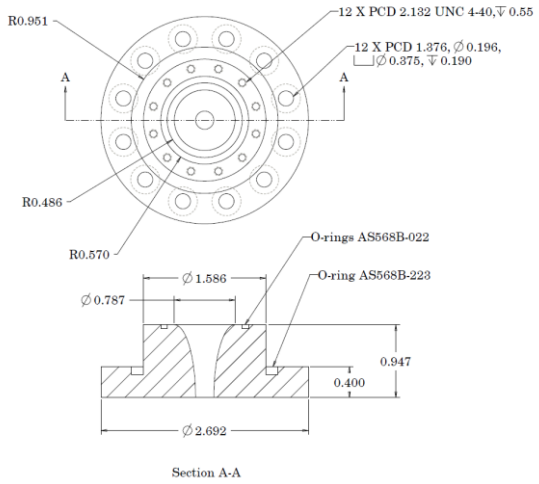

Figure B.1 Nozzle basic dimensions

Nozzle # 1

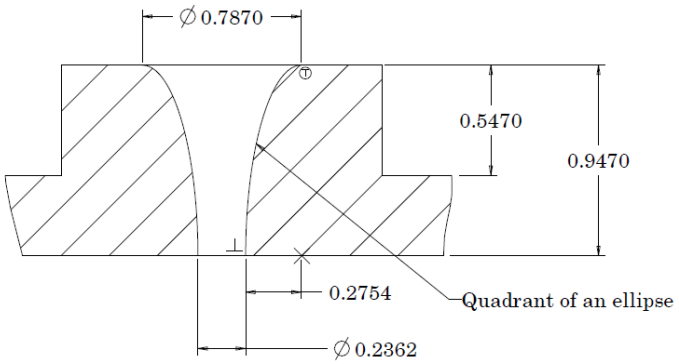

Figure B.2 Nozzle # 1

Nozzle # 2

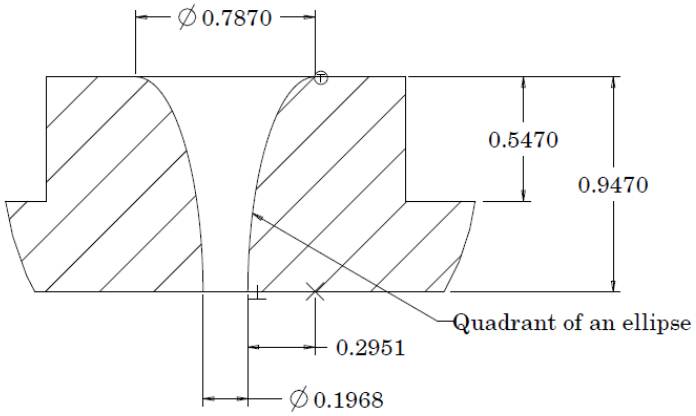

Figure B.3 Nozzle # 2

Nozzle # 3

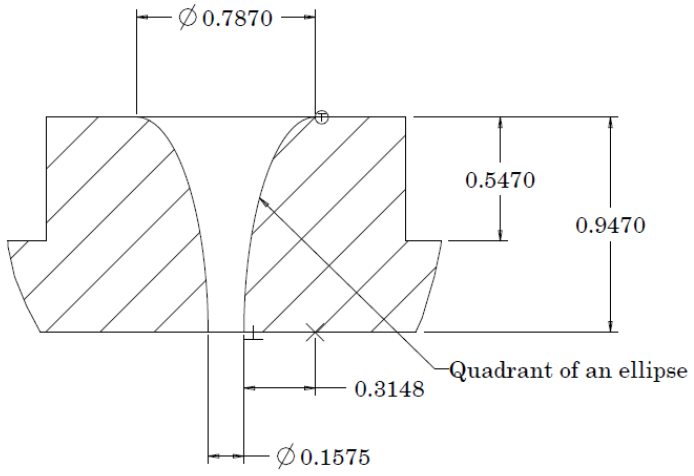

Figure B.4 Nozzle # 3

Nozzle # 4

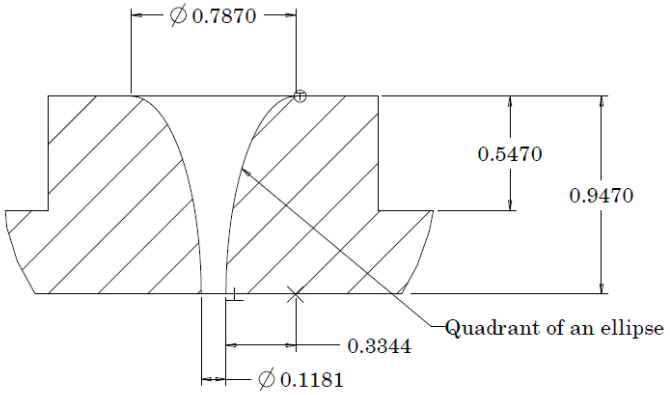

Figure B.5 Nozzle # 4

Nozzle # 5

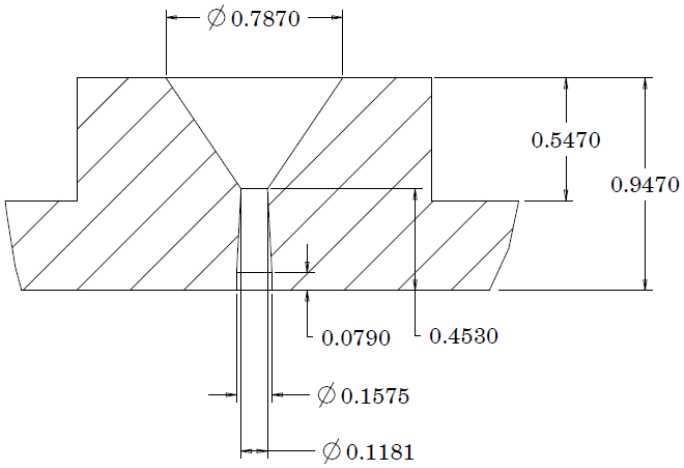

Figure B.6 Nozzle # 5

Nozzle # 6

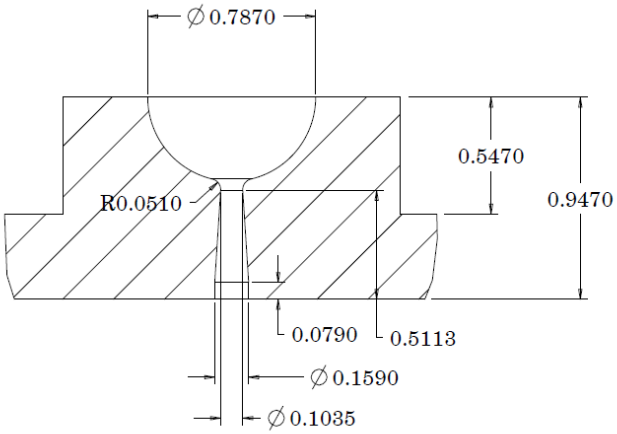

Figure B.7 Nozzle # 6

Nozzle # 7

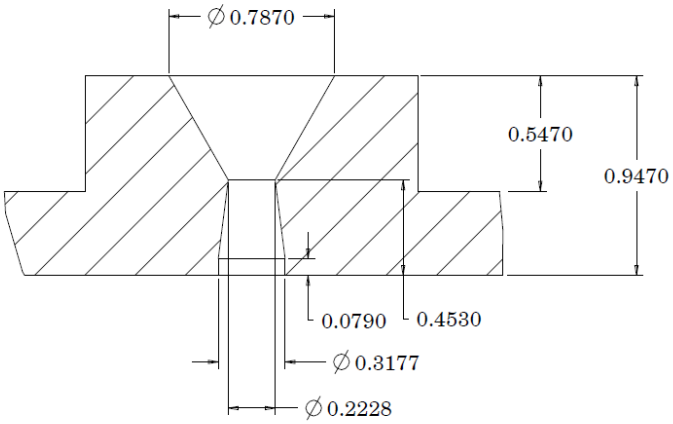

Figure B.8 Nozzle # 7

Appendix C Ignition Trigger Synchronizing Circuit Output

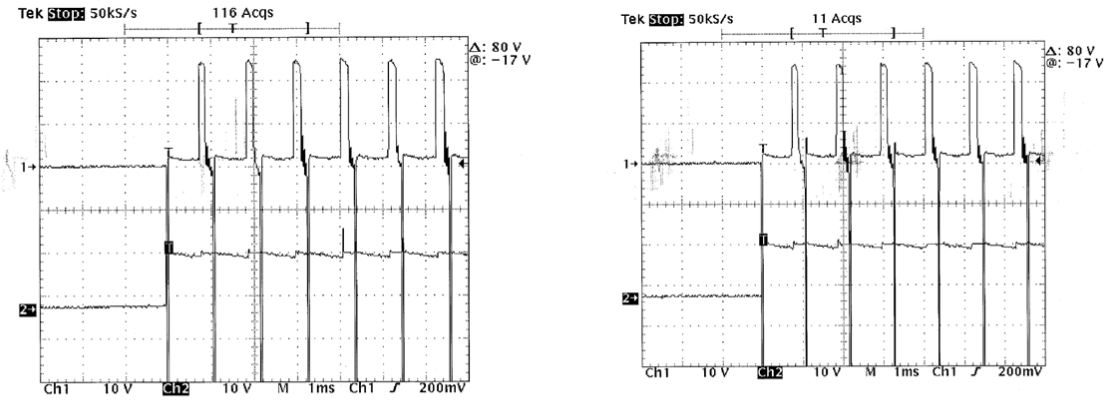

1 - signal from ignition circuit
2 - triggering voltage to the igniton circuit

Figure C.1 Ignition trigger and voltage variation in the ignition circuit

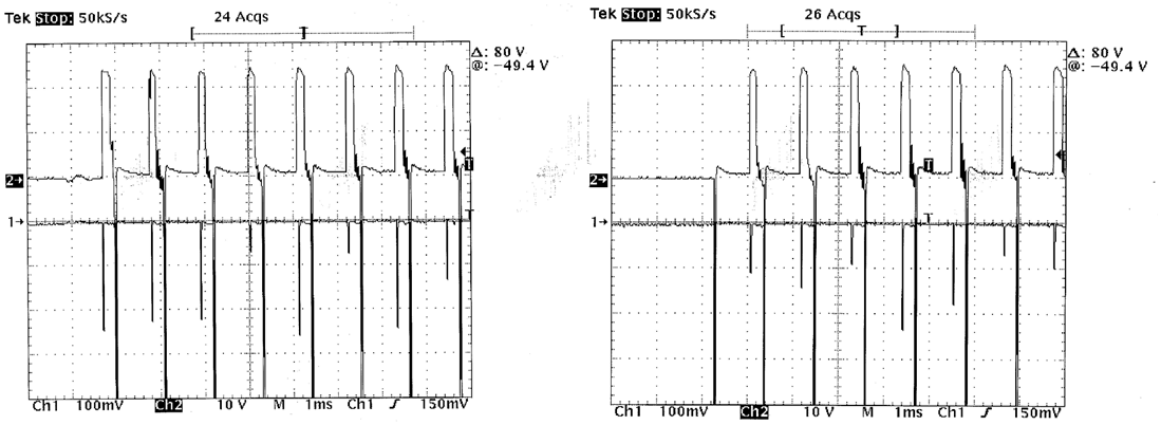

1 - trigger signal to high-speed camera and data aquisition system
2 - ignition system volatage variation due to triggering by the user

Figure C.2 High-speed camera and data acquisition system triggered on ignition signal

Appendix D Phantom v9.0 Camera Spectral Response

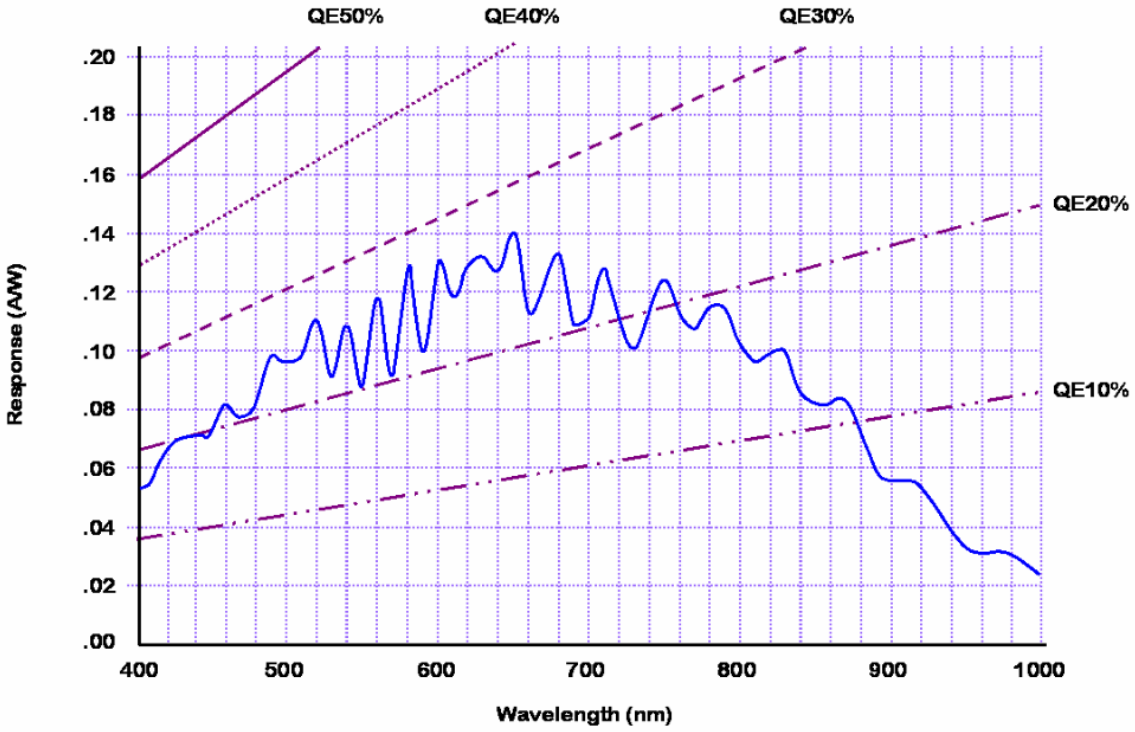

Figure D.1 Phantom v9.0 camera sensor spectral response curve

Appendix E Laser Alignment System

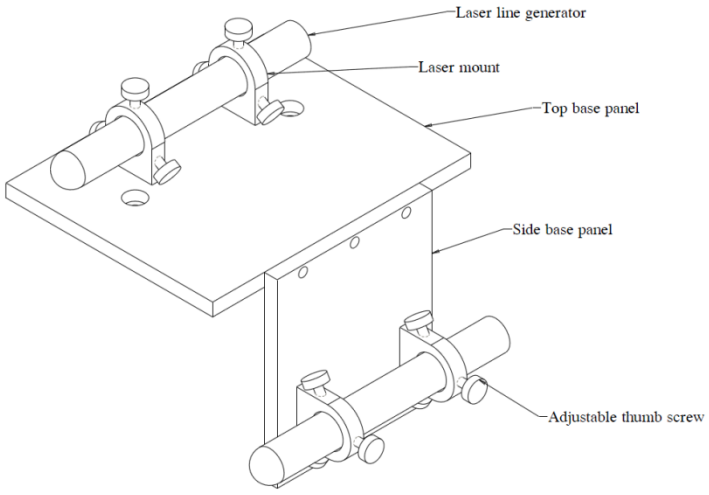

Figure E.1 Laser alignment system

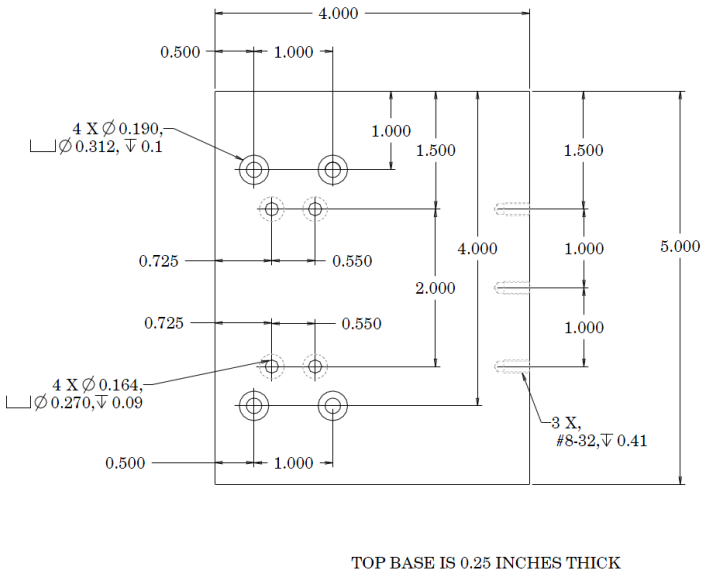

Figure E.2 Top base panel design drawing

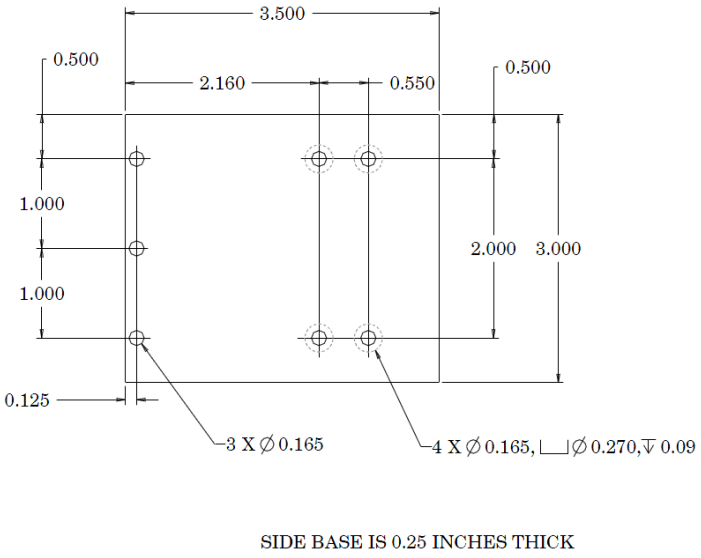

Figure E.3 Side base panel design drawing

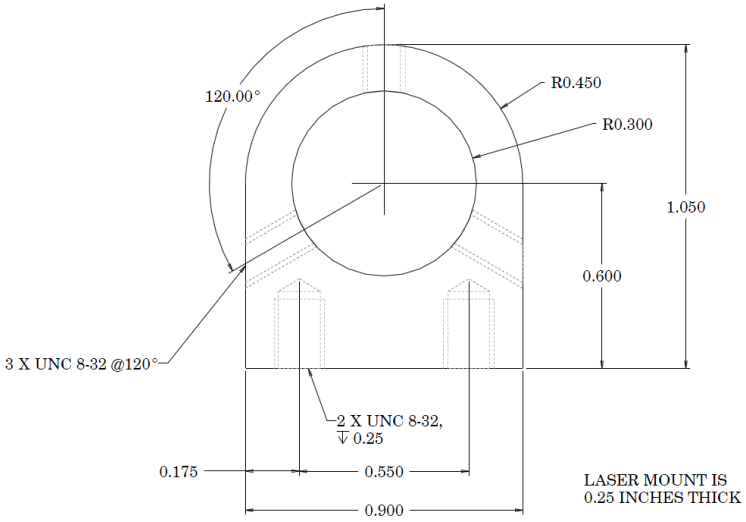

Figure E.4 Laser mount design drawing

Appendix F Sliding Bed for Scoring Aluminum Diaphragms

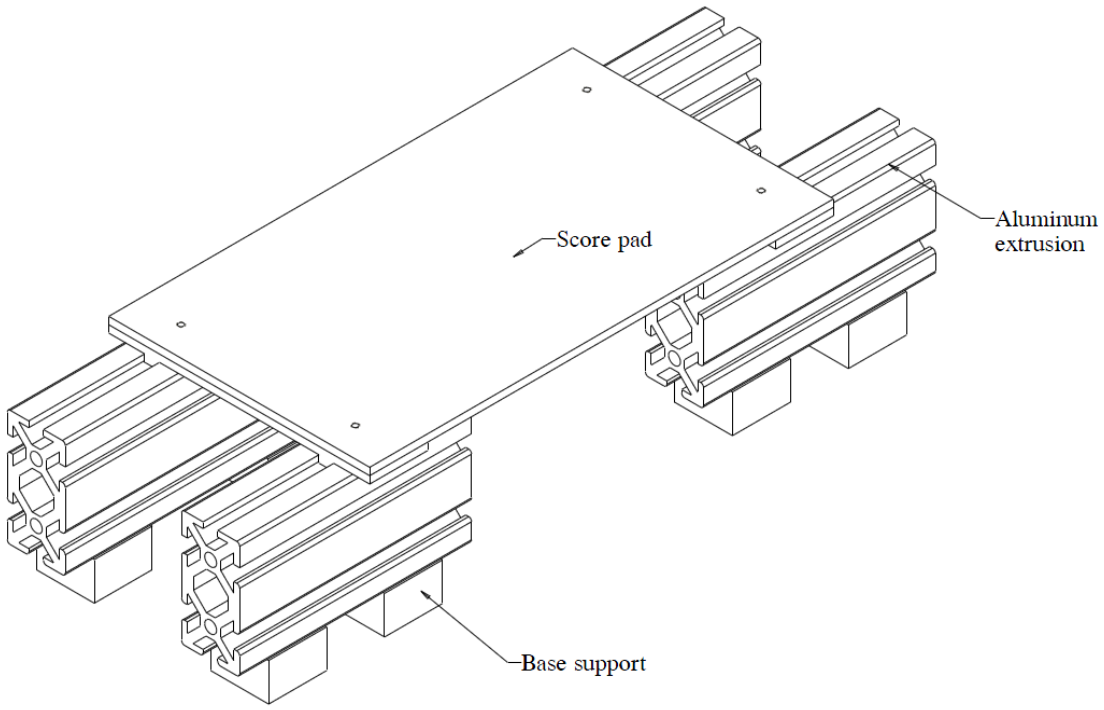

Figure F.1 Sliding bed for scoring aluminum diaphragm

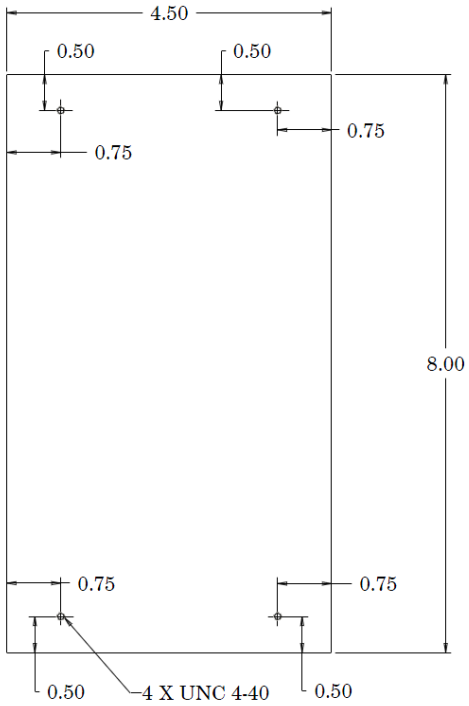

Figure F.2 Score pad design drawing

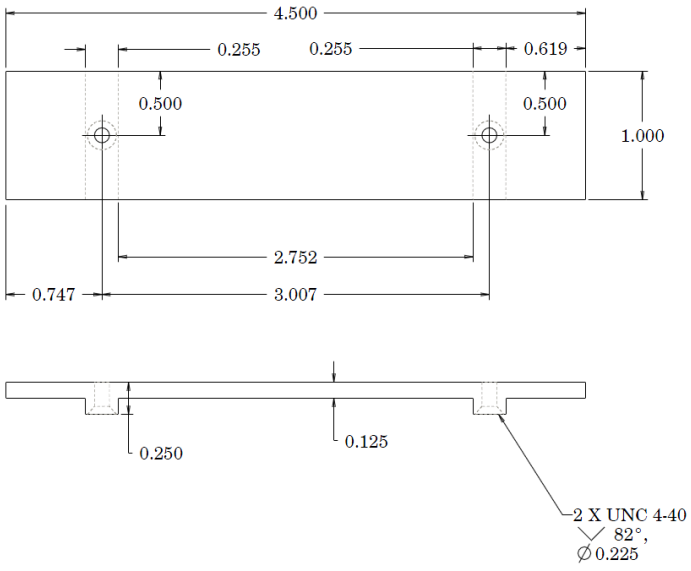

Figure F.3 Sliding bed guide design drawing

Appendix G Infrared Transmitting Filter Specifications

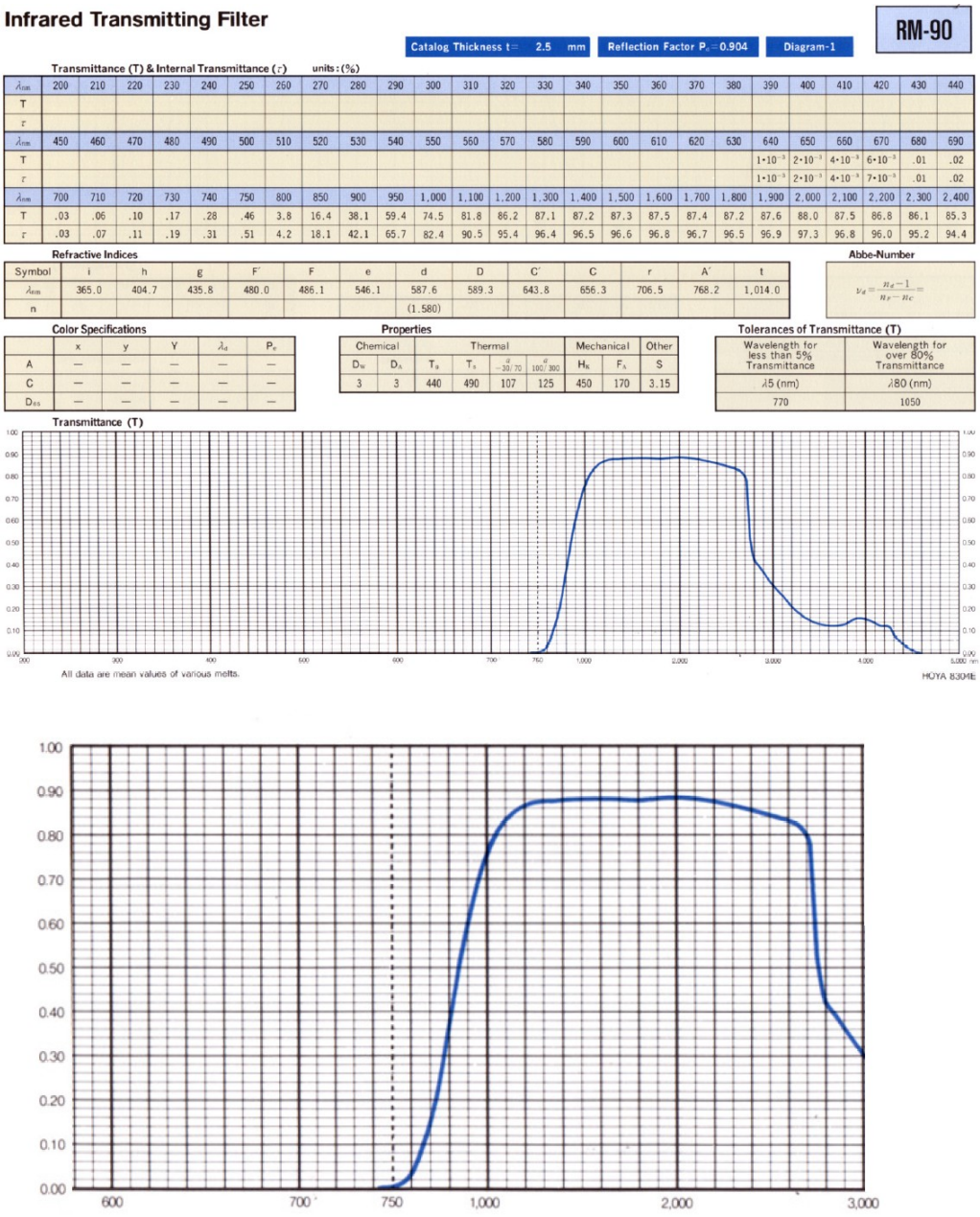

Infrared Transmitting Filter

RM-90

Catalog Thickness t= 2.5 mm | Reflection Factor P_s = 0.904 | Diagram-1

Transmittance (T) & Internal Transmittance (τ) units : (%)

λ_{nm}	200	210	220	230	240	250	260	270	280	290	300	310	320	330	340	350	360	370	380	390	400	410	420	430	440
T																									
τ																									
λ_{nm}	450	460	470	480	490	500	510	520	530	540	550	560	570	580	590	600	610	620	630	640	650	660	670	680	690
T																				$1\cdot10^{-3}$	$2\cdot10^{-3}$	$4\cdot10^{-3}$	$6\cdot10^{-3}$	.01	.02
τ																				$1\cdot10^{-3}$	$2\cdot10^{-3}$	$4\cdot10^{-3}$	$7\cdot10^{-3}$	.01	.02
λ_{nm}	700	710	720	730	740	750	800	850	900	950	1,000	1,100	1,200	1,300	1,400	1,500	1,600	1,700	1,800	1,900	2,000	2,100	2,200	2,300	2,400
T	.03	.06	.10	.17	.28	.46	3.8	16.4	38.1	59.4	74.5	81.8	86.2	87.1	87.2	87.3	87.5	87.4	87.2	87.6	88.0	87.5	86.8	86.1	85.3
τ	.03	.07	.11	.19	.31	.51	4.2	18.1	42.1	65.7	82.4	90.5	95.4	96.4	96.5	96.6	96.8	96.7	96.5	96.9	97.3	96.8	96.0	95.2	94.4

Refractive Indices

Symbol	i	h	g	F'	F	e	d	D	C'	C	r	A'	t
λ_{nm}	365.0	404.7	435.8	480.0	486.1	546.1	587.6	589.3	643.8	656.3	706.5	768.2	1,014.0
n							(1.580)						

Abbe-Number

$$\nu_d = \frac{n_d - 1}{n_F - n_C} =$$

Color Specifications

	x	y	Y	λ_d	P_e
A	—	—	—	—	—
C	—	—	—	—	—
D_{65}	—	—	—	—	—

Properties

Chemical		Thermal				Mechanical		Other
D_w	D_h	T_g	T_s	$\alpha_{-30/70}$	$\alpha_{100/300}$	H_K	F_A	S
3	3	440	490	107	125	450	170	3.15

Tolerances of Transmittance (T)

Wavelength for less than 5% Transmittance	Wavelength for over 80% Transmittance
λ5 (nm)	λ80 (nm)
770	1050

Transmittance (T)

All data are mean values of various melts.

HOYA 830ME

Figure G.1 Infrared transmitting filter RM 90 specifications

Appendix H Pressure Transducer Specifications

ICP® High Frequency-General Purpose
With integral electronics

Optional o-ring isolation mounting adaptor is available for blast applications; see page 59.

Dimensions shown in inches except where noted.

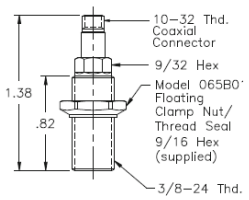

Model 102A12
Ground Isolated

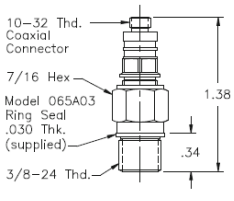

Models 102A, A03, A04, A06, A15
Ground Isolated

Mounting Adaptors on Page 58

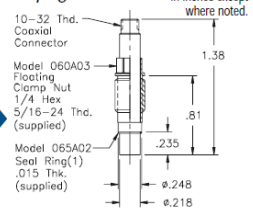

Models 113A21, A22, A23, A24, A26
NEW all Invar Models 113A31, A32, A33, A34, A36

	Dynamic Range (2)	psi	0.05 to 200	0.1 to 500	0.2 to 1000	1 to 5000	2 to 10 000
	MODEL NUMBERS		102A12, A15 113A21 113A31	102A06 113A26 113A36	102A04 113A24 113A34	102A 113A22 113A32	102A03 113A23 113A33
AMPLITUDE	Sensitivity (9)	mV/psi	25	10 ± .5	5 ± .25	1 ± .05	0.5 ± .03
	Resolution	psi	0.003	0.01	0.02	0.1	0.2
	Range (for 5V output)	psi	200	500	1000	5000	10 000
	Range (for 10V output) (3)	psi	400	1000	2000	10 000	20 000
	Maximum Pressure	psi	1000	10 000		15 000	20 000
	Linearity (4)	%FS	≤ 1				
FREQ RESP	Resonant Frequency (5)	kHz	≥ 500				
	Rise Time	µs	≤ 1				
	Discharge Time Constant (6)	sec	≥ 1	≥ 50	≥ 100	≥ 500	≥ 1 000
	Low Frequency (-5%) (6)	Hz	0.5	0.01	0.005	0.001	0.0005
ENVIRONMENTAL	Shock (max)	g pk	20 000				
	Acceleration Sensitivity	psi/g	0.002				
	Temperature Range	°F	-100 to +275				
	Temperature Coefficient	%/°F	≤ 0.03				
	Flash Temperature	°F	3000				
ELECTRICAL	Polarity (positive pressure)		positive				
	Output Impedance	ohm	≤ 100				
	Output Bias	+volts	8 to 14				
	Power Required: Voltage	+VDC	20 to 30				
	Constant Current	mA	2 to 20				
	Ground Isolation	model	102A12, A15	102A06	102A04	102A	102A03
PHYSICAL	Sensing Element	material	quartz				
	Case (7)	material	17-4PH (113A30 series : Invar)				
	Diaphragm (8)	material	Invar				
	Connector (8)	type	10-32 coaxial				
	Sealing (8)	type	epoxy				
OPTIONS	Hermetic Seal (8)	prefix	H				
	Stainless Steel Diaphragm	prefix	S (for series 113A20 only)				
	Emralon Gnd. Isolation Coating	prefix	E (for series 113 only)				
	Negative Polarity	prefix	N				
	Momentum Trap	prefix	T				
	Water-resistant Cable	prefix	W (specify length)				

NOTES:
1. For recess mount, Model 065A05 seal sleeve is available.
2. Measures dynamic pressures from full vacuum to rated maximum.
3. ≥+24 VDC supply required for 10V output. If optional calibration to 10V range is required, linearity specs may change.
4. % FS any calibrated range; zero-based best straight line.
5. Suppressed resonance.
6. Discharge Time Constant (DTC) relates low-frequency to signal lost during transient events at room temperature. See technical section on page 78.
7. Special diaphragm or case material available.
8. Diaphragms of all sensors are welded or integral. Hermetic option specifies a fused-glass electrical connector and welded joints.
9. Unless otherwise designated, sensitivities are ± 15%.

Figure H.1 PCB 113A32 Pressure transducer specifications

Appendix I Main Chamber Redesign Drawings

The design drawings of the redesigned main chamber are provided as supplementary material.